THE UNIVERSITY OF TOKYO

MASTER THESIS

Transport Processes and Quantum Critical Phenomena in Heat Transport via a Two-State System

---

Author:
Tsuyoshi YAMAMOTO

Supervisor:
Takeo KATO

A thesis submitted in fulfillment of the requirements for the degree of Master of Physics

in the

Kato Group
Department of Physics

March, 2019

THE UNIVERSITY OF TOKYO

Abstract

Graduate School of Science
Department of Physics

Master of Physics

Transport Processes and Quantum Critical Phenomena in Heat Transport via a Two-State System

by Tsuyoshi YAMAMOTO

Many-body effects and non-equilibrium properties in heat transport via a nano-scale object have attracted much interest for a few decades. A number of theoretical works have clarified that there appear various kinds of transport processes despite the simpleness of the target system. Recent development in experimental techniques for measurement and sample fabrication has now enabled us to access information of heat current flowing via a nano-scale circuit. In near future, experimental studies on heat transport via a two-state system (a qubit) will be possible.

In this thesis, we systematically investigate heat transport via a two-state system, using the spin-boson system near thermal equilibrium. We derive several analytical formulas for the thermal conductance within the linear response theory. We also perform an accurate numerical simulation with the quantum Monte Carlo method and confirm these predictions for arbitrary types of thermal baths. The present numerical calculation classifies transport mechanism and shows that the noninteracting-blip approximation quantitatively describes thermal conductance in the incoherent transport regime.

In addition, we study quantum critical behavior in heat transport via a two-state system with sub-Ohmic reservoirs theoretically. We calculate temperature dependence of thermal conductance near quantum phase transition and discuss its critical exponents. We also propose superconducting circuits to realize the sub-Ohmic spin-boson model, which can be used for observation of quantum critical phenomena.

Acknowledgements

The work presented in this thesis could not have been done without the support of a lot of people. I am deeply grateful to Professor Takeo Kato. His broad knowledge and great intuition were very helpful for proceeding our research.

I also want to thank the other people in the Kato group. Assistant Professor Rui Sakano taught me how to make the logical presentation. Tomohiro Tamaya gave me various advices as a academic researcher. Masahiro Hasegawa and Marc Ken Ritter are excellence and I have stimulated from them at seminars. Hiroko Eguchi often encouraged me. Without their support, I could have not had my enjoyable graduate life.

Next, I would like to thank Professor Keiji Saito, who came all the way from Keio University in Yokohama. Discussions with him have inspired me. I am also grateful to Masanari Kato. Our work could not proceed smoothly without his work.

Finally, I want to thank my parents. The continued encouragement and financial support of them have helped me.

List of Publications

- T. Yamamoto, M. Kato, T. Kato, and K. Saito, New J. Phys. **20**, 093014 (2018).
- T. Yamamoto and T. Kato, Phys. Rev. B **98**, 245412 (2018).

Contents

Chapter 1

Introduction

In this chapter, we summarize the background of this thesis. After we discuss similarities between heat transport and electronic transport in Section 1.1, we introduce the spin-boson model as a minimal model for describing heat transport via a nano-scale object in Section 1.2. We review existing theoretical and experimental studies on heat transport via a nano-scale object in Section 1.3 and Section 1.4, respectively. We also summarize theoretical studies on quantum phase transition in the sub-Ohmic spin-boson model in Section 1.5. Based on these previous studies, we describe the purpose of this thesis in Section 1.6. Finally, we give the organization of this thesis in Section 1.7.

In this chapter, we give just a brief summary and detailed descriptions of analytical results are given in the subsequent chapters. Throughout this thesis, we employ the unit of $\hbar = 1$.

1.1 Electronic transport vs. Heat transport

In macroscopic scale, it is known that electronic transport is well described by the Ohm's law, which states the charge current is proportional to the negative gradient in the electronic potential, where the linear coefficient is the conductivity. The corresponding macroscopic law in heat transport is the Fourier's law, which states that the time rate of the heat current density $\boldsymbol{j}$ through a material is proportional to the negative gradient in the temperature T:

$$\boldsymbol{j} = -\kappa \nabla T, \tag{1.1}$$

where κ is the thermal conductivity.

For quantum transport via nano-scale objects such as quantum point contact, quantum wires, and quantum dots, electronic transport is described by the Landauer formula [1] based on the scattering theory. This formula predicts quantum transport phenomena, e.g., the quantization of the electronic conductance [2]. It is remarkable that there exists the corresponding formula for heat transport, that is the Landauer-like formula for photons (or phonons) [3]:

$$J = \frac{1}{2\pi} \int_0^\infty d\omega \, \omega \mathcal{T}(\omega) \left[n_L(\omega) - n_R(\omega) \right], \tag{1.2}$$

where $\mathcal{T}(\omega)$ is the transmission probability of photons (or phonons) and $n_\nu(\omega)$ is the Bose-Einstein distribution function in the reservoir ν. Then, the quantized thermal conductance is predicted from Eq. (1.2) as in electronic transport and has indeed been observed in heat transport through one-dimensional wires [4].

TABLE 1.1: Electronic transport vs. heat transport

	Electronic Transport	Heat Transport
Macroscopic law	Ohm's law	Fourier's law (1.1)
Microscopic law	Landauer's formula	Photon (or phonon) version of Landauer formula (1.2)
Nano-scale object	Quantum dot	Two-state system (a qubit)
Quantum phase transition	Multi-channel Kondo model	Sub-Ohmic spin-boson model

As indicated by these two examples, there exist strong similarities between electronic transport and heat transport (see Table 1.1). It is meaningful to consider counterparts of electronic transport phenomena in heat transport. Electronic transport via a quantum dot has been attracting considerable attention because the system exhibits various intriguing phenomena, e.g., the Kondo effect [5]. It is quite natural to ask what happens if one considers heat transport via a zero-dimensional system. Indeed, as a counterpart of electronic transport via quantum dots, we can consider heat transport via a two-state system (or a qubit). This system is described by the spin-boson model (see the next section) and is proved to be related to the Kondo model [6], which exhibits the Kondo effect. Recently, a number of theoretical studies on heat transport via nano-scale objects including two-state systems have shown that various transport phenomena can occur in this system (see Section 1.3). Heat transport via a zero-dimensional system is also important in designing thermal devices such as thermal rectification [7] and thermal transistors [8].

Realizing quantum critical phenomena (QCP) near quantum phase transition in a controlled way is one of the central topics in condensed matter physics. Recently, QCP have been studied for the multi-channel Kondo effect realized in artificial nanostructures [9, 10, 11], and quantum critical behavior has been observed via electronic transport properties in good agreement with theories [12, 13]. It is possible to consider even its counterpart in heat transport. The spin-boson model with sub-Ohmic reservoirs is known to display quantum phase transition at zero temperature when a system-reservoir is tuned at a critical value (for details, see Section 1.5). Heat transport via a two-state system coupled to the sub-Ohmic reservoirs has, however, not been discussed in previous works.

While the similarities between electronic and heat transport via a nano-scale object have been discussed for a few decades, it was generally difficult to study the corresponding heat transport experimentally since high-accuracy calorimetry for nano-scale devices was challenging. Recent development of experimental technology has, however, changed the experimental situation greatly. For example, measurement of heat current via a harmonic oscillator (a circuit resonator) and its control by an external bias voltage have been realized quite recently [14] (for details, see Section 1.4). We expect that experimental studies on heat transport via nano-scale objects will be accelerated in near future.

1.2 Spin-boson model

We consider the spin-boson model as a minimum model describing heat transport via nano-scale objects. Despite simpleness of the model, it exhibits fruitful fundamental physics such as the Kondo effect and quantum phase transition. In this section, we introduce the spin-boson model and discuss its properties briefly.

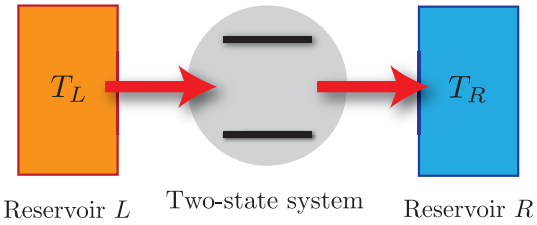

FIGURE 1.1: Schematics of the spin-boson model composed of a two-state system and two thermal reservoirs.

A two-state system coupled to thermal reservoirs is called as the 'spin-boson system' (see Fig. 1.1). The Hamiltonian is composed of three parts

$$H = H_{\rm S} + \sum_{\nu=L,R} H_{{\rm B},\nu} + \sum_{\nu=L,R} H_{{\rm I},\nu}, \tag{1.3}$$

where $H_{\rm S}$, $H_{{\rm B},\nu}$, and $H_{{\rm I},\nu}$ describe a two-state system, a bosonic thermal reservoir ν, and a coupling between the two-state system and the reservoir ν, respectively. Each term of the Hamiltonian is given by as follows:

$$H_{\rm S} = -\frac{\Delta}{2}\sigma_x - \epsilon\sigma_z, \tag{1.4}$$

$$H_{{\rm B},\nu} = \sum_k \omega_{\nu,k} b^\dagger_{\nu,k} b_{\nu,k}, \tag{1.5}$$

$$H_{{\rm I},\nu} = -\frac{\sigma_z}{2}\sum_k \lambda_{\nu,k}\left(b_{\nu,k} + b^\dagger_{\nu,k}\right), \tag{1.6}$$

where σ_α ($\alpha = x,\ y,\ z$) is the Pauli matrix and $b_{\nu,k}$ ($b^\dagger_{\nu,k}$) is the annihilation (creation) operator of bosonic excitation with the wavenumber k in the reservoir ν. The parameters, Δ, ϵ, $\omega_{\nu,k}$, and $\lambda_{\nu,k}$, denote the tunneling amplitude, the detuning energy, the energy dispersion of bosonic excitation, and the system-reservoir coupling strength, respectively. In the spin-boson model, the properties of the reservoirs are characterized by the spectral density:

$$I_\nu(\omega) \equiv \sum_k \lambda^2_{\nu,k}\delta(\omega - \omega_{\nu,k}). \tag{1.7}$$

Assuming that the number of modes is so large to form a continuous spectrum, the spectral density becomes a smooth function of ω, and is usually taken as [15, 6]

$$I_\nu(\omega) = \alpha_\nu \tilde{I}(\omega), \tag{1.8}$$

$$\tilde{I}(\omega) = 2\omega\left(\frac{\omega}{\omega_{\rm c}}\right)^{s-1} e^{-\omega/\omega_{\rm c}}, \tag{1.9}$$

where α_ν is the dimensionless coupling strength between the two-state system and the reservoir ν. We introduced the exponential cutoff function $e^{-\omega/\omega_{\rm c}}$, where the high-frequency cutoff frequency $\omega_{\rm c}$ is assumed to be considerably larger than other characteristic frequencies, e.g., Δ, ϵ, and $k_{\rm B}T$. The exponent s of the spectral density is crucial for determining the properties of the reservoirs. The case $s = 1$ is called 'Ohmic,' whereas the cases $s > 1$ and $s < 1$ are called 'super-Ohmic' and 'sub-Ohmic,' respectively. Note that effect of high-frequency modes ($\omega \gtrsim \omega_{\rm c}$) is renormalized into the tunneling amplitude Δ.

FIGURE 1.2: Schematics of (a) a superconducting transmission-line resonator with a flux qubit and (b) a molecular junction.

The spin-boson model has been used in theoretical studies on decoherence phenomena due to the environments [15, 6]. Recently, this model has been used also for the study of heat transport due to phonons or photons via a nano-scale object. By coupling the two-state system to the two reservoirs with different temperatures ($T_L > T_R$), the heat current flows from one reservoir to the other one (see Fig. 1.1). Since the spin-boson model is a simple model for describing heat transport, it has been used for a variety of systems, e.g., superconducting circuits [16, 17, 18], photonic waveguides with local two-state systems [19], and molecular junctions [20, 21] (see Fig. 1.2).

In the following sections, we briefly review existing theoretical and experimental studies on heat transport via a two-state system using the spin-boson system. The explicit expression of the heat current in this model will be given in Chapter 2.

1.3 Theories on heat transport via a nano-scale object

1.3.1 Analytical formulas

In a number of theoretical studies, heat transport via a two-state system has been investigated by analytical methods [7, 22, 23, 24, 25, 26, 27]. In the pioneering work by Ruokola and Ojanen [23], heat current via a two-state system was calculated using perturbation calculation with respect to the coupling Hamiltonian $H_{\rm I}$. This calculation gives transition rates between the eigenstates of the two-state Hamiltonian, $|\pm\rangle$. Solving the stochastic equation, we obtain the heat current as

$$J = J_+ + J_-, \tag{1.10}$$

$$J_\pm = \frac{\pi \sin^4\theta}{8} \int_0^\infty d\omega\, \omega I_L(\omega) I_R(\omega) \left[n_L(\omega) - n_R(\omega)\right] \times \left| \frac{1}{\omega - \omega_0 \pm \frac{i}{2}\Gamma_+} - \frac{1}{\omega + \omega_0 \mp \frac{i}{2}\Gamma_+} \right|, \tag{1.11}$$

where $\tan\theta = \Delta/\epsilon$, $\omega_0 = \sqrt{\epsilon^2 + \Delta^2}$, $n_\nu(\omega)$ is the Bose-Einstein distribution function in reservoir ν, and $\Gamma_\pm$ is a transition rate out of state $|\pm\rangle$ calculated by the Fermi's golden rule.

At the high-temperatures limit ($k_{\rm B}T \sim \Delta$), since resonant energy transfer at $\omega = \omega_0$ is dominant, the heat current is obtained as

$$J = \frac{\pi}{2} \frac{\sin^2\theta\, \omega_0 I_L(\omega_0) I_R(\omega_0) \left[n_L(\omega_0) - n_R(\omega_0)\right]}{I_L(\omega_0)\left[2n_L(\omega_0)+1\right] + I_L(\omega_0)\left[2n_L(\omega_0)+1\right]}. \tag{1.12}$$

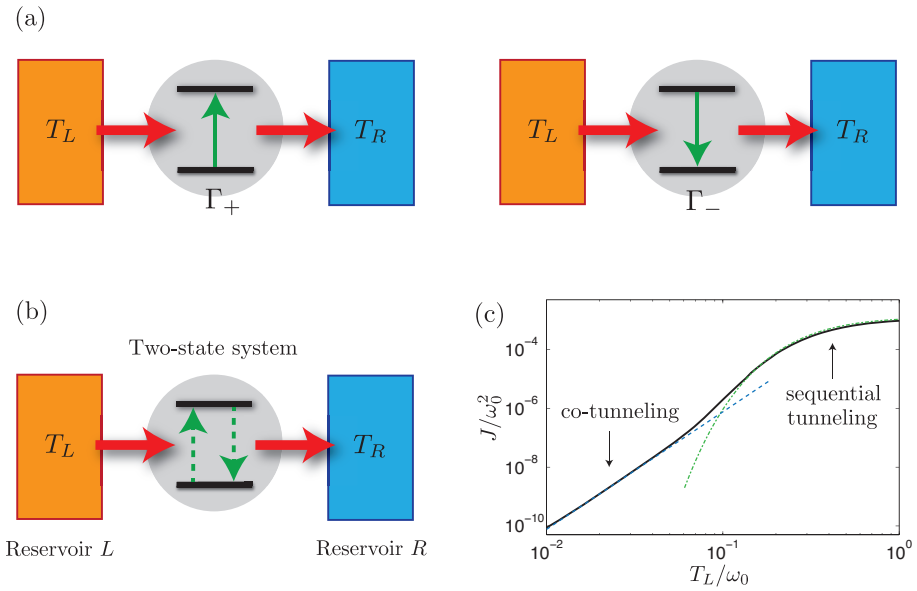

FIGURE 1.3: Schematics of (a) the sequential tunneling and (b) co-tunneling processes. (c) The left-reservoir temperature dependence of the total heat current for the symmetric Ohmic case ($s = 1$, $\epsilon = 0$) with $\alpha_L = \alpha_R = 0.1/\pi$ [23]. Right-reservoir temperature is $T_R = 0.95T_L$. The solid line represents the numerical solution of Eq. (1.11), the green dash-dotted line represents the high-temperature approximation (1.12), and the blue dashed line represents the low-temperature approximation (1.13).

This formula indicates a heat transport process induced by boson absorption and emission (see Fig. 1.3 (a)). This transport process is called the 'sequential tunneling'. In contrast, at the low-temperature limit ($k_B T \ll \Delta$), the frequency dependence of the energy denominators in Eq. (1.11) can be ignored and the excitation of the two-state system is exponentially suppressed. Then, the expression of the heat current has been obtained as

$$J = \frac{\pi \sin^4\theta}{2\omega_0^2} \int_0^\infty d\omega\, \omega I_L(\omega) I_R(\omega) \left[n_L(\omega) - n_R(\omega)\right]. \tag{1.13}$$

This expression indicates heat transport via a virtual excitation in the two-state system (see Fig. 1.3 (b)). This transport process is called the 'co-tunneling'.

Roukola and Ojanen have also shown that the crossover between the sequential tunneling and co-tunneling is quite sharp as shown in Fig. 1.3 (c). This means that one of the two analytical formulas holds well except for a narrow transition region. We should note that the heat current (1.13) in the co-tunneling regime obtained by the perturbative method does not include higher-order processes, which is important in the Kondo effect.

There are many other theoretical approaches to treat heat transport via a two-state system. For weak system-reservoir coupling, one can consider perturbative calculation for general quantum systems using the quantum master equation [7] and the nonequilibrium Green's function method [25]. For strong system-reservoir coupling, the noninteracting-blip approximation (NIBA) [22, 24] and the polaron-transformed Redfield equation (PTRE) [26, 27] have been applied. Although these analytical methods are powerful in analyzing heat transport, the condition for which

these approximations hold well is non-trivial.

1.3.2 Kondo effect

In the spin-boson model, the many-body effect emerges due to the strong interaction between the local system and the environments. In particular, it is known that the symmetric Ohmic spin-boson model ($s = 1$, $\epsilon = 0$) can be related to the anisotropic Kondo model [5] using the bosonization technique [6, 15, 28]. The Kondo model describes a single magnetic impurity with spin $1/2$ interacting with conduction electrons. The ground state forms a singlet state between the spin of the impurity and spins of conduction electrons, which is called the 'Kondo singlet'. The temperature at which the Kondo singlet is formed is characterized by the Kondo temperature $T_{\rm K}$.

The anisotropic Kondo Hamiltonian takes the form

$$H_{\rm K} = \sum_{k,s} \epsilon_k c^\dagger_{k,s} c_{k,s} + \frac{J_\parallel}{4L}\sigma_z \sum_{k,k',s} s c^\dagger_{k,s} c_{k',s} + \frac{J_\perp}{2L}\sum_{k,k'}\left(\sigma_+ c^\dagger_{k,\downarrow} c_{k',\uparrow} + \sigma_- c^\dagger_{k,\uparrow} c_{k',\downarrow}\right), \quad (1.14)$$

where $c_{k,s}$ ($c^\dagger_{k,s}$) is the annihilation (a creation) operator of the conduction electron with wavenumber k and spin polarization s $=\uparrow$ or $\downarrow$, L is the system size, and $\sigma_\pm = (\sigma_x \pm i\sigma_y)/2$. The $J_\parallel$-term describes the scattering of the impurity in which the spin polarization is conserved while the $J_\perp$-term describes spin-flip scattering. The correspondence of the parameters between the Ohmic spin-boson model and the anisotropic Kondo model is [6, 15, 28]

$$\Delta/\omega_{\rm c} = \rho J_\perp \cos^2\left[\arctan\left(\frac{\pi\rho J_\parallel}{4}\right)\right], \quad (1.15)$$

$$\alpha = \left[1 - \frac{2}{\pi}\arctan\left(\frac{\pi\rho J_\parallel}{4}\right)\right]^2, \quad (1.16)$$

where ρ is the density of states of conduction electrons. In the Ohmic spin-boson model, the characteristic energy scale (the Kondo temperature) is given by [6, 15, 29]

$$k_{\rm B}T_{\rm K} = \begin{cases} \Delta\left(\dfrac{\Delta}{\omega_{\rm c}}\right)^{\alpha/(1-\alpha)}, & (0 < \alpha < 1), \\ 0, & (1 \le \alpha). \end{cases} \quad (1.17)$$

We show the "Kondo temperature" as a function of the system-reservoir coupling α in Fig. 1.4. As shown Fig. 1.4, at low temperature $T < T_{\rm K}$, the Kondo-like many-body state is realized in the spin-boson model.

Saito and Kato have studied the Kondo-like effect in heat transport in the Ohmic spin-boson model using the quantum Monte Carlo simulation [29]. They have clarified the Kondo signature in the universal temperature dependence of the linear thermal conductance proportional to T^3 at low temperatures ($T \ll T_{\rm K}$) (see Fig. 1.5). They have also shown that at high temperatures the thermal conductance is proportional to $T^{2\alpha-1}$. While the detailed features of the thermal conductance have been clarified for the Ohmic spin-boson model, the non-Ohmic case (the sub-Ohmic and super-Ohmic cases) has not been studied so much. It is a fundamental question whether the Kondo-like effect emerges in heat transport in the non-Ohmic spin-boson model or not.

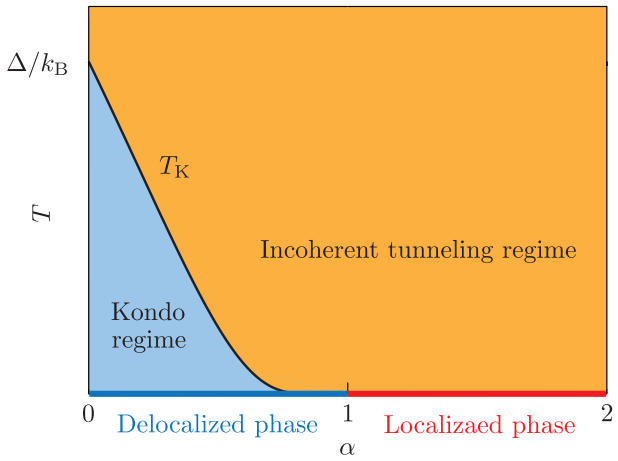

FIGURE 1.4: The "Kondo temperature" T_{K} as a function of α. This line indicates a crossover from the Kondo regime (blue) to the incoherent tunneling regime (orange). At zero temperature, a quantum phase transition occurs at $\alpha = 1$.

FIGURE 1.5: The temperature dependence of the thermal conductance for various α [29]. The thermal conductance is proportional to $T^{2\alpha-1}$ for high temperatures and T^3 for low temperatures.

1.4 Experiments on heat transport via a nano-scale object

The recent, rapid development in techniques of heat measurement that has enabled us to experimentally access the heat current in nano-scale objects is remarkable. In particular, Ronzani *et al.* have observed heat transport via resonator-system-resonator quite recently (see Fig. 1.6 (a)) [14]. They have considered two models: the quasi-Hamiltonian (QH) model for $\gamma \simeq g$ and the non-Hamiltonian (NH) model for $\gamma \ll g$, where γ and g are the reservoir-resonator and resonator-system couplings, respectively. For each model, they have measured the total heating powers for the different source temperatures with high accuracy as shown in Fig. 1.6 (b) and (c).

In addition, it has been theoretically proposed that a superconducting qubit coupled to transmission lines realizes the Ohmic spin-boson model [17, 18], and experimentally demonstrated [31, 30]. The experimental setup composed of a superconducting flux qubit (a two-state system) coupled to transmission lines (reservoirs) is shown in Fig. 1.7 (a). The flux qubit consists of a superconducting loop interrupted by three (or more) Josephson junctions [32] (for details, see Section 6.1). Magazzú *et*

FIGURE 1.6: (a) A circuit representing the experimental setup in Ref. [14]. A transmon qubit, whose tunneling amplitude can be tunable by the external flux Φ, is coupled to two $L_{\mathrm{r}}C_{\mathrm{r}}$-resonators and each resonator is terminated at one end by a mesoscopic normal-metal resistor which plays the role as the reservoir. The total heating powers as a function of the external flux Φ in (b) the QH model and (c) the NH model regimes for different source temperatures T_{S} [14].

FIGURE 1.7: (a) Experimental setup in Ref. [30]. A coplanar waveguide running across the chip plays the role as the Ohmic reservoir. The inset is a scanning electron micrograph showing the flux qubit and the scale bar is 2 μm. (b)-(d) Experimental and theoretical transmissions for $\alpha = 0.007,\ 0.21$, and 0.8, respectively [30].

al. have experimentally investigated an impact of quantum coherence by the system-reservoir coupling strength [30]. When the microwave is injected into the transmission line, the detuning energy is described by

$$\varepsilon(t) = \varepsilon_0 + \varepsilon_p \cos(\omega_p t), \tag{1.18}$$

where ε_p and ω_p are the amplitude and frequency of microwave, respectively, and the static detuning energy ε_0 is given as $\varepsilon_0 \propto \Phi_\varepsilon - \Phi_0/2$ (Φ_ε: the external flux, $\Phi_0 = h/2e$: flux quantum). When the microwave amplitude is weak, the linear response theory gives the transmission at the microwave frequency ω_p as

$$\mathcal{T}(\omega_p) = 1 - i\mathcal{N}\omega_p\chi(\omega_p), \tag{1.19}$$

where $\mathcal{N}$ is a coupling constant determined by fitting and $\chi(\omega)$ is the dynamic susceptibility of the qubit. Fig. 1.7 (b)-(d) show the experimental (the left side) and theoretical (the right side) transmissions as a function of the static detuning energy ε_0 and the probe frequency ω_p for different coupling strengths. The theoretical results have been calculated in the NIBA [15, 6]. For the weakest coupling strength, $\alpha = 0.007$, one can see the high quantum coherence as shown in Fig. 1.7 (b). As the coupling strength is increased, for $\alpha = 0.21$, the quantum coherence is reduced, but the hyperbolic curve characteristic of it can be recognized in Fig. 1.7 (c). However, for the strongest coupling strength, $\alpha = 0.8$, the quantum coherence is broken completely and the transmission is independent of the prove frequency as shown in Fig. 1.7 (d).

We expect that heat transport via a two-state system will be measured in near future by combining the accurate heat measurement technique [14] with the controlled system-reservoir coupling [30].

1.5 Quantum critical phenomena

One of the intriguing phenomena in the spin-boson model is that, at zero temperature, a quantum phase transition occurs when the coupling strength between the two-state system and thermal reservoirs is tuned to a critical point α_c. For $\alpha < \alpha_c$, the ground state is described by a coherent superposition of two wavefunctions localized at each well, and is called a 'delocalized phase'. For $\alpha > \alpha_c$, the ground-state becomes two-fold degenerate because the coherent superposition is completely broken due to the disappearance of quantum tunneling between the two wells. This phase is called a 'localized phase'. For the Ohmic case, a Kosterlitz-Thouless-type phase transition occurs at $\alpha_c = 1$ [6, 33, 34]. The sub-Ohmic case shows a second-order phase transition [35, 36, 37, 38, 39, 40]. The super-Ohmic case does not have a distinct phase transition.

In this thesis, we focus on quantum critical phenomena in the sub-Ohmic case. Fig. 1.8 shows schematic of the population $\langle\sigma_z\rangle_\varepsilon$ as a function of the detuning energy ϵ near the critical point $\alpha = \alpha_c$. In the delocalized phase ($\alpha < \alpha_c$), the slope at $\epsilon = 0$

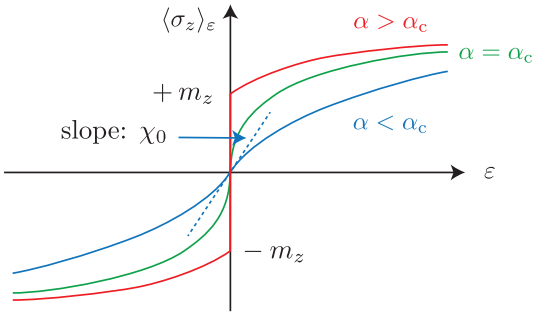

FIGURE 1.8: Population, $\langle\sigma_z\rangle_\varepsilon$, as a function of the detuning energy, ϵ near the critical point. For $\alpha < \alpha_c$ (blue line), $\langle\sigma_z\rangle_\varepsilon$ is a continuous function of ϵ, and the static susceptibility, χ_0, can be defined by the slope at $\epsilon = 0$. At the critical point (green line; $\alpha = \alpha_c$), $\langle\sigma_z\rangle_\varepsilon$ is continuous, but the static susceptibility diverges at $\epsilon = 0$. For $\alpha > \alpha_c$ (red line), $\langle\sigma_z\rangle_\varepsilon$ is discontinuous at $\epsilon = 0$.

TABLE 1.2: Summary of the critical exponents.

Exponent	Definition	Condition
γ	$\chi_0 \propto (\alpha_c - \alpha)^{-\gamma}$	$\alpha < \alpha_c$, $T = 0$
β'	$m_z \propto (\alpha - \alpha_c)^{\beta'}$	$\alpha > \alpha_c$, $T = 0$
η	$C(\tau) \propto \tau^{-\eta}$	$\alpha = \alpha_c$, $\lvert\tau\rvert \ll 1/k_B T$
x	$\chi_0 \propto T^{-x}$	$\alpha = \alpha_c$, $T > 0$

corresponds to the static susceptibility defined as

$$\chi_0 = \lim_{\epsilon \to 0} \frac{\langle\sigma_z\rangle_\varepsilon}{\epsilon}, \tag{1.20}$$

where $\langle\cdots\rangle$ implies an equilibrium average. The static susceptibility diverges as the system-reservoir coupling α approaches the critical point α_c from below. In the localized phase ($\alpha > \alpha_c$), the population $\langle\sigma_z\rangle_\varepsilon$ jumps from $-m_z$ to $+m_z$ at $\epsilon = 0$, where $m_z \equiv \langle\sigma_z\rangle_{\epsilon\to+0}$ is the spontaneous magnetization. Information of the system dynamics in thermal equilibrium is included in the imaginary-time correlation function $C(\tau) = \langle\sigma_z(\tau)\sigma_z(0)\rangle$. In Table 1.2, we summarize the critical exponents. In principle, all the exponents can be determined experimentally by measurement of the population $\langle\sigma_z\rangle_\varepsilon$. By using the two exponents related to the fixed point, y_t^* and y_h^*, the critical exponents in Table 1.2 are expressed as [37]

$$\gamma = \frac{2y_h^* - 1}{y_t^*}, \quad \beta' = \frac{1 - y_h^*}{y_t^*}, \quad \eta = 1 - x = 2 - 2y_h^*. \tag{1.21}$$

For the case of $0 < s \leq 0.5$, the exponents, y_t^* and y_h^*, are given by the mean-field theory as [41, 42, 37]

$$y_t^* = \frac{1}{2}, \quad y_h^* = \frac{3}{4}, \tag{1.22}$$

because the transition occurs above the upper critical dimension. Hence, we obtain

$$\gamma = 1, \quad \beta' = \frac{1}{2}, \quad \eta = \frac{1}{2}, \quad x = \frac{1}{2}. \tag{1.23}$$

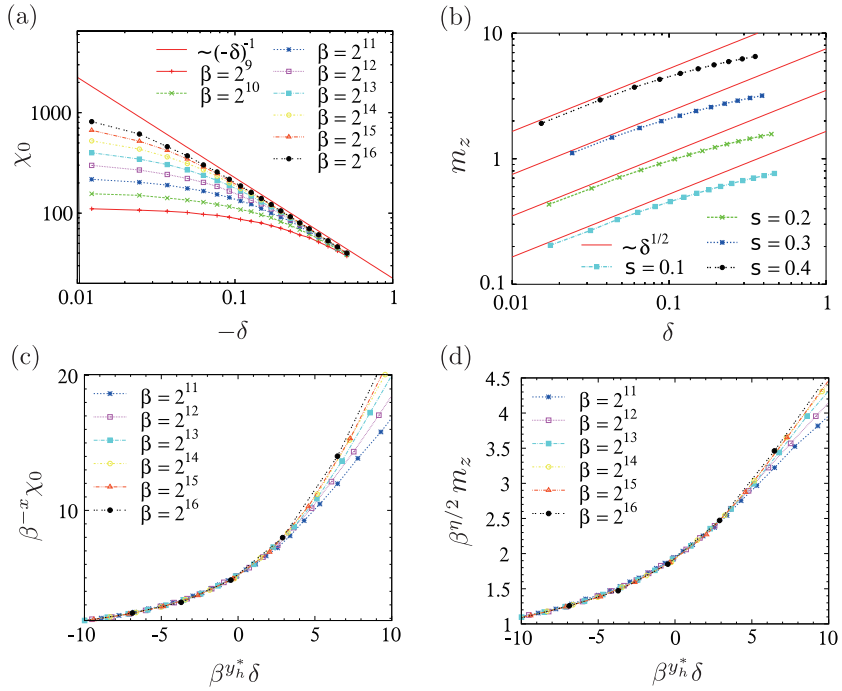

FIGURE 1.9: The static susceptibility χ_0 and magnetization m_z close to the critical point for $s = 0.2$ and $\Delta/\omega_c = 0.1$ [37]. (a) χ_0 as a function of the distance from the critical point $-\delta \equiv -(\alpha - \alpha_c)/\alpha_c > 0$ for different temperatures. As the temperature is lowered, the static susceptibility approaches a line proportional to $(-\delta)^{-1}$. (b) m_z as a function of $\delta > 0$ for different s. The straight lines are proportional to $\delta^{1/2}$. (c)-(d) $T^{1/2}\chi$ and $T^{-1/4}m_z$ collapse onto one point at $\delta = 0$.

Winter *et al*. have demonstrated using the quantum Monte Carlo simulation and confirmed that these critical exponents for $0 < s \leq 0.5$ agree with the numerical results in Fig. 1.9 [37]. For $0.5 < s < 1$, the exponents, y_t^* and y_h^*, are nontrivial functions of the exponent s of the spectral density. Luijten has calculated the exponents using the ε-expansion as follows [41]:

$$y_t^* = s + \frac{1}{6}\varepsilon - \frac{4A(s)}{9s}\varepsilon^2 + \mathcal{O}(\varepsilon^3), \quad y_h^* = \frac{1+s}{2} + \frac{1}{4}\varepsilon - \frac{A(s)}{6s}\varepsilon^2 + \mathcal{O}(\varepsilon^3), \tag{1.24}$$

where $\varepsilon = 2s - 1$, $A(s) = s\,[\psi(1) - 2\psi(s/2) + \psi(s)]$, and $\psi(x)$ is the digamma function. Vojta *et al*. have studied quantum critical phenomena using the numerical renormalization group (NRG) for all values of s [35, 36, 38, 40]. The NRG produces the phase diagram consistent with one from the quantum Monte Carlo methods [35, 37]. However, the NRG simulation gives incorrect critical exponents which do not agree with those from the quantum Monte Carlo method [37] or Eq. (1.22) for the case of $0 < s \leq 0.5$. In Ref. [40], the origin of this disagreement has been discussed and attributed to a failure in describing quantum critical phenomena in a naive NRG simulation. Finally, we show a schematic phase diagram of the sub-Ohmic spin-boson model in Fig. 1.10.

So far, experimental realization of the sub-Ohmic spin-boson model has been discussed only in few theoretical works. In Refs. [43, 44], experimental realization of the sub-Ohmic reservoirs of $s = 0.5$ was theoretically proposed using transmission lines with resistance elements. The sub-Ohmic reservoirs with arbitrary s have, however,

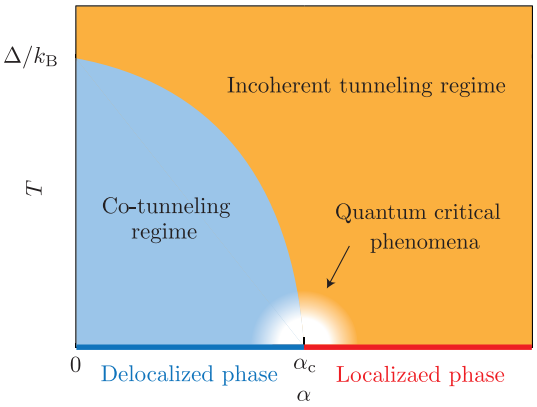

FIGURE 1.10: The phase diagram of the sub-Ohmic case. At zero temperature, a quantum phase transition occurs between the delocalized and localized phases at the critical point $\alpha = \alpha_{\mathrm{c}}$. In contrast, at finite temperature, there is a crossover between the co-tunneling and incoherent tunneling regimes.

not been discussed.

1.6 Purpose

In this thesis, we study heat transport using the spin-boson model, which is the simplest model to describe heat transport via a nano-scale object. Despite its simpleness, the spin-boson model exhibits remarkable many-body phenomena such as the Kondo effect and the quantum phase transition. Theoretical analysis of the spin-boson model not only contributes to the understanding of transport processes and many-body effect in heat transport but also provides a concrete foundation for designing novel thermal devices.

In this thesis, we focus on heat transport near equilibrium, for which the linear response theory is applicable. We calculate the thermal conductance, which is the linear-response coefficient in heat current under a temperature gradient, using both analytical and numerical methods. We first derive analytical formulas for three different transport processes, i.e., sequential tunneling, co-tunneling, and incoherent tunneling. In a previous study [45], Kato has derived a new asymptotically exact expression including higher-order perturbations, which are not taken into account in the previous work by Ruokola and Ojanen [23]. This new formula is applicable also to the non-Ohmic spin-boson model and is useful to understand the Kondo-like effect at low-temperatures. We perform the continuous-time quantum Monte Carlo simulation and compare the numerical results with these analytical formulas. The present Monte Carlo study is a substantial extension of the previous work by Saito and Kato [29] toward arbitrary types of reservoirs; in Ref. [29], only the Ohmic reservoirs have been considered. We confirm the temperature dependencies predicted by our expressions for the co-tunneling and the sequential-tunneling transport regime, and in addition, discuss the accuracy of noninteracting-blip approximation (NIBA) [15] in incoherent tunneling regime. We consider a general picture to understand transport properties at extremely low temperatures for the whole regime of spectral densities and also characterize the transport mechanism for all temperature regimes quantitatively.

In this thesis, we also investigate quantum critical phenomena in heat transport via a two-state coupled to the sub-Ohmic reservoirs. We calculate the temperature dependence of thermal conductance in the critical regime and discuss how its critical exponent is determined. We also propose superconducting circuits to realize the sub-Ohmic spin-boson model with an arbitrary value of s. The present study will provide a useful starting point for observing quantum critical phenomena via heat transport.

1.7 Outline

This thesis is organized as follows. In Chapter 2, we explain the spin-boson model in detail and derive the linear thermal conductance using the Keldysh formalism. In Chapter 3, after introducing an effective tunneling amplitude, we classify the transport mechanism and derive analytical expressions for the thermal conductance in each process. We also consider quantum critical phenomena in the sub-Ohmic case. In Chapter 4, we explain the numerical method to calculate the thermal conductance based on the continuous-time quantum Monte Carlo method. In Chapter 5, we show numerical results of the thermal conductance and compare the results with analytical approximations derived in Chapter 3. We also determine the critical exponent of the thermal conductance in the sub-Ohmic case. In Chapter 6, we propose superconducting circuits with a qubit to realize the sub-Ohmic reservoirs. Finally, we summarize our study in Chapter 7.

Chapter 2

Formulation

In this chapter, we first introduce a general Hamiltonian coupled to reservoirs and consider the reduction of it to the spin-boson Hamiltonian. Second, we derive the Meir-Wingreen-Landauer-type formula for the thermal conductance using the standard Keldysh formalism.

2.1 Model

We consider heat transport via a local quantum system coupled to two reservoirs denoted by L and R. The model Hamiltonian is given by

$$H = H_{\rm S} + \sum_{\nu={\rm L,R}} H_{{\rm B},\nu} + \sum_{\nu={\rm L,R}} H_{{\rm I},\nu}, \tag{2.1}$$

$$H_{\rm S} = \frac{p^2}{2M} + V(q), \tag{2.2}$$

$$H_{{\rm B},\nu} = \sum_k \left(\frac{p_{\nu,k}}{2m_{\nu,k}} + \frac{1}{2} m_{\nu,k} \omega_{\nu,k}^2 x_{\nu,k}^2 \right), \tag{2.3}$$

$$H_{{\rm I},\nu} = \sum_k \left(-C_{\nu,k} x_{\nu,k} q + \frac{C_{\nu,k}^2}{2m_{\nu,k}\omega_{k,\nu}^2} q^2 \right), \tag{2.4}$$

where $H_{\rm S}$, $H_{{\rm B},\nu}$, and $H_{{\rm I},\nu}$ describe the local system, the reservoir ν (=L, R), and the interaction between them, respectively. The operators p and q are the momentum and position of the local system, respectively, and $V(q)$ is the potential energy. The reservoirs comprise multiple phonon (or photon) modes, which are described in general by harmonic oscillators with frequency $\omega_{\nu,k}$ and mass $m_{\nu,k}$, where the subscript denotes the phonon (photon) wavenumber k in the reservoir ν. The momentum and position of an individual oscillator are denoted by $p_{\nu,k}$ and $x_{\nu,k}$, respectively. For simplicity, the system-reservoir coupling $H_{{\rm I},\nu}$ is consider as a bilinear form of q and $x_{\nu,k}$, and the interaction strength is denoted by $C_{\nu,k}$. The second term of $H_{{\rm I},\nu}$ is a counter term to cancel the potential renormalization due to the reservoirs [46, 15].

In this thesis, the potential energy $V(q)$ of the local system is considered as a double-well potential as shown in Fig. 2.1:

$$V(q) = \frac{M\omega_0^2}{2} \left(\frac{q^2 - \frac{1}{4}q_0^2}{q_0} \right)^2, \tag{2.5}$$

where ω_0 is the frequency of small oscillation in each well. The double-well potential, $V(q)$, has minimal potential energy $V(\pm q_0/2) = 0$ at $q = \pm q_0/2$ and the barrier height $V_b \equiv V(q=0) = M\omega_0^2 q_0^2/32$. Quantum tunneling between the two

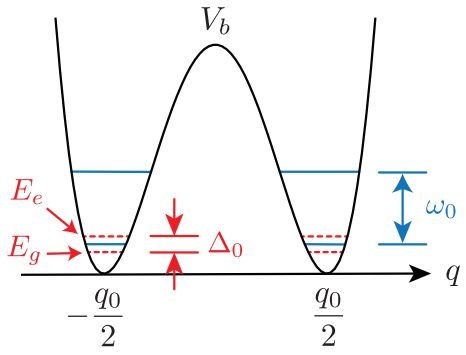

FIGURE 2.1: Symmetric double-well potential of the local system. An energy spacing of quantum levels in each well is ω_0 (indicated by the blue solid lines), and an energy splitting due to quantum tunneling (indicated by the red dashed lines) is $\Delta = E_e - E_g$, where E_g and E_e are the ground-state energy and the first-excited-state energy, respectively.

wells induces small energy splitting Δ_0 between the ground-state energy E_g and the first-excited-state energy E_e.

We consider the parameter regime

$$\Delta_0,\ |\epsilon|,\ k_{\rm B}T \ll \omega_0 \ll V_b, \tag{2.6}$$

where ω_0 is the energy spacing of quantum levels in each well, ϵ is a detuning energy. The tunneling amplitude Δ_0 can be calculated using instanton methods as follows (see Appendix A) [15, 47]:

$$\Delta_0 = 8\sqrt{\frac{2V_b}{\pi\omega_0}}\omega_0 \exp\left(-\frac{16V_b}{3\omega_0}\right), \tag{2.7}$$

the local system with the double-well potential is effectively restricted to a two-dimensional Hilbert space spanned by the states $|\uparrow\rangle$ and $|\downarrow\rangle$ localized in the right and left wells, respectively, and described by the two-state Hamiltonian in terms of the Pauli matrices $\{\sigma_i\}$ in the pseudo-spin form (see Fig. 2.2):

$$H_{\rm S} = -\frac{\Delta}{2}\sigma_x - \epsilon\sigma_z. \tag{2.8}$$

Here, for later convenience, we employ the renormalized tunneling amplitude Δ, which includes the effect of the high-frequency oscillators using adiabatic renormalization (for the detail discussion, see Section 3.1), instead of the bare tunneling amplitude Δ_0. In this thesis, we examine the symmetric double-well potential ($\epsilon = 0$). For the symmetric case ($\epsilon = 0$), the system Hamiltonian $H_{\rm S}$ describes the tunneling splitting Δ between the ground state ($\sigma_x = +1$) and the first excited state ($\sigma_x = -1$). Introducing annihilation and creation operators of the harmonic oscillators with the wavenumber k in the reservoir ν:

$$b_{\nu,k} = \sqrt{\frac{m_{\nu,k}\omega_{\nu,k}}{2}}\left(x_{\nu,k} + i\frac{p_{\nu,k}}{m_{\nu,k}\omega_{\nu,k}}\right), \tag{2.9}$$

$$b^\dagger_{\nu,k} = \sqrt{\frac{m_{\nu,k}\omega_{\nu,k}}{2}}\left(x_{\nu,k} - i\frac{p_{\nu,k}}{m_{\nu,k}\omega_{\nu,k}}\right), \tag{2.10}$$

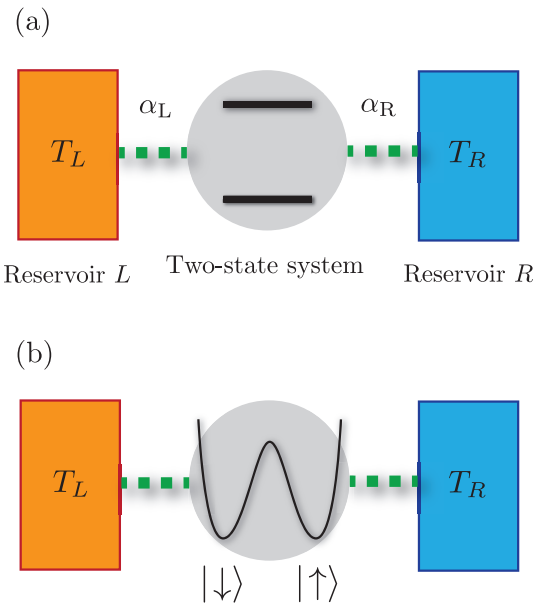

FIGURE 2.2: Schematic of the model comprises a two-state system coupled to two bosonic reservoirs (L and R) with temperatures $T_{\rm L}$ and $T_{\rm L}$, respectively. Symmetric double-well potential of the local system. (a) σ_x-basis and (b) σ_z-basis for the local two-state system.

the Hamiltonians of the reservoir and the system-reservoir interaction can be expressed in terms of these operators:

$$H_{{\rm B},\nu} = \sum_k \omega_{\nu,k} b^\dagger_{\nu,k} b_{\nu,k}, \tag{2.11}$$

$$H_{{\rm I},\nu} = -\frac{\sigma_z}{2} \sum_k \lambda_{\nu,k} \left(b_{\nu,k} + b^\dagger_{\nu,k} \right), \tag{2.12}$$

respectively, where $\lambda_{\nu,k} = q_0 C_{\nu,k} / \sqrt{2 m_{\nu,k} \omega_{\nu,k}}$. Here we have dropped the irrelevant constant zero-point energies. Consequently, we obtained the spin-boson Hamiltonian:

$$H = H_{\rm S} + H_{\rm B} + H_{\rm I}, \tag{2.13}$$

$$H_{\rm S} = -\frac{\Delta}{2}\sigma_x - \epsilon\sigma_z, \tag{2.14}$$

$$H_{\rm B} = \sum_{\nu={\rm L,R}} H_{{\rm B},\nu} = \sum_{\nu,k} \omega_{\nu,k} b^\dagger_{\nu,k} b_{\nu,k}, \tag{2.15}$$

$$H_{\rm I} = \sum_{\nu={\rm L,R}} H_{{\rm I},\nu} = -\frac{\sigma_z}{2} \sum_{\nu,k} \lambda_{\nu,k} \left(b_{\nu,k} + b^\dagger_{\nu,k} \right). \tag{2.16}$$

The reservoir effects are characterized by the spectral density:

$$I(\omega) = \sum_{\nu={\rm L,R}} I_\nu(\omega) = \sum_{\nu={\rm L,R}} \sum_k \lambda^2_{\nu,k} \delta(\omega - \omega_{\nu,k}) = \alpha \tilde{I}(\omega), \tag{2.17}$$

$$\tilde{I}(\omega) = 2\omega \left(\frac{\omega}{\omega_{\rm c}} \right)^{s-1} e^{-\omega/\omega_{\rm c}}, \tag{2.18}$$

where $\alpha = \alpha_{\rm L} + \alpha_{\rm R}$ is the dimensionless coupling strength between the two-state system and the reservoirs, and $\omega_{\rm c}$ is the cutoff frequency. In this thesis, we focus on

the symmetric case ($\varepsilon = 0$) and only use the detuning energy to defined the static susceptibility

$$\chi_0 = \lim_{\varepsilon \to 0} \frac{\langle \sigma_z \rangle}{\varepsilon}, \tag{2.19}$$

where $\langle \cdots \rangle$ denotes an equilibrium average.

2.2 Thermal conductance

In this section, we derive the linear thermal conductance from the spin-boson model. First, based on previous studies [23, 29, 3], we derive the Meir-Wingreen-Landauer formula for the heat current in the Keldysh formalism. The heat current flowing from the reservoir ν into the local two-state system is defined as follows:

$$J_\nu \equiv -\frac{dH_{\mathrm{B},\nu}}{dt} = i[H_{\mathrm{B},\nu}, H] = -i\frac{\sigma_z}{2}\sum_k \lambda_{\nu,k}\omega_{\nu,k}\left(-b_{\nu,k} + b_{\nu,k}^\dagger\right). \tag{2.20}$$

The average of the heat current is written as

$$\langle J_\nu(t) \rangle = \mathrm{Tr}\left[\rho J_\nu(t)\right] = \mathrm{Tr}\left[\rho(t) J_\nu\right], \tag{2.21}$$

Here ρ is the initial-state density matrix

$$\rho = \rho_{\mathrm{S}} \otimes \prod_{\nu=\mathrm{L,R}} \rho_\nu, \tag{2.22}$$

$$\rho_\nu = \frac{1}{Z_\nu} e^{-\beta_\nu H_{\mathrm{B},\nu}}, \tag{2.23}$$

where $\rho(t) = e^{-iH(t-t_0)}\rho e^{iH(t-t_0)}$ and Z_ν is the partition function of the isolated reservoir ν. Hereafter, we consider the average of the observables after realizing the steady state by taking the limit $t_0 \to -\infty$. Substituting the definition of the heat current (2.20) into Eq. (2.21), the heat current is rewritten as

$$\langle J_\nu(t) \rangle = \sum_k \frac{\omega_{\nu,k}\lambda_{\nu,k}}{2}\left[G^<_{\sigma_z, b_{\nu,k}^\dagger}(t_1,t_2) + \left(G^<_{\sigma_z, b_{\nu,k}^\dagger}(t_1,t_2)\right)^*\right]\Big|_{t_1=t_2=t} \tag{2.24}$$

$$= \mathrm{Re}\left[\sum_k \omega_{\nu,k}\lambda_{\nu,k}\, G^<_{\sigma_z, b_{\nu,k}^\dagger}(t_1,t_2)\right]\Big|_{t_1=t_2=t}, \tag{2.25}$$

where $G^<_{\sigma_z, b_{\nu,k}^\dagger}(t_1,t_2)$ is the lesser Green function defined as

$$G^<_{A,B}(t,t') = -i\langle B(t')A(t)\rangle, \tag{2.26}$$

where $A(t) = e^{iHt}Ae^{-iHt}$ and $B(t) = e^{iHt}Be^{-iHt}$. In addition, the retarded and advanced Green functions are defined as

$$G^{\mathrm{r}}_{A,B}(t,t') = -i\theta(t-t')\langle [A(t), B(t')]\rangle, \tag{2.27}$$

$$G^{\mathrm{a}}_{A,B}(t,t') = i\theta(t'-t)\langle [A(t), B(t')]\rangle, \tag{2.28}$$

respectively, where $\theta(t)$ is the Heaviside step function.

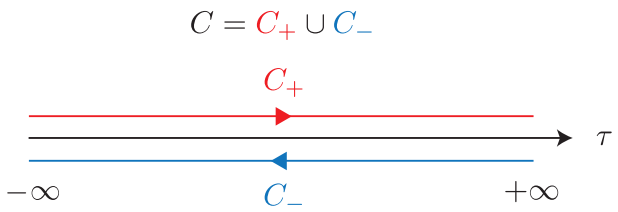

FIGURE 2.3: Keldysh contour C. C_+ is the forward branch and C_- is the backward branch.

Next, let us calculate the lesser Green function $G^<_{\sigma_z, b^\dagger_{\nu,k}}(t_1, t_2)$ in the Keldysh formalism [48]. We introduce the Green function on the Keldysh contour as

$$G_{A,B}(\tau, \tau') = -i \left\langle T_C A(\tau) B(\tau') \right\rangle , \tag{2.29}$$

where T_C is a time-ordered product on the Keldysh contour. The Keldysh contour consists of two oriented branches $C = C_+ \cup C_-$, the forward branch C_+ extending from $-\infty$ to ∞ and the backward branch C_- extending from ∞ to $-\infty$ (see Fig. 2.3). Using the formal expansion with respect to $\lambda_{\nu,k}$, the Green function can be written as

$$G_{\sigma_z, b^\dagger_{\nu,k}}(\tau_1, \tau_2) = -i \left\langle T_C S_C \tilde{\sigma}_z(\tau_1) \tilde{b}^\dagger_{\nu,k}(\tau_2) \right\rangle . \tag{2.30}$$

Here $\tilde{O}(\tau) = e^{i(H_S + H_B)\tau} O e^{-i(H_S + H_B)\tau}$ and S_C is the S-matrix defined as

$$S_C = \sum_{n=0}^{\infty} \frac{(-i)^n}{n!} \int_C du_1 \cdots \int_C du_n \, \tilde{H}_I(u_1) \cdots \tilde{H}_I(u_n), \tag{2.31}$$

where u_i is a time variable on the Keldysh contour and $\int_C du_i$ implies a line integral along the Keldysh contour. Thus, we obtain the relation

$$G_{\sigma_z, b^\dagger_{\nu,k}}(\tau_1, \tau_2) = \frac{\lambda_{\nu,k}}{2} \int_C du \; G_{\sigma_z, \sigma_z}(\tau_1, u) g_{b_{\nu,k}, b^\dagger_{\nu,k}}(u, \tau_2), \tag{2.32}$$

where $g_{b_{\nu,k}, b^\dagger_{\nu,k}}(u, \tau_2)$ is the Green function for the isolated reservoir ν. By projection onto the real-time axis using the Langreth rule [48], the lesser Green function can be written as

$$G^<_{\sigma_z b^\dagger_{\nu,k}}(t_1, t_2) = \frac{\lambda_{\nu,k}}{2} \int_{-\infty}^{\infty} ds \; \left[G^r_{\sigma_z, \sigma_z}(t_1, s) g^<_{b_{\nu,k}, b^\dagger_{\nu,k}}(s, t_2) + G^<_{\sigma_z, \sigma_z}(t_1, s) g^a_{b_{\nu,k}, b^\dagger_{\nu,k}}(s, t_2) \right] . \tag{2.33}$$

Substituting this expression of the lesser Green function (2.33) into Eq. (2.25), the heat current is then rewritten as

$$\begin{aligned}\langle J_\nu(t)\rangle &= \mathrm{Re}\int_{-\infty}^{\infty} ds\ \sum_k \frac{\lambda_{\nu,k}^2}{2}\omega_{\nu,k} \\ &\quad\times\left[G^{\mathrm{r}}_{\sigma_z,\sigma_z}(t_1,s)g^{<}_{b_{\nu,k},b^\dagger_{\nu,k}}(s,t_2)+G^{<}_{\sigma_z,\sigma_z}(t_1,s)g^{\mathrm{a}}_{b_{\nu,k},b^\dagger_{\nu,k}}(s,t_2)\right]\Big|_{t_1=t_2=t} \\ &= \mathrm{Re}\int_{-\infty}^{\infty} ds\ (-i)\frac{\partial}{\partial t_2}\left[G^{\mathrm{r}}_{\sigma_z,\sigma_z}(t_1,s)\Sigma^{<}_\nu(s,t_2)+G^{<}_{\sigma_z,\sigma_z}(t_1,s)\Sigma^{\mathrm{a}}_\nu(s,t_2)\right]\big|_{t_1=t_2=t},\end{aligned} \tag{2.34}$$

where $\Sigma^{<}_\nu(t,t')$ and $\Sigma^{\mathrm{a}}_\nu(t,t')$ are the lesser and advanced self-energies

$$\begin{aligned}\Sigma^{<}_\nu(t,t') &\equiv \sum_k \frac{\lambda_{\nu,k}^2}{2} g^{<}_{b_{\nu,k},b^\dagger_{\nu,k}}(t,t') = -\frac{i}{2}\sum_k \lambda^2_{\nu,k} n_\nu(\omega_{\nu,k})e^{-i\omega_{\nu,k}(t-t')} \\ &= -\frac{i}{2}\int_0^\infty d\omega\ \sum_k \lambda^2_{\nu,k}\delta(\omega-\omega_{\nu,k})n_\nu(\omega)e^{-i\omega(t-t')} \\ &= -\frac{i}{2}\int_0^\infty d\omega\ I_\nu(\omega)n_\nu(\omega)e^{-i\omega(t-t')}, \qquad (2.35) \\ \Sigma^{\mathrm{a}}_\nu(t,t') &\equiv \sum_k \frac{\lambda_{\nu,k}^2}{2} g^{\mathrm{a}}_{b_{\nu,k},b^\dagger_{\nu,k}}(t,t') = \frac{i}{2}\theta(t'-t)\sum_k \lambda^2_{\nu,k} e^{-i\omega_{\nu,k}(t'-t)} \\ &= \frac{i}{2}\theta(t'-t)\int_0^\infty d\omega\ \sum_k \lambda^2_{\nu,k}\delta(\omega-\omega_{\nu,k})e^{-i\omega(t'-t)} \\ &= \frac{i}{2}\theta(t'-t)\int_0^\infty d\omega\ I_\nu(\omega)e^{-i\omega(t'-t)}, \qquad (2.36)\end{aligned}$$

respectively. Here $n_\nu(\omega) = \left(e^{\beta_\nu\omega}-1\right)^{-1}$ is the Bose-Einstein distribution function in reservoir ν. We have used the definition of the spectral density (2.17). Performing a Fourier transform on the heat current (2.34), we obtain

$$\langle J_\nu\rangle = \frac{1}{2}\int_0^\infty d\omega\ \omega I_\nu(\omega)\left[\mathrm{Im}\left[G^{\mathrm{r}}_{\sigma_z,\sigma_z}(\omega)\right]n_\nu(\omega)-\frac{i}{2}G^{<}_{\sigma_z,\sigma_z}(\omega)\right]. \tag{2.37}$$

The conservation law of energy $\langle J_{\mathrm{L}}\rangle = -\langle J_{\mathrm{R}}\rangle \equiv \langle J\rangle$ gives

$$\begin{aligned}\langle J\rangle &= \frac{\alpha_{\mathrm{R}}}{\alpha_{\mathrm{L}}+\alpha_{\mathrm{R}}}\langle J_{\mathrm{L}}\rangle - \frac{\alpha_{\mathrm{L}}}{\alpha_{\mathrm{L}}+\alpha_{\mathrm{R}}}\langle J_{\mathrm{R}}\rangle \qquad (2.38) \\ &= \frac{\alpha_{\mathrm{L}}\alpha_{\mathrm{R}}}{2\left(\alpha_{\mathrm{L}}+\alpha_{\mathrm{R}}\right)}\int_0^\infty d\omega\ \omega\mathrm{Im}\left[G^{\mathrm{r}}_{\sigma_z,\sigma_z}(\omega)\right]\tilde{I}(\omega)\left[n_{\mathrm{L}}(\omega)-n_{\mathrm{R}}(\omega)\right], \qquad (2.39)\end{aligned}$$

where $\tilde{I}(\omega) = \alpha_\nu^{-1}I_\nu(\omega)$ (see Eq. (2.17)). Rewriting $G^{\mathrm{r}}_{\sigma_z,\sigma_z}(\omega)$ with $\chi(\omega)$, we finally obtain

$$\langle J\rangle = \frac{\alpha\gamma}{8}\int_0^\infty d\omega\ \omega\mathrm{Im}\left[\chi(\omega)\right]\tilde{I}(\omega)\left[n_{\mathrm{L}}(\omega)-n_{\mathrm{R}}(\omega)\right], \tag{2.40}$$

where $\alpha = \alpha_{\mathrm{L}}+\alpha_{\mathrm{R}}$, $\gamma = 4\alpha_{\mathrm{L}}\alpha_{\mathrm{R}}/\alpha^2$ is an asymmetric factor, and $\chi(\omega)$ is the dynamical susceptibility of the two-state system defined by

$$\chi(\omega) = -i\int_0^\infty dt\ e^{i\omega t}\left\langle[\sigma_z(t),\sigma_z(0)]\right\rangle. \tag{2.41}$$

This expression of the heat current is called the Meir-Wingreen-Landauer formula. The thermal conductance is defined as

$$\kappa \equiv \lim_{\Delta T \to 0} \frac{\langle J \rangle}{\Delta T}. \tag{2.42}$$

Using the formula (2.40), the linear thermal conductance is given as

$$\kappa = \frac{\alpha \gamma k_B}{8} \int_0^\infty d\omega \, \mathrm{Im}\left[\chi(\omega)\right] \tilde{I}(\omega) \left[\frac{\beta\omega/2}{\sinh(\beta\omega/2)}\right]^2, \tag{2.43}$$

where $\chi(\omega)$ is evaluated for the thermal equilibrium and $\beta = 1/k_B T$. Thus, we need to calculate the dynamical susceptibility, $\chi(\omega)$, for evaluating the linear thermal conductance.

For convenience of discussion, we also introduce a symmetrized correlation function and its Fourier transformation:

$$S(t) \equiv \frac{1}{2} \left\langle \sigma_z(t)\sigma_z(0) + \sigma_z(0)\sigma_z(t) \right\rangle, \tag{2.44}$$

$$S(\omega) = \int_{-\infty}^{\infty} dt \, e^{i\omega t} S(t). \tag{2.45}$$

From the fluctuation-dissipation theorem [15], the imaginary part of the dynamical susceptibility is related to $S(\omega)$ as

$$S(\omega) = \coth\left(\frac{\beta\omega}{2}\right) \mathrm{Im}\left[\chi(\omega)\right]. \tag{2.46}$$

Then, the thermal conductance is rewritten in terms of the symmetrized correlation function, $S(\omega)$, as

$$\kappa = \frac{\alpha \gamma k_B}{8} \int_0^\infty d\omega \, \tanh\left(\frac{\beta\omega}{2}\right) S(\omega) \tilde{I}(\omega) \left[\frac{\beta\omega/2}{\sinh(\beta\omega/2)}\right]^2. \tag{2.47}$$

Chapter 3

Transport Processes and Quantum Critical Phenomena

The dynamics of dissipative two-state systems have long been studied using various approximations [15, 6]. In this chapter, we re-examine such analytical approximations from the viewpoint of heat transport. In Section 3.1, we first consider the effective tunneling amplitude and discuss a quantum phase transition driven by strong system-reservoir coupling. Next, we consider the three mechanisms, which we call 'sequential tunneling' (Section 3.2), 'co-tunneling' (Section 3.3), and 'incoherent tunneling' (Section 3.4). We derive analytical expressions for the thermal conductance in each transport process. We also introduce the noninteracting-blip approximation (NIBA) in Section 3.5.

In Section 3.6, we consider in detail the quantum phase transition for the sub-Ohmic case. In the critical regime near the quantum phase transition, the temperature dependence of thermal conductance becomes power law which is reflected the nature of the quantum phase transition. We derive the critical exponent of the thermal conductance.

3.1 Effective tunneling amplitude

One important effect of the system-reservoir coupling is renormalization of the tunneling amplitude Δ. In this section, we derive the effective tunneling amplitude via adiabatic renormalization [15, 6] (see Fig. 3.1).

We assume that high-frequency oscillators ($\Delta_0 \ll p\omega_c < \omega,\ p \in (0,1)$) instantaneously adjust their quantum states to the current value of σ_z. Then, the two lowest energy eigenstates for the global system are described by

$$|E_g\rangle = \frac{1}{\sqrt{2}}\left(|\Psi_L\rangle + |\Psi_R\rangle\right), \tag{3.1}$$

$$|E_e\rangle = \frac{1}{\sqrt{2}}\left(|\Psi_L\rangle - |\Psi_R\rangle\right), \tag{3.2}$$

where $|\Psi_L\rangle$ and $|\Psi_R\rangle$ are give by

$$|\Psi_L\rangle = |\sigma_z = -1\rangle \otimes \prod_{\nu,k}{}' |\psi^-_{\nu,k}\rangle, \tag{3.3}$$

$$|\Psi_R\rangle = |\sigma_z = +1\rangle \otimes \prod_{\nu,k}{}' |\psi^+_{\nu,k}\rangle, \tag{3.4}$$

respectively. Here the prime symbol indicates that the product is in the range $p\omega_c < \omega_{\nu,k}$. $|\psi^\pm_{\nu,k}\rangle$ is the ground state of the oscillator with wavenumber k in reservoir ν

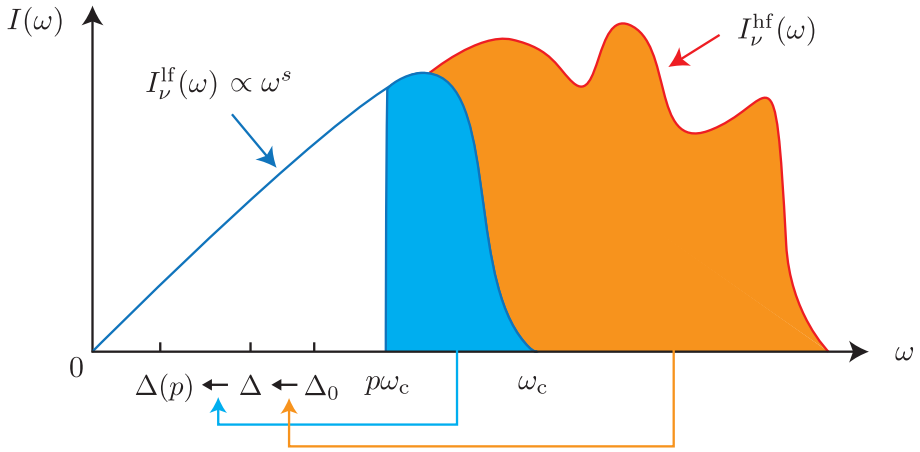

FIGURE 3.1: A conceptual diagram of the adiabatic renormalization. The spectral density is separated into two parts, $I_\nu^0(\omega) = I_\nu^{\rm lf}(\omega) + I_\nu^{\rm hf}(\omega)$. In the first step, the tunneling amplitude Δ_0 is renormalized into the dressed tunneling amplitude Δ by high-frequency oscillators (orange arrow). In the second step, the dressed tunneling amplitude Δ is renormalized into $\Delta(p)$ by oscillators with $p\omega_c < \omega < \omega_c$ (blue arrow). In general, the spectral density with high-frequency oscillators is complex shapes.

when the state of the local two-state system is located at right (left) well; it is obtained by translation of the ground-state wavefunction $|\psi_{\nu,k}^0\rangle$ for the isolated oscillators as

$$|\psi_{\nu,k}^{\pm}\rangle = e^{\pm i\delta_{\nu,k}p_{\nu,k}}\,|\psi_{\nu,k}^0\rangle\,, \tag{3.5}$$

$$\delta_{\nu,k} = \frac{C_{\nu,k}}{m_{\nu,k}\omega_{\nu,k}^2}\frac{q_0}{2} = \frac{1}{\sqrt{2m_{\nu,k}\omega_{\nu,k}}}\frac{\lambda_{\nu,k}}{\omega_{\nu,k}}. \tag{3.6}$$

Adiabatic renormalization suggests that the tunneling amplitude is renormalized by the overlap between the ground states of the oscillators for different localized states ($\sigma_z = \pm 1$):

$$\begin{aligned}
\Delta(p) &= \Delta_0 \prod_{\nu,k}{}' \langle\psi_{\nu,k}^+|\psi_{\nu,k}^-\rangle = \Delta_0 \prod_{\nu,k}{}' \langle\psi_{\nu,k}^0|\, e^{-2i\delta_{\nu,k}p_{\nu,k}}\,|\psi_{\nu,k}^0\rangle \\
&= \Delta_0 \langle\psi_{\nu,k}^0| \exp\left[\sum_{\nu,k}{}' \frac{\lambda_{\nu,k}}{\omega_{\nu,k}}\left(b_{\nu,k}^\dagger - b_{\nu,k}\right)\right]|\psi_{\nu,k}^0\rangle \\
&= \Delta_0 \sum_{n=0}^{\infty}\frac{1}{n!}\langle\psi_{\nu,k}^0|\left[\sum_{\nu,k}{}' \frac{\lambda_{\nu,k}}{\omega_{\nu,k}}\left(b_{\nu,k}^\dagger - b_{\nu,k}\right)\right]^n|\psi_{\nu,k}^0\rangle \\
&= \Delta_0 \sum_{n=0}^{\infty}\frac{1}{n!}\left(-\frac{1}{2}\sum_{\nu,k}{}' \frac{\lambda_{\nu,k}^2}{\omega_{\nu,k}^2}\right)^n = \Delta_0 \exp\left(-\frac{1}{2}\sum_{\nu,k}{}' \frac{\lambda_{\nu,k}^2}{\omega_{\nu,k}^2}\right) \\
&= \Delta_0 \exp\left[-\frac{1}{2}\sum_\nu \int_{p\omega_c}^{\infty} d\omega\, \frac{I_\nu^0(\omega)}{\omega^2}\right].
\end{aligned} \tag{3.7}$$

In general, the spectral density can be separated into two parts (see Fig. 3.1):

$$I_\nu^0(\omega) = I_\nu^{\rm lf}(\omega) + I_\nu^{\rm hf}(\omega), \tag{3.8}$$

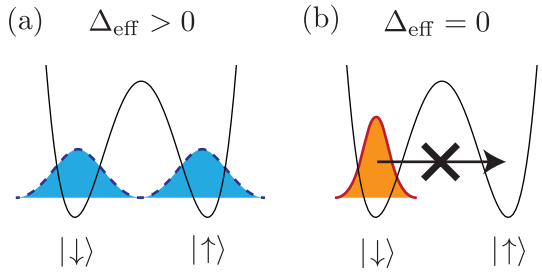

FIGURE 3.2: Schematics of the ground-state wavefunction (a) below the transition ($0 \leq \alpha < \alpha_{\rm c}$) and (b) above the transition ($\alpha > \alpha_{\rm c}$). The former state is delocalized, whereas the latter is localized at one of the two wells. For the localized state, quantum tunneling between the two wells is forbidden since the overlap integral between the states in the two wells vanishes.

where $I_\nu^{\rm lf}(\omega)$ is the spectral density for the low-frequency oscillators and given by the power law behavior (2.18) ($I_\nu^{\rm lf}(\omega) = I_\nu(\omega)$), and $I_\nu^{\rm hf}(\omega)$ represents the high-frequency oscillators and has complex behavior. In the first stage of the adiabatic renormalization procedure, we consider high-frequency oscillators, $\omega > \omega_{\rm c}$, with the spectral density $I_\nu^{\rm hf}(\omega)$. Then, the bare tunneling amplitude, Δ_0, is changed into the dressed tunneling amplitude, Δ, by renormalization of the high-frequency oscillators (the orange arrow in Fig. 3.1):

$$\begin{aligned}
\Delta(p) &= \Delta_0 \exp\left[-\frac{1}{2}\sum_\nu \int_{p\omega_{\rm c}}^\infty d\omega\, \frac{I_\nu^{\rm lf}(\omega) + I_\nu^{\rm hf}(\omega)}{\omega^2}\right] \\
&= \Delta \exp\left[-\frac{1}{2}\sum_\nu \int_{p\omega_{\rm c}}^\infty d\omega\, \frac{I_\nu^{\rm lf}(\omega)}{\omega^2}\right] = \Delta \exp\left[-\frac{1}{2}\sum_\nu \int_{p\omega_{\rm c}}^\infty d\omega\, \frac{I_\nu(\omega)}{\omega^2}\right] \\
&= \Delta \exp\left[-\alpha \int_{p\omega_{\rm c}}^\infty d\omega\, \frac{(\omega/\omega_{\rm c})^{s-1}}{\omega} e^{-\omega/\omega_{\rm c}}\right].
\end{aligned} \tag{3.9}$$

In the second stage, we consider the low-frequency oscillators with the power law spectral density $I_\nu^{\rm lf}(\omega)$ (2.18). If the renormalized tunneling amplitude $\Delta(p)$ is less than $p\omega_{\rm c}$, the adiabatic renormalization can continue by reducing the factor p (the blue arrow in Fig. 3.1). If $\Delta(p^*) = p^*\omega_{\rm c}$ holds at $p = p^*$, adiabatic renormalization must be stopped there and the finite effective tunneling amplitude $\Delta_{\rm eff} = \Delta(p^*)$, which is a characteristic energy scale of the global system, is obtained. In contrast, if $\Delta(p) < p\omega_{\rm c}$ holds for an arbitrary value of p, adiabatic renormalization can be completed even at $p = 0$, yielding an effective tunneling amplitude of zero ($\Delta_{\rm eff} = 0$).

For the Ohmic case ($s = 1$), the effective tunneling amplitude is obtained as follows:

$$\Delta'_{\rm eff} = \begin{cases} \Delta\left(\dfrac{\Delta}{\omega_{\rm c}}\right)^{\alpha/(1-\alpha)}, & (0 < \alpha < 1), \\ 0, & (1 \geq \alpha). \end{cases} \tag{3.10}$$

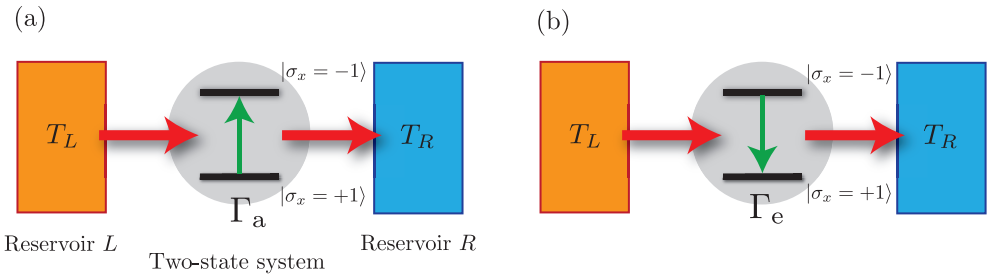

FIGURE 3.3: Schematic of the sequential tunneling process. Heat transport occurs by a combination of (a) phonon (photon) absorption and (b) phonon (photon) emission.

In this thesis, we employ a modified effective tunneling amplitude multiplied by a dimensionless function of α [15]:

$$\Delta_{\text{eff}} = [\Gamma(1-2\alpha)\cos(\pi\alpha)]^{1/2(1-\alpha)}\,\Delta'_{\text{eff}}. \tag{3.11}$$

This result indicates a phase transition at zero temperature, for which the critical value of the system-reservoir coupling is $\alpha = 1$ [49, 50]. For system-reservoir couplings below the transition ($0 < \alpha < 1$), the ground state is non-degenerate, as shown in Fig. 3.2 (a), indicating the coherent superposition of the two localized states $|\uparrow\rangle$ and $|\downarrow\rangle$. We call this ground state 'delocalized'. For strong system-reservoir couplings above the transition ($1 < \alpha$), the coherent superposition of the two localized states is completely broken, leading to the doubly-degenerate ground states shown in Fig. 3.2 (b). We call this ground state 'localized'. In this localized regime, quantum tunneling between the wells is forbidden at zero temperature since there is no mixing ($\Delta_{\text{eff}} = 0$) between the two localized states. Thus, the present quantum phase transition can be recognized as a 'localization' transition that separates the delocalized and localized regimes at zero temperature.

For the sub-Ohmic case ($0 < s < 1$), the adiabatic renormalization always leads to an effective tunneling amplitude of zero ($\Delta_{\text{eff}} = 0$). This is correct in the limit $\Delta/\omega_c \to 0$, as discussed in a previous study [6]. However, for a finite value of Δ/ω_c, the naive adiabatic renormalization procedure yields incorrect results and should be improved. In subsequent theoretical studies [51, 52] , it was found that the localization transition actually occurred at a critical system-reservoir coupling ($\alpha = \alpha_c$), where the critical value α_c depended on both s and Δ/ω_c. The existence of the localization transition was also confirmed via numerical calculations [36, 37]. In summary, for the sub-Ohmic case, the ground state is delocalized for $0 < \alpha < \alpha_c$, as shown in Fig. 3.2 (a), and localized for $\alpha_c < \alpha$ as shown in Fig. 3.2 (b).

For the super-Ohmic case ($s > 1$), the effective tunneling amplitude is always finite:

$$\Delta_{\text{eff}} = \Delta e^{-\alpha\Gamma(s-1)}, \tag{3.12}$$

where $\Gamma(z)$ is the Gamma function. Therefore, there is no localization transition and the ground state is always delocalized, as shown in Fig. 3.2 (a).

3.2 Sequential tunneling

For weak system-reservoir couplings ($\alpha \ll 1$), the system and the reservoirs are almost decoupled and the interaction Hamiltonian $H_{\mathrm{I},\nu}$ can be regarded as a perturbation. For the second-order perturbation, the system dynamics are described by a stochastic transition between the ground state ($\sigma_x = +1$) and the excited state ($\sigma_x = -1$), as shown in Fig. 3.3. The transition from the ground state to the excited state involves phonon (photon) absorption, and the inverse transition involves phonon (photon) emission. A combination of these two processes induces heat transport. We refer to this type of transport process as 'sequential tunneling'. The transition rates for processes of absorption and emission can be calculated using Fermi's golden rule:

$$\Gamma_j = 2\pi \left|\langle f| H_{\mathrm{I}} |i\rangle\right|^2 \delta(\epsilon_f - \epsilon_i), \tag{3.13}$$

where $|i\rangle$ ($|f\rangle$) and ϵ_i (ϵ_f) are eigenstate of $H_{\mathrm{S}} + H_{\mathrm{B}}$ and its eigenvalue, respectively. Introducing the lowering and raising operators

$$\sigma_x^+ \equiv \frac{\sigma_z - i\sigma_y}{2} = \frac{1}{2}\begin{pmatrix} 1 & -1 \\ 1 & -1 \end{pmatrix}, \tag{3.14}$$

$$\sigma_x^- \equiv \frac{\sigma_z + i\sigma_y}{2} = \frac{1}{2}\begin{pmatrix} 1 & 1 \\ -1 & -1 \end{pmatrix}, \tag{3.15}$$

respectively, the interaction Hamiltonian $H_{\mathrm{I},\nu}$ is rewritten in terms of σ_x^+ and σ_x^- as

$$H_{\mathrm{I},\nu} = -\frac{1}{2}\sum_{\nu,k} \lambda_{\nu,k}\left(\sigma_x^+ b_{\nu,k} + \sigma_x^+ b_{\nu,k}^\dagger + \sigma_x^- b_{\nu,k} + \sigma_x^- b_{\nu,k}^\dagger\right). \tag{3.16}$$

Here the second and third terms on the right side of Eq. (3.16) correspond to the process of emission and absorption, respectively. Substituting the expression of the interaction Hamiltonian (3.16) corresponding to the process of emission into Fermi's golden rule (3.13), we obtain the transition rates for process of emission as follows:

$$\begin{aligned}
\Gamma_{\mathrm{e}} &= 2\pi \left| \langle \sigma_x = +1| \otimes \sum_{\nu_2,k_2} \langle n_{\nu_2,k_2}| \left(-\frac{1}{2}\sum_{\nu,k} \lambda_{\nu,k}\sigma_x^+ b_{\nu,k}^\dagger\right) |\sigma_x = -1\rangle \otimes \sum_{\nu_1,k_1} |n_{\nu_1,k_1}\rangle \right|^2 \\
&\quad \times \delta(\omega_{\nu,k} - \Delta) \\
&= 2\pi \sum_{\nu,k}\sum_{\nu_1,k_1}\sum_{\nu_2,k_2} \frac{\lambda_{\nu,k}^2}{4} \left|\langle n_{\nu_2,k_2}| b_{\nu,k}^\dagger |n_{\nu_1,k_1}\rangle\right|^2 \delta(\omega_{\nu,k} - \Delta) \\
&= 2\pi \sum_{\nu,k} \frac{\lambda_{\nu,k}^2}{4} \left[n_{\mathrm{B}}(\omega_{\nu,k}) + 1\right] \delta(\omega_{\nu,k} - \Delta) \\
&= \frac{\pi}{2}\left[n_{\mathrm{B}}(\Delta) + 1\right] \sum_{\nu,k} \lambda_{\nu,k}^2 \delta(\omega_{\nu,k} - \Delta) = \frac{\pi}{2} I(\Delta)\left[n_{\mathrm{B}}(\Delta) + 1\right],
\end{aligned} \tag{3.17}$$

where $I(\omega) = I_{\rm L}(\omega) + I_{\rm R}(\omega)$ and $n_{\rm B}(\omega) = \left(e^{\beta\omega} - 1\right)^{-1}$ is the Bose-Einstein distribution function. Similarly, the rate for the process of absorption is obtained by

$$\begin{aligned}\Gamma_{\rm a} &= 2\pi \left| \langle \sigma_x = -1| \otimes \sum_{\nu_2,k_2} \langle n_{\nu_2,k_2}| \left(-\frac{1}{2} \sum_{\nu,k} \lambda_{\nu,k} \sigma_x^- b_{\nu,k} \right) |\sigma_x = +1\rangle \otimes \sum_{\nu_1,k_1} |n_{\nu_1,k_1}\rangle \right|^2 \\ &\quad \times \delta(\Delta - \omega_{\nu,k}) \\ &= \frac{\pi}{2} I(\Delta) n_{\rm B}(\Delta). \end{aligned} \tag{3.18}$$

For weak system-reservoir coupling, the density matrix of the two-state system can be described by the quantum master equation in the Lindblad form [53]:

$$\frac{d\rho(t)}{dt} = -i\left[H_{\rm S}, \rho(t)\right] + \sum_{j={\rm a,e}} \Gamma_j \left[L_j \rho(t) L_j^\dagger - \frac{1}{2}\left(L_j^\dagger L_j \rho + \rho L_j^\dagger L_j \right) \right], \tag{3.19}$$

where $L_{\rm a} = \sigma_x^-$ and $L_{\rm e} = \sigma_x^+$ are Lindblad operators. Since Hilbert space of the two-state system is spanned by just two states, an excited state $|\sigma_x = -1\rangle$ and a ground state $|\sigma_x = +1\rangle$, it is convenient to represent the density matrix as

$$\rho(t) = \frac{1}{2}\left(1 + \langle \vec{\sigma}(t) \rangle \cdot \vec{\sigma}\right) = \frac{1}{2} \begin{pmatrix} 1 + \langle \sigma_z(t) \rangle & \langle \sigma_x(t) \rangle - i \langle \sigma_y(t) \rangle \\ \langle \sigma_x(t) \rangle + i \langle \sigma_y(t) \rangle & 1 - \langle \sigma_z(t) \rangle \end{pmatrix}. \tag{3.20}$$

With the help of the algebra of the Pauli matrices, the Lindblad equation (3.19) gives the differential equations:

$$\frac{d\langle \sigma_x(t) \rangle}{dt} = \Gamma_{\rm e}\left(1 - \langle \sigma_x(t) \rangle\right) - \Gamma_{\rm a}\left(1 + \langle \sigma_x(t) \rangle\right), \tag{3.21}$$

$$\frac{d\langle \sigma_y(t) \rangle}{dt} = \Delta \langle \sigma_z(t) \rangle - \Gamma \langle \sigma_y(t) \rangle, \tag{3.22}$$

$$\frac{d\langle \sigma_z(t) \rangle}{dt} = -\Delta \langle \sigma_y(t) \rangle - \Gamma \langle \sigma_z(t) \rangle, \tag{3.23}$$

where $\Gamma = (\Gamma_{\rm a} + \Gamma_{\rm e})/2$. We observe that the x-component, $\langle \sigma_x(t) \rangle$, given by Eq. (3.21) decays exponentially with rate 2Γ. The differential equations for y- and z-components (3.22), (3.23) are written in matrix form

$$\frac{d}{dt} \begin{pmatrix} \langle \sigma_z(t) \rangle \\ \langle \sigma_y(t) \rangle \end{pmatrix} = G \begin{pmatrix} \langle \sigma_z(t) \rangle \\ \langle \sigma_y(t) \rangle \end{pmatrix}, \tag{3.24}$$

where G is a coefficient matrix

$$G = \begin{pmatrix} -\Gamma & -\Delta \\ +\Delta & -\Gamma \end{pmatrix}. \tag{3.25}$$

Using the quantum regression theorem [53], which states that the correlation function satisfies the same system of differential equations:

$$\frac{d}{dt} \langle \sigma_i(t) \sigma_j(0) \rangle = \sum_k G_{ik} \langle \sigma_k(t) \sigma_j(0) \rangle, \tag{3.26}$$

we obtain the differential equations for the correlation functions

$$\frac{d}{dt}\langle\sigma_z(t)\sigma_z(0)\rangle = -\Gamma\langle\sigma_z(t)\sigma_z(0)\rangle - \Delta\langle\sigma_y(t)\sigma_z(0)\rangle, \tag{3.27}$$

$$\frac{d}{dt}\langle\sigma_y(t)\sigma_z(0)\rangle = +\Delta\langle\sigma_z(t)\sigma_z(0)\rangle - \Gamma\langle\sigma_y(t)\sigma_z(0)\rangle. \tag{3.28}$$

From Eq. (3.27) and (3.28), under boundary conditions:

$$\langle\sigma_z(0)\sigma_z(0)\rangle = 1, \tag{3.29}$$

$$\frac{d}{dt}\langle\sigma_z(t)\sigma_z(0)\rangle|_{t=0} = 0, \tag{3.30}$$

the z-z correlation function is obtained as

$$\langle\sigma_z(t)\sigma_z(0)\rangle = \frac{1}{\Delta}e^{-\Gamma t}\left[\Delta\cos(\Delta t) + \Gamma\sin(\Delta t)\right]. \tag{3.31}$$

Since the symmetrized correlation function (2.44) has time-reversal symmetry, it is written as

$$S(t) = \langle\sigma_z(|t|)\sigma_z(0)\rangle = \frac{1}{\Delta}e^{-\Gamma|t|}\left[\Delta\cos(\Delta|t|) + \Gamma\sin(\Delta|t|)\right]. \tag{3.32}$$

Performing a Fourier transform on it, we finally derive the symmetrized correlation function as follows:

$$S(\omega) = \frac{4\Gamma(\Delta^2+\Gamma^2)}{\left[(\omega-\Delta)^2+\Gamma^2\right]\left[(\omega+\Delta)^2+\Gamma^2\right]}. \tag{3.33}$$

The correlation function $S(\omega)$ has two peaks at $\omega = \pm\Delta$, reflecting the coherent system dynamics. Because $\Gamma \ll \Delta$ always holds in the weak coupling regime, the correlation function is approximated as

$$S(\omega) \simeq \pi\left[\delta(\omega-\Delta) + \delta(\omega+\Delta)\right], \tag{3.34}$$

where is $\delta(x)$ is the delta function. The thermal conductance for the weak coupling regime is obtained by substituting Eq. (3.34) into Eq. (2.47) as follows

$$\kappa \simeq \frac{\pi\alpha\gamma k_B}{8}\tanh\left(\frac{\beta\Delta}{2}\right)\tilde{I}(\Delta)\left[\frac{\beta\Delta/2}{\sinh(\beta\Delta/2)}\right]^2. \tag{3.35}$$

This result is identical to the formula derived in previous research [29, 7] using the master equation approach and is consistent with the perturbation theory [23]. For actual comparison with the numerical simulation in Section 5, we improve the approximation by replacing Δ with Δ_{eff} using adiabatic renormalization. Then, the symmetrized correlation function is improved to

$$S(\omega) = \frac{4\Gamma(\Delta_{\text{eff}}^2+\Gamma^2)}{\left[(\omega-\Delta_{\text{eff}})^2+\Gamma^2\right]\left[(\omega+\Delta_{\text{eff}})^2+\Gamma^2\right]}. \tag{3.36}$$

For this function to have two peaks at $\omega = \Delta_{\text{eff}}$, it is necessary to hold the condition as follows

$$\Gamma = \frac{\pi}{4}\left[1+2n_B(\Delta_{\text{eff}})\right]I(\Delta_{\text{eff}}) \ll \Delta_{\text{eff}}. \tag{3.37}$$

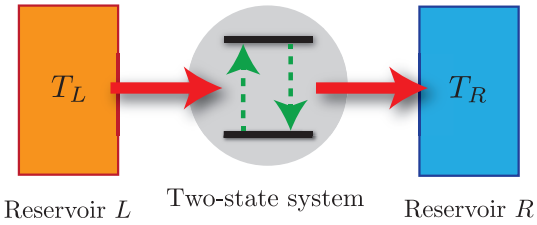

FIGURE 3.4: Schematic of the co-tunneling process. At $k_B T \ll \Delta_{\rm eff}$, heat transport via a virtual excitation in the local system is dominant.

For the sub-Ohmic case ($s < 1$), this condition is never satisfied, indicating the absence of a sequential tunneling regime. For the Ohmic case ($s = 1$), the condition is equivalent to $\alpha \ll 1$, whereas for the super-Ohmic case ($s > 1$), the condition is always satisfied for a moderate temperature ($k_B T \sim \Delta_{\rm eff}$). At high temperatures ($k_B T \gg \Delta_{\rm eff}$), the condition is always satisfied for $s \geq 2$, whereas for $1 < s < 2$, it becomes

$$T < T^* = \frac{\omega_c}{\alpha k_B} \left(\frac{\Delta_{\rm eff}}{\omega_c} \right)^{2-s}. \tag{3.38}$$

where T^* is the crossover temperature.

The formula for sequential tunneling (3.35) predicts the exponential decrease in the thermal conductance as the temperature is lowered. At low temperatures, the thermal conductance behaves as $\kappa \propto e^{-\Delta_{\rm eff}/k_B T}/T^2$; this is because the transition from the ground state to the excited state is strongly suppressed if the thermal fluctuation is smaller than the effective energy splitting, i.e., when $k_B T \ll \Delta_{\rm eff}$. When the sequential tunneling process is strongly suppressed at low temperatures, Eq. (3.35) becomes invalid since another process becomes dominant, as discussed in the next subsection.

3.3 Co-tunneling

At low temperatures, heat transport via the virtual excitation of the local two-state system becomes dominant (see Fig. 3.4); this transport process is known as 'co-tunneling'. In a previous study [23], an analytical expression for the thermal conductance was derived using the fourth-order perturbation theory with respect to the interaction $H_{I,\nu}$. However, in this calculation, the renormalization of the tunneling amplitude at a low temperature has not been considered.

Here, we derive an asymptotically exact formula for the thermal conductance without any approximations [54]. For this purpose, we focus on an asymptotically exact relation called the generalized Shiba relation [55, 56]:

$$\lim_{\omega \to 0+} \frac{S(\omega)}{\tilde{I}(\omega)} = \pi \alpha \left(\frac{\chi_0}{2} \right)^2, \tag{3.39}$$

where χ_0 is the static susceptibility defined in Eq. (2.19). This exact relation holds at low temperatures ($k_B T \ll \Delta_{\rm eff}$) for arbitrary environments and arbitrary system-reservoir couplings. At low temperatures ($k_B T \ll \Delta_{\rm eff}$), the dominant contribution to the integral of Eq. (2.47) comes from the low-frequency part ($0 \leq \omega \simeq k_B T \ll \Delta_{\rm eff}$)

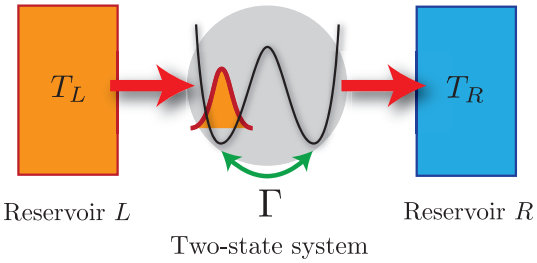

FIGURE 3.5: Schematic of the incoherent tunneling process. The wavefunction is localized in the two wells, and a stochastic transition occurs between them.

due to the factor of the Bose-Einstein distribution function. By substituting the low-frequency asymptotic form $S(\omega) \simeq \pi\alpha \left(\chi_0/2\right)^2 \tilde{I}(\omega)$ into Eq. (2.47), we obtain [54]

$$\kappa \simeq \frac{\pi k_{\rm B}\chi_0^2}{8} \int_0^\infty d\omega \; I_{\rm L}(\omega) I_{\rm R}(\omega) \left[\frac{\beta\omega/2}{\sinh(\beta\omega/2)}\right]^2. \tag{3.40}$$

This expression is similar to the co-tunneling formula in previous studies [23, 57] but significantly differs in terms of the static susceptibility, χ_0, which considers higher-order processes. Eq. (3.40) can be rewritten as

$$\kappa \simeq \frac{1}{2}\pi k_{\rm B}\alpha_{\rm L}\alpha_{\rm R}\omega_{\rm c}^3\chi_0^2 \left(\frac{k_{\rm B}T}{\omega_{\rm c}}\right)^{2s+1} F(s), \tag{3.41}$$

$$F(s) = \int_0^\infty dx \; x^{2s} \left[\frac{x/2}{\sinh(x/2)}\right]^2, \tag{3.42}$$

where $F(s)$ is a dimensionless function of s. Thus, we find that the thermal conductance is proportional to T^{2s+1} at low temperatures. The same temperature dependence has been derived by the perturbation theory [23, 57]. However, the perturbation theory cannot treat renormalization effect due to higher-order processes on the static susceptibility and fails in predicting a correct prefactor including χ_0. In contrast, the present result given in Eq. (3.40) is asymptotically exact, incorporating the renormalization effect appropriately.

The co-tunneling formula (3.40) holds universally at low temperatures for an arbitrary exponent, s, as long as the ground state of the system is delocalized ($\Delta_{\rm eff} > 0$). In a previous study [29], the thermal conductance in the Ohmic case ($s = 1$) was shown to be proportional to T^3, which is consistent with Eq. (3.40), and this T^3-dependence was discussed in terms of the emergence of the Kondo effect. However, it is worth noting that the power-law temperature dependences are derived in a unified way even in the non-Ohmic cases. These temperature dependences result from non-trivial many-body effects due to strong mixing between the system and the reservoirs.

3.4 Incoherent tunneling

For a strong reservoir-system coupling, the coherent superposition of the two localized states is completely broken. In such a situation, heat transport is induced by stochastic dynamics between the two localized states $|\uparrow\rangle$ and $|\downarrow\rangle$, as shown in Fig. 3.5. We call this transport process 'incoherent tunneling'.

Within the Markov approximation [58], the stochastic dynamics of the system is described by the master equation:

$$\frac{dP_{\rm L}(t)}{dt} = -\Gamma P_{\rm L}(t) + \Gamma P_{\rm R}(t), \quad \frac{dP_{\rm R}(t)}{dt} = \Gamma P_{\rm L}(t) - \Gamma P_{\rm R}(t), \tag{3.43}$$

where $P_{\rm L}(t)$ and $P_{\rm R}(t)(= 1 - P_{\rm L}(t))$ are the probabilities that the wavefunction of the system is localized at the well on the left-hand side ($\sigma_z = -1$) and that on the right-hand side ($\sigma_z = +1$), respectively, at time t. The transition rate Γ is calculated via second-order perturbation with respect to the Hamiltonian $H_{\rm S}$ as follows [6]:

$$\Gamma = \frac{\Delta^2}{2}\int_{-\infty}^{\infty} d\tau\, e^{-Q'(\tau)} \cos\left[Q''(\tau)\right], \tag{3.44}$$

$$Q'(\tau) = \int_0^{\infty} d\omega\, \frac{I(\omega)}{\omega^2} \coth\left(\frac{\beta\omega}{2}\right)\left[1-\cos(\omega\tau)\right], \tag{3.45}$$

$$Q''(\tau) = \int_0^{\infty} d\omega\, \frac{I(\omega)}{\omega^2} \coth\left(\frac{\beta\omega}{2}\right)\sin(\omega\tau). \tag{3.46}$$

Note that this expression for the transition rate of incoherent tunneling is valid when $\Gamma \ll k_{\rm B}T$ [58]. By solving the master equation (3.43), the symmetrized correlation function is calculated as

$$S(\omega) = \frac{4\Gamma}{\omega^2 + 4\Gamma^2}. \tag{3.47}$$

In contrast to sequential tunneling, $S(\omega)$ has only one peak at $\omega = 0$ with a width of 2Γ, indicating the destruction of the superposition of the two localized states.

The long-term dynamics are well described by the Markov approximation [6]. Therefore, one may expect that the thermal conductance in the incoherent tunneling regime would be well approximated by substituting Eq. (3.44) into Eq. (2.47). However, the results of the Markov approximation show clear deviation from the numerical results, as discussed in Section 5. The reason for this is summarized as follows. Note that incoherent tunneling occurs when $\Gamma \ll k_{\rm B}T$. Under this condition, the integrand of Eq. (2.47) is proportional to ω^{s-2} for $\Gamma \ll \omega \ll k_{\rm B}T$ since $S(\omega) \propto \omega^{-2}$ (see Eq. (3.47)). Then, the integral in Eq. (2.47) diverges if the high-frequency cutoff occurring due to the Bose-Einstein distribution function is absent. This indicates that the high-frequency part of the integral in Eq. (2.47) makes the dominant contribution to the thermal conductance. Although the Markov approximation yields reasonable results for the low-frequency behavior of $S(\omega)$, it fails to reproduce the accurate high-frequency behavior of $S(\omega)$ in general, leading to incorrect results for the thermal conductance.

3.5 Noninteracting-blip approximation (NIBA)

To study the short-term (high-frequency) dynamics in the incoherent tunneling regime, we introduce the noninteracting-blip approximation (NIBA), which is a natural extension of the Markov approximation in the previous section [6, 15]. In the NIBA, the Fourier transformation of the symmetrized correlation function is expressed as [15] (the detail derivation is given in Appendix C)

$$S(\omega) = 2{\rm Re}\left[\frac{1}{-i\omega + \Sigma(-i\omega)}\right], \tag{3.48}$$

where $\Sigma(\lambda = -i\omega)$ is the frequency-dependent self-energy defined as

$$\Sigma(\lambda) = \Delta^2 \int_0^\infty d\tau\, e^{-\lambda\tau} e^{-Q'(\tau)} \cos\left[Q''(\tau)\right]. \tag{3.49}$$

Here, $Q'(\tau)$ and $Q''(\tau)$ are given by Eqs. (3.45) and (3.46), respectively. The thermal conductance is then calculated by substituting Eq. (3.48) and (3.49) into Eq. (2.47). From the definition, it is easy to check that the NIBA reproduces the Markov approximation if one neglect the frequency dependence of the self-energy and replace it with the zero-frequency value $\Sigma(0) = 2\Gamma$. Since the NIBA appropriately considers the non-Markovian properties, it is suitable to describe the thermal conductance in the incoherent tunneling regime.

The condition for the NIBA is well known [15, 6]. As expected from the fact that the NIBA is an extension of the Markov approximation, it works well for the incoherent tunneling regime. Roughly, the incoherent tunneling mechanism becomes crucial in a regime wherein both the sequential tunneling formula and the co-tunneling formula fail. (a) The NIBA holds at moderate-to-high temperatures in the sub-Ohmic ($0 < s < 1$) and Ohmic cases ($s = 1$). (b) It holds for $T > T^*$ in the super-Ohmic case of $1 < s < 2$, where T^* is the crossover temperature defined in Eq. (3.38). Note that the NIBA never holds for $s \geq 2$ since the crossover temperature T^* diverges.

Here, the NIBA has been introduced to improve the Markov approximation in the incoherent regime. This introduction of the NIBA may give an impression to the readers that the NIBA is a good approximation only in the incoherent regime. However, the NIBA is known to be applicable for a wider parameter region not restricted to the incoherent regime [15, 6]. The NIBA holds also in the weak coupling regime ($\alpha \ll 1$) at arbitrary temperature for the unbiased case ($\epsilon = 0$), where the interblip interaction is shown to be much weaker than the intrablip interaction. For this reason, the NIBA yields almost the same result as the sequential tunneling formula or the co-tunneling formula if the system-reservoir coupling is sufficiently weak.

In Section 5, we show that the NIBA is an excellent approximation for reproducing the numerical results for a wide region of the parameter space at moderate-to-high temperatures. Thus, the short-term (high-frequency) non-Markovian behavior in the system dynamics is important for calculating the thermal conductance in the incoherent tunneling regime.

3.6 Quantum critical phenomena for the sub-Ohmic case

We explained three tunneling processes (sequential tunneling, co-tunneling, and incoherent tunneling) and derived the analytical expressions for the thermal conductance in each transport process. However, the temperature dependence of the thermal conductance near the quantum phase transition for the sub-Ohmic case (as described in Section 3.1) has not been discussed. In this section, we discuss quantum critical phenomena induced by the second-order phase transition for the sub-Ohmic case at zero temperature and determine the critical exponent of the thermal conductance using other critical exponents discussed in Section 1.5. In the quantum critical regime near the quantum phase transition, the thermal conductance exhibits a distinctive power-law temperature dependence reflecting the nature of the quantum phase transition:

$$\kappa \propto T^c, \ (\alpha = \alpha_c) \tag{3.50}$$

where c is the critical exponent dependent on s.

Let us discuss the critical exponent, c, defined in Eq. (3.50). The static susceptibility defined in Eq. (2.19) is rewritten by

$$\chi_0 = \beta \langle \bar{\sigma}_z^2 \rangle_{\rm eq}, \tag{3.51}$$

$$\bar{\sigma}_z = \frac{1}{\beta} \int_0^\beta d\tau\, \sigma_z(\tau). \tag{3.52}$$

where $\langle \cdots \rangle_{\rm eq}$ indicates the thermal average and $\sigma_z(\tau)$ is the imaginary time path. Combining Eq. (3.51) with (3.52), the static susceptibility is expressed as

$$\chi_0 = \int_0^\infty d\tau\, C(\tau), \tag{3.53}$$

where $C(\tau)$ is the correlation function $C(\tau) \equiv \langle \sigma_z(\tau)\sigma_z(0)\rangle_{\rm eq}$. At the critical point, the correlation function exhibits the power-law decay:

$$C(\tau) = C(\beta - \tau) \sim \tau^{-\eta},\ (\omega_{\rm c}^{-1} \ll \tau \ll \beta/2), \tag{3.54}$$

where η is the critical exponent (1.21). Then, the temperature dependence of the static susceptibility at the critical point is obtained:

$$\chi_0 \sim \beta^{1-\eta}. \tag{3.55}$$

By using the Fourier transformation of the correlation function:

$$C(i\omega_n) = \int_0^\beta d\tau\, e^{i\omega_n \tau} C(\tau), \tag{3.56}$$

the critical behavior of the imaginary part of the dynamical susceptibility $\chi(\omega) = C(i\omega_n \to \omega + i\delta)$ is obtained:

$$\mathrm{Im}\,[\chi(\omega)] \sim \omega^{\eta-1}. \tag{3.57}$$

Substituting this into Eq. (2.43), the thermal conductance at the critical point behaves as $\kappa \sim T^c$, where the exponent is given by:

$$c = s + \eta. \tag{3.58}$$

The critical exponent η is a function of s and has been analyzed in previous theoretical studies [37, 41]. The phase transition for $0 < s \leq 0.5$ belongs to the mean-field universality class and leads to $\eta = 1/2$ (see Eq. (1.22)). For $0.5 < s < 1$, η is a nontrivial function of s and is evaluated by the ε-expansion (see Eq. (1.24)) [41]. In summary, the exponent of the thermal conductance is given as follows:

$$c = \begin{cases} s + \dfrac{1}{2}, & (0 < s \leq 0.5), \\ 1 - \dfrac{1}{2}\varepsilon - \dfrac{A(s)}{3s}\varepsilon^2 + \mathcal{O}(\varepsilon^3), & (s > 0.5), \end{cases} \tag{3.59}$$

where $\varepsilon = 2s - 1$, $A(s) = s\,[\psi(1) - 2\psi(s/2) + \psi(s)]$, and $\psi(z)$ is the digamma function. The detail has been discussed using the numerical calculations in Ref. [41].

Chapter 4

Continuous-time Quantum Monte Carlo Method

While the analytical approaches discussed in the previous section are sufficiently powerful for clarifying the mechanism of heat transport in a two-state system, the detailed conditions justifying each approximation are not trivial. To understand all features of heat transport, unbiased numerical simulation without any approximation would be helpful. In this thesis, we employ the continuous-time Monte Carlo (CTQMC) algorithm [59]. According to this algorithm, the partition function is rewritten in path integral form with respect to an imaginary time path, $\sigma_z(\tau)$, (kink representation) and the weight of this path is defined. We describe the way to calculate the imaginary part of the dynamical susceptibility, $\mathrm{Im}\,[\chi(\omega)]$, by applying the Monte Carlo method to the kink representation using the cluster update algorithm [37]. In addition, we explain the way to determine the critical point of the quantum phase transition for the sub-Ohmic case.

4.1 The kink representation of the spin-boson model

The partition function of the spin-boson model (2.13) is written in the imaginary time path integral form as [15, 37] (for the detained derivation, see Appendix B)

$$Z = \mathrm{Tr}\left[e^{-\beta H}\right] = \int \mathcal{D}\sigma_z(\tau)\, e^{-S[\sigma_z(\tau)]}, \tag{4.1}$$

$$S\left[\sigma_z(\tau)\right] = -\frac{1}{4}\int_0^\beta d\tau \int_0^\tau d\tau'\, \sigma_z(\tau) K(\tau-\tau')\sigma_z(\tau'), \tag{4.2}$$

where $\sigma_z(\tau)$ is a spin path defined on the imaginary time axis, $\mathcal{D}\sigma_z(\tau)$ indicates the integral measure for all possible paths $\sigma_z(\tau)$, $S\left[\sigma_z(\tau)\right]$ is a influence function, and $K(\tau)$ is a kernel defined as

$$K(\tau) = \int_0^\infty d\omega\, I(\omega) \frac{\cosh\left[\omega(\beta/2-\tau)\right]}{\sinh(\beta\omega/2)}. \tag{4.3}$$

The kernel has the symmetry $K(\tau) = K(\beta-\tau)$ and asymptotic form $K(\tau) \sim \tau^{-(1+s)}$ for $\omega_c^{-1} \ll \tau \ll \beta/2$. Note that the partition function (4.1) shows the equivalence between the spin-boson model and the ferromagnetic Ising model with the long-range spin-spin interaction $K(\tau)$ [60].

To apply the CTQMC method, we change over from the spin representation (4.1) to the kink representation. As shown in Fig. 2.1 (a), the path $\sigma_z(\tau)$ is assigned by an alternative configuration of kinks (jumps from $\sigma_z = -1$ to $\sigma_z = +1$) and anti-kinks (jumps from $\sigma_z = +1$ to $\sigma_z = -1$) and described by the positions τ_i ($i = 1, 2, \ldots, 2n$)

of the kinks ($q_i = +1$) and anti-kinks ($q_i = -1$). Thus, the derivative of the spin path reads

$$\frac{d\sigma_z(\tau)}{d\tau} = \sum_{i=1}^{2n} 2q_i\delta(\tau - \tau_i), \tag{4.4}$$

where n is the number of the pairs of kinks and anti-kinks. By substituting Eq. (4.4) into (4.1), we obtain the kink representation of the partition function:

$$Z = \sum_{n=0}^{\infty} \left(\frac{\Delta}{2}\right)^{2n} \int_0^{\beta} d\tau_{2n} \int_0^{\tau_{2n}} d\tau_{2n-1} \cdots \int_0^{\tau_2} d\tau_1 \ \exp\left[\sum_{\langle i,j\rangle}^{2n} q_i q_j W(\tau_i - \tau_j)\right], \tag{4.5}$$

where $W(\tau)$ is obtained from the relation $W''(\tau) = -K(\tau)$ as

$$W(\tau) = \int_0^{\infty} d\omega \ \frac{I(\omega)}{\omega^2} \frac{\cosh(\beta\omega/2) - \cosh[\omega(\beta/2 - \tau)]}{\sinh(\beta\omega/2)}. \tag{4.6}$$

4.2 Calculation algorithm

We apply the CTQMC method to the partition function for the kink representation (4.5). The present CTQMC algorithm [59] employs a cluster-flip update similar to that in the Swendsen–Wang cluster algorithm [61]. Employing this algorithm, we can overcome the problem of the critical slowing down (the correlation time diverges near the critical point of second-order phase transition). The cluster-flip update is constructed as follows [37] (see Fig. 4.1):

1. Inserting new vertices with Poisson statics given by $P(\Delta\tau) = \Gamma e^{-\Gamma\Delta\tau}$ with mean value $\Gamma^{-1} = 2/\Delta$.

2. Connecting two segments (the line segments between neighboring vertices), s_i and s_j, with the probability

$$p[s_i, s_j] = 1 - \delta_{\sigma_z(s_i),\sigma_z(s_j)}\left[1 - e^{-2A}\right], \tag{4.7}$$

$$A = W(\tau_{i-1} - \tau_{j-1}) - W(\tau_{i-1} - \tau_j) - W(\tau_i - \tau_{j-1}) + W(\tau_i - \tau_j), \tag{4.8}$$

   where $\sigma_z(s_i)$ is the value of σ_z in the segment s_i, and positions of the vertices at the two edges of the segment s_i are denoted by τ_{i-1} and τ_i, respectively.

3. Flipping each segment cluster with probability $1/2$.

4. Removing the redundant vertices within segments.

The Monte Carlo data presented in this paper typically represent averages over 10^3-10^4 updates at low temperatures and 10^7–10^8 updates at high temperatures.

Using the CTQMC sampling method, we evaluate the spin correlation function $C(i\omega_n)$ defined in Eq. (3.56) as follows:

$$C(i\omega_n) = \frac{1}{\beta\omega_n^2}\left\langle |\rho(i\omega_n)|^2 \right\rangle, \tag{4.9}$$

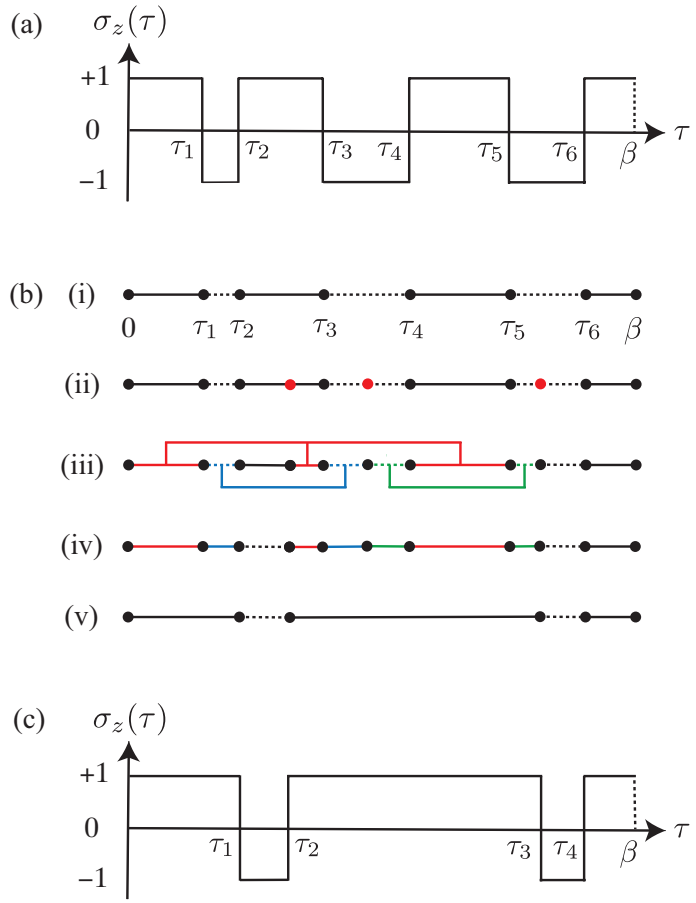

FIGURE 4.1: The spin path on the imaginary time axis for the spin-boson model and the CTQMC update process: (a) An initial spin path, (b-i) the vertex representation of (a), (b-ii) insertion of new cuts using the Poisson distribution, (b-iii) connection of segments with the probability (4.7), (b-iv) flipping each cluster with probability 1/2, (b-v) removal of redundant cuts, and (c) the final spin path after the update.

where $\langle \cdots \rangle$ denotes the average obtained via CTQMC sampling and $\rho(i\omega_n)$ is the Fourier transformation of $\rho(\tau) = d\sigma_z(\tau)/d\tau$. From Eq. (4.4), $\rho(i\omega_n)$ is expressed as

$$\rho(i\omega_n) = \sum_{j=1}^{2n} 2(-1)^j e^{i\omega_n \tau_j}. \tag{4.10}$$

Then, to evaluate the thermal conductance (2.43) numerically, we need to calculate as follows:

1. Calculating the Fourier transformation of the correlation function, $C(i\omega_n)$, from Eq. (4.9).

2. Performing the analytical continuation

$$\chi(\omega) = C(i\omega_n \to \omega + i\delta). \tag{4.11}$$

3. Evaluating the thermal conductance from Eq. (2.43).

For using the co-tunneling formula (3.40), we need to calculate the static susceptibility χ_0. Typically, a simple estimate $\chi_0 \simeq 2/\Delta_{\rm eff}$ yields quantitatively correct results. However, for the sub-Ohmic case, χ_0 has non-trivial temperature dependence, even at low temperatures. For this case, we numerically calculate the static susceptibility, χ_0, using the CTQMC method as follows:

$$\chi_0 = \beta \langle \bar{\sigma}_z^2 \rangle , \tag{4.12}$$

$$\bar{\sigma}_z = \frac{1}{\beta}\int_0^\beta d\tau\, \sigma_z(\tau) = \frac{2}{\beta}\sum_{j=0}^{2n-1}(-1)^j \tau_j + 1. \tag{4.13}$$

4.3 Analytical continuation

To obtain the dynamical susceptibility, $\chi(\omega)$, we need to perform the analytical continuation (4.11). If the analytical expression for the Fourier transformation of the correlation function, $C(i\omega_n)$ is clarified, we have only to replace $i\omega_n$ with $\omega + i\delta$. However, since the Fourier transformation of the correlation function includes numerical errors, the analytical continuation is difficult. In this thesis, we usually employ Padé approximation [62].

In Padé approximation, given values of the analytical function for upper half plane $F(z)$ at $z = i\omega_n$ ($n = 0, 1, \ldots, N$) numerically, $F(\omega)$ is approximated by a continued fractional function:

$$G_N(\omega) = \frac{a_1}{1+}\frac{a_2(\omega - z_1)}{1+}\cdots\frac{a_N(\omega - z_{N-1})}{1}, \tag{4.14}$$

where a_i are coefficients determined by $G_N(\omega)$. Using Thiele's reciprocal difference algorithm, we can determine coefficients a_i as follows. We introduce a function

$$g_1(z_n) = F(z_n), \tag{4.15}$$

and define sequentially functions

$$g_n(z_n) = \frac{g_{n-1}(z_{n-1}) - g_{n-1}(\omega)}{(\omega - z_{n-1})g_{n-1}(\omega)}. \tag{4.16}$$

Then, coefficients a_i are obtained by

$$a_i = g_i(z_i). \tag{4.17}$$

In this thesis, $F(z)$ and $G_N(\omega)$ correspond to the Fourier transformation of the correlation function $C(i\omega_n)$ and dynamical susceptibility $\chi(\omega)$, respectively.

For the weak coupling regime, however, Padé approximation yields poor results since the imaginary part of the pole nearest to the real frequency axis is small. In this case, we employ another approximation based on the fitting [63]. We assume that the Fourier transformation if the correlation function as

$$C(i\omega_n) \simeq \frac{a\omega_0^3}{(\omega_n + \lambda)^2 + \omega_0^3} + \text{const}, \tag{4.18}$$

where a, ω_0, and λ are the fitting parameters determined using the least-squares method. It is easy to obtain the imaginary part of the dynamical susceptibility $\mathrm{Im}\,[\chi(\omega)]$ using the fitting function (4.18) with optimized parameters. Note that

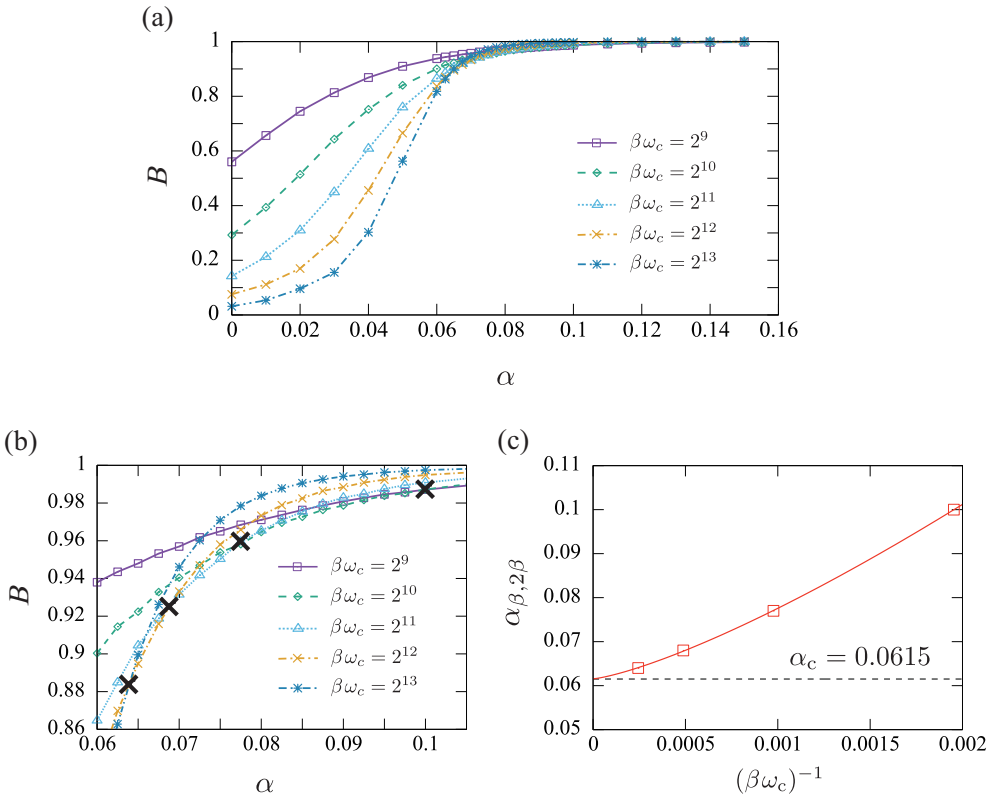

FIGURE 4.2: An example of the Binder parameter analysis. The results for $s = 0.6$ and $\Delta/\omega_c = 0.01$ are shown. (a) The Binder parameter as a function of the coupling constant α for different temperatures. (b) Enlarged view of (a) around $\alpha = 0.08$. Crosses represent the intersection points $\alpha_{\beta,2\beta}$ between the two neighboring inverse temperature, $\beta\omega_c$ and $2\beta\omega_c$, respectively. (c) The intersection points of the Binder parameters. The red solid curve shows the fitted quadratic function. The dashed horizontal line indicates the critical value $\alpha_c = 0.0615$ obtained via the present analysis.

this fitting method works well for weak couplings since it is compatible with the dynamic susceptibility for the sequential tunneling process.

4.4 Binder analysis

In this section, we describe how to determine the critical point of the quantum phase transition for the sub-Ohmic case ($0 < s < 1$) [37]. To study this quantum phase transition, we utilize the finite size scaling form for observable O close to the critical point

$$\langle O \rangle (T, \alpha) = \beta^{x_O} f_O(\beta^{y_t^*} \delta), \tag{4.19}$$

where $\delta = (\alpha - \alpha_c)/\alpha_c$ denotes the distance from the critical point, x_O and f_O are the scaling exponent and scaling function of the observable O, respectively. The exponent y_t^* is related to the correlation length exponent ν, $\xi \sim \delta^{-\nu}$ at $\delta \simeq 0$, as

follows [37, 41, 42]:

$$y_t^* = \begin{cases} \dfrac{1}{\nu}, & (0 < s \leq 0.5), \\ \dfrac{1}{\nu} + \dfrac{1}{2} - s, & (s > 0.5). \end{cases} \tag{4.20}$$

We introduce the Binder parameter, which is defined as follows:

$$B = \frac{1}{2}\left(3 - \frac{\langle \bar{\sigma}_z^4 \rangle}{\langle \bar{\sigma}_z^2 \rangle^2}\right), \tag{4.21}$$

where $\bar{\sigma}_z = \beta^{-1} \int d\tau\, \sigma_z(\tau)$ indicates the average obtained via the Monte Carlo sampling. Since the Binder parameter has $x_B = 0$, the critical point $\delta = 0$ ($\alpha = \alpha_c$) is determined as the point for which the Binder parameter is independent of the temperature at sufficiently low temperatures. In Fig. 4.2, we show an example of the Binder analysis for $s = 0.6$ and $\Delta/\omega_c = 0.01$. The curve of the Binder parameter for different temperatures has intersection points around $\alpha = 0.08$, as shown in Fig. 4.2 (a). To accurately determine the critical point, we consider the intersection points $\alpha_{\beta,2\beta}$ between the two neighboring inverse temperatures, β and 2β (see Fig. 4.2 (b)), and plot the intersection points as a function of $(\beta\omega_c)^{-1}$, as shown in Fig. 4.2 (c). By extrapolating $\alpha_{\beta,2\beta}$ in the limit $(\beta\omega_c)^{-1} \to 0$ using fitting to the quadratic function of $(\beta\omega_c)^{-1}$, the critical value $\alpha_c = 0.0615$ is obtained for this parameter set.

Chapter 5

Numerical Results and Comparison with Analytical Formulas

In this chapter, we perform numerical simulations based on the CTMQC method and compare the simulation results with the analytical formulas introduced in Section 3. We separately consider the Ohmic (Section 5.1.1), sub-Ohmic (Section 5.1.2), and super-Ohmic cases (Sections 5.1.3 and 5.1.4). The dynamics of the spin-boson model has been studied by using various numerical methods. However, no systematic comparisons between analytical approximations and numerical simulations have been performed in the context of heat transport near thermal equilibrium. This comparison allows us to discuss the validity of various approximations critically.

In Section 5.2, we show numerical results near the quantum phase transition point for the sub-Ohmic case and compare them with the analytical temperature dependence of the thermal conductance discussed in Section 3.6.

5.1 Thermal conductance

5.1.1 The Ohmic case $(s = 1)$

In Fig. 5.1, we show the thermal conductances for $\alpha = 0.05$, 0.1, 0.5, and 0.7 as functions of temperature. We plot the graph using the normalized temperature $k_{\mathrm{B}}T/\Delta_{\mathrm{eff}}$ and the normalized thermal conductance $\kappa/(k_{\mathrm{B}}\gamma\Delta_{\mathrm{eff}})$, where Δ_{eff} is the effective tunneling amplitude defined in Eq. (3.11). As shown in Fig. 5.1, the numerical results fall on a universal scaling curve at each value of α regardless of the ratio $\Delta/\omega_{\mathrm{c}}$ ($\Delta/\omega_{\mathrm{c}} \ll 1$) obtained via this normalization. This universal behavior is characteristic of the Kondo-like effect [29]. In Fig. 5.1 (c), we also show the exact solution (the Toulouse point) for $\alpha = 0.5$ (indicated by the brown dotted–dashed line) [15, 29, 63]. The agreement between the numerical results and the exact solution indicates the correctness of the CTQMC simulation.

At low temperatures ($k_{\mathrm{B}}T \ll \Delta_{\mathrm{eff}}$), the numerical results agree well with those of the approximate formula for the co-tunneling process (Eq. (3.41); indicated by blue dashed lines in Fig. 5.1). In this regime, the thermal conductance is always proportional to T^3 ($= T^{2s+1}$), which is consistent with the previous study [29].

At moderate ($k_{\mathrm{B}}T \sim \Delta_{\mathrm{eff}}$) and high temperatures ($k_{\mathrm{B}}T \gg \Delta_{\mathrm{eff}}$), the numerical results deviate from the co-tunneling formula and agree well with the NIBA (indicated by black solid lines in Fig. 5.1). Note that the thermal conductance obtained by the NIBA is proportional to $T^{3-2\alpha}$ at low temperatures, as shown in Fig. 5.1. The NIBA agrees well even with the low-temperature numerical results for the weak system-reservoir coupling ($\alpha \ll 1$), whereas it deviates from these results as this coupling becomes large. It is remarkable that the NIBA agrees well with the numerical results at arbitrary temperatures for $\alpha \ll 1$, as shown in Fig. 5.1 (a).

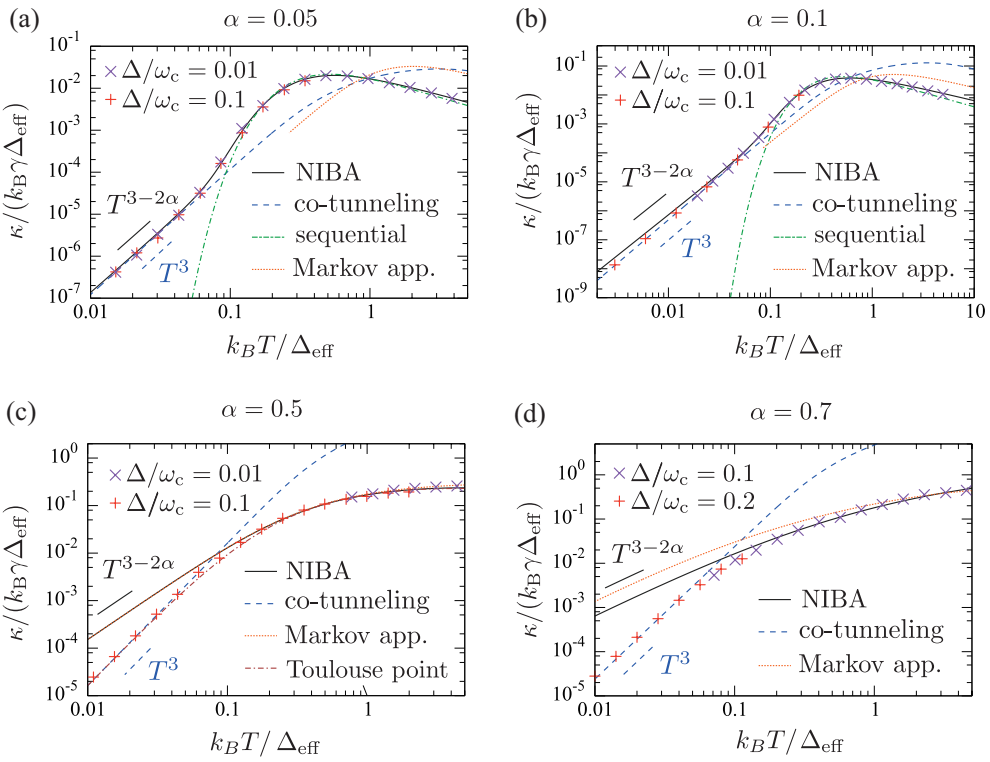

FIGURE 5.1: The temperature dependence of the thermal conductance for (a) $\alpha = 0.05$, (b) 0.1, (c) 0.5, and (d) 0.7. The symbols indicate the numerical results obtained using the CTQMC method. The black solid, green dotted-dashed, blue dashed, and orange dotted lines represent the NIBA, sequential tunneling formula, co-tunneling formula, and Markov approximation for incoherent tunneling, respectively. In (c), the exact solution for the Toulouse point ($\alpha = 0.5$) is indicated by the brown dotted line.

In Fig. 5.1 (a) and (b), we also show the approximate formula for sequential tunneling (indicated by green dotted-dashed lines). As shown in this figure, the sequential tunneling formula at moderate temperatures ($k_BT \sim \Delta_{\rm eff}$) agrees with the numerical results of the weak system-reservoir coupling ($\alpha \ll 1$). This agreement is consistent with the previous study [29]. However, note that the NIBA agrees with the numerical results for a wider temperature region than the sequential tunneling formula.

The Markov approximation for incoherent tunneling, indicated by orange dotted lines in Fig. 5.1, clearly deviates from the numerical results for $\alpha = 0.05$, 0.1, and 0.7, indicating the importance of the non-Markovian properties of the system. The Toulouse point ($\alpha = 0.5$) is an exception, as shown in Figure 5.1 (c); the NIBA coincides with the Markov approximation since at this point the self-energy in the NIBA becomes independent of the frequency for the unbiased case [15]. A detailed discussion on the failure of the Markov approximation is given in Section 5.1.2.

As described in Section 3.1, quantum phase transition occurs at $\alpha_c = 1$ for the Ohmic case. For $\alpha_c \geq 1$, the effective tunneling amplitude $\Delta_{\rm eff}$ becomes zero, indicating complete destruction of the superposition of the two localized states. Therefore, heat transport is induced by incoherent tunneling at arbitrary temperatures. In Fig. 5.2, we show the thermal conductance for $\alpha = 1.0$, 1.5, and 2.0 as a function of temperature. As indicated by the black solid lines in the figure, the numerical results

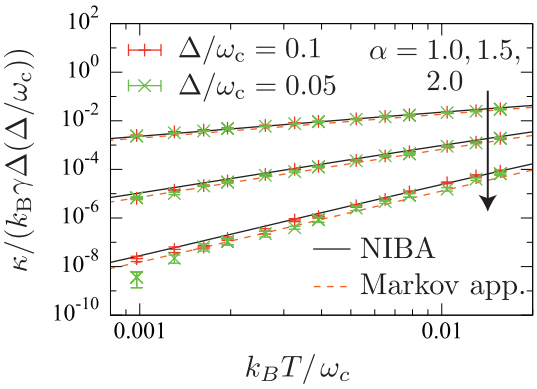

FIGURE 5.2: Temperature dependence of the thermal conductance. The symbols with error bars indicate the numerical results obtained using the CTQMC method for $\alpha = 1.0$, 1.5, and 2.0 from top to bottom. The black solid and orange dashed lines represent the NIBA and the Markov approximation for incoherent tunneling.

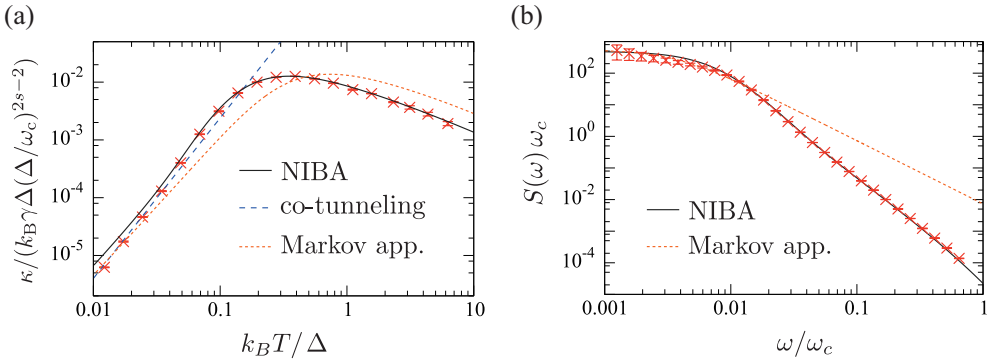

FIGURE 5.3: (a) The thermal conductance calculated using the CTQMC method for $s = 0.9$, $\Delta/\omega_c = 0.01$ and $\alpha = 0.1$. (b) The symmetrized correlation function calculated using the CTQMC method at $k_BT = \omega_c/64$ for parameters same as those considered in (a). The black solid, blue dashed, and orange dotted lines represent the NIBA, co-tunneling formula, and Markov approximation for incoherent tunneling, respectively.

agree well with the NIBA formula for arbitrary temperatures. Note that for $\alpha \geq 1$, the condition for the co-tunneling regime $k_BT \ll \Delta_{\text{eff}}$ is never satisfied. In Fig. 5.2, we also show the Markov approximation for incoherent tunneling (indicated by the orange dashed line). For $\alpha \geq 1$, the difference between the NIBA and the Markov approximation is not considerably large.

5.1.2 The sub-Ohmic case $(0 < s < 1)$

We first discuss the thermal conductance for the sub-Ohmic case wherein the system-reservoir coupling is below the critical value for the quantum phase transition. In Fig. 5.3 (a), we show the thermal conductance as a function of the temperature for $s = 0.9$, $\Delta/\omega_c = 0.01$, and $\alpha = 0.1$, for which the ground state is delocalized ($\alpha < \alpha_c(s, \Delta)$). At moderate and high temperatures, the numerical results agree well

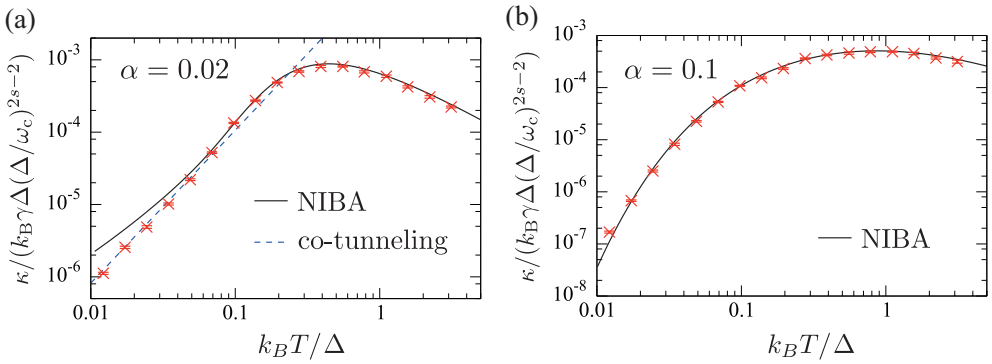

FIGURE 5.4: Temperature behavior of the thermal conductance calculated by a Monte Carlo simulation. The data represent results for $s = 0.6$, $\Delta/\omega_c = 0.01$, (a) $\alpha = 0.02$, and (b) $\alpha = 0.1$. The black solid lines and the blue dashed line represents the NIBA and the co-tunneling formula, respectively.

with the NIBA, which is shown by the black solid line. We note that the sequential-tunneling formula cannot be applied to the sub-Ohmic case. At low temperatures ($k_BT \ll \Delta_{\rm eff}$), the numerical results agree well with the co-tunneling formula, showing T^{2s+1}-dependence.

We also show the results of the Markov approximation for incoherent tunneling by the orange dotted line in Fig. 5.3 (a). The Markov approximation clearly deviates from the numerical results. To understand the failure of the Markov approximation, we show the numerical and analytical result of the symmetrized correlation function $S(\omega)$ as a function of ω/ω_c for $k_BT = \omega_c/64$ in Fig. 5.3 (b). While the Markov approximation for the incoherent tunneling process agrees with the numerical results at a low frequency, clear deviation is observed at higher frequencies; the numerical result indicates that the high-frequency decay of $S(\omega)$ is much faster than that of the Markov approximation, which is proportional to ω^{-2} (see Eq. (3.47)). We note that the numerical result of $S(\omega)$ is well reproduced by the NIBA at arbitrary frequencies. These observations indicate that the non-Markovian properties of the system dynamics are important for obtaining correct thermal conductance results for the sub-Ohmic case.

The quantum phase transition remarkably affects the temperature dependence of the thermal conductance. In Fig. 5.4, we show the thermal conductance as a function of the temperature for $s = 0.6$ and $\Delta/\omega_c = 0.01$, for which a quantum phase transition occurs at $\alpha = \alpha_c = 0.0615$. The detailed procedure for the determination of the critical point is given in Section 4.4. Fig. 5.4 (a) shows the temperature dependence in the delocalized regime ($\alpha = 0.02 < \alpha_c$), for which $\Delta_{\rm eff}$ remains finite. The numerical results agree well with the co-tunneling formula at low temperatures and with the NIBA at moderate-to-high temperatures. This feature is the same as that shown in Fig. 5.3. Fig. 5.4 (b) shows the temperature dependence in the localized regime ($\alpha = 0.1 > \alpha_c$), for which $\Delta_{\rm eff} = 0$. Reflecting the quantum phase transition, the numerical results agree with the NIBA at arbitrary temperatures, as shown in Fig. 5.4 (b). Since the condition for the co-tunneling regime, $k_BT \ll \Delta_{\rm eff}$, is never satisfied for $\Delta_{\rm eff} = 0$, the thermal conductance does not show a universal T^{2s+1}-dependence due to the co-tunneling process at low temperatures.

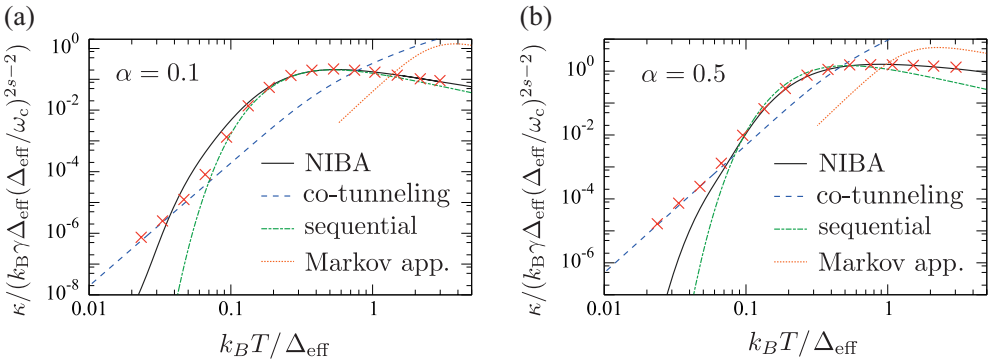

FIGURE 5.5: Temperature behavior of the thermal conductance calculated by Monte Carlo simulation. The data represent results for $s = 1.5$, $\Delta/\omega_c = 0.05$, (a) $\alpha = 0.1$, and (b) $\alpha = 0.5$. In both figures, the black solid, blue dashed, green dotted-dashed, and orange dotted lines represent the NIBA, co-tunneling formula, sequential tunneling formula, and Markov approximation for incoherent tunneling, respectively.

5.1.3 The super-Ohmic case $(1 < s < 2)$

In Fig. 5.5, we show the numerical thermal conductance results obtained using the CTQMC method as a function of temperature for $s = 1.5$. Here, the horizontal and vertical axes are the normalized temperature $k_BT/\Delta_{\rm eff}$ and the normalized thermal conductance $\kappa/(k_B\gamma\Delta_{\rm eff}(\Delta_{\rm eff}/\omega_c)^{2s-2})$, respectively, where $\Delta_{\rm eff}$ is the effective tunneling amplitude defined in Eq. (3.12). Note that there is no quantum transition for the super-Ohmic case ($s > 1$); $\Delta_{\rm eff}$ is finite for arbitrary system-reservoir couplings. At low temperatures ($k_BT \ll \Delta_{\rm eff}$), the numerical results agree with the co-tunneling formula (indicated by blue dashed lines) and show T^{2s+1}-dependence, regardless of the strength of the system-reservoir coupling. As shown in Fig. 5.5 (a), the numerical results for $\alpha = 0.1$ agree with the sequential tunneling formula at moderate temperatures ($k_BT \sim \Delta_{\rm eff}$) and with the NIBA at high temperatures. However, from Fig. 5.5 (b), it is evident that the numerical results for $\alpha = 0.5$ agree better with the NIBA than with the sequential tunneling formula at moderate-to-high temperatures ($k_BT \gtrsim \Delta_{\rm eff}$). This change can be explained by the crossover temperature T^*, which separates the sequential ($T < T^*$) and incoherent ($T > T^*$) tunneling regimes (see Eq. (3.38)). As the system-reservoir coupling α increases, the temperature region for which the numerical results agree with the NIBA is widened since the crossover temperature T^* is lowered.

The Markov approximation for incoherent tunneling is indicated by orange dotted lines in Fig. 5.5. The incoherent tunneling formula clearly deviates from numerical results, indicating the importance of the non-Markovian properties of the system dynamics. The origin of this disagreement is the same as that for the sub-Ohmic case (see Section 5.1.2).

5.1.4 The super-Ohmic case $(2 \leq s)$

In Fig. 5.6, we show the numerical results of the thermal conductance obtained using the CTQMC method as a function of the temperature for $s = 2.0$. The normalization of the horizontal and vertical axes as well as the line types of the analytical formula are same as those in Fig. 5.5. At low temperatures, the numerical results agree

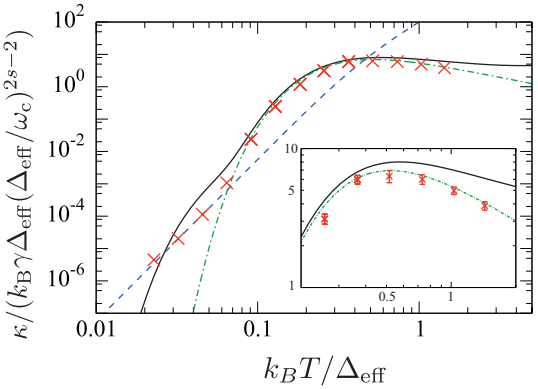

FIGURE 5.6: Temperature dependence of the thermal conductance calculated using CTQMC simulation. The data represent the result for $s = 2.0$, $\Delta/\omega_c = 0.05$, and $\alpha = 0.5$. The linetypes are same as those in Fig. 5.5. The inset shows an enlarged graph in the high-temperature region.

well with the co-tunneling formula and show T^{2s+1}-dependence, regardless of the strength of the system-reservoir coupling. In contrast to the case of $1 < s < 2$, the numerical results agree with the sequential tunneling formula at moderate-to-high temperatures. This is reasonable since the crossover T^* becomes of the order of ω_c for $s = 2.0$.

5.2 Quantum critical phenomena

For the sub-Ohmic case ($0 < s < 1$), a quantum phase transition occurs at zero temperature when the reservoir-system coupling reaches the critical value α_c, where α_c is a function of s and Δ/ω_c as described in Section 3.1. In this section, we discuss quantum critical phenomena near the transition point.

5.2.1 Phase diagram

For $\alpha < \alpha_c$, the ground state is described by a coherent superposition of two wave functions localized at each well (delocalized phase). For $\alpha > \alpha_c$, the ground state becomes two-fold degenerate because the coherent superposition is completely broken owing to the disappearance of quantum tunneling between the two wells (localized phase). The phase diagram of the spin-boson model determined by the CTQMC simulations for $\Delta/\omega_c = 0.1$ is shown in Fig. 5.7 (for details on determining the critical value, α_c, see Section 4.4). The transition separating the two phases is of second-order for the sub-Ohmic case (the empty squares) or of the Kosterlitz-Thouless-type [49, 50] for the Ohmic case (the filled circle). This phase diagram is consistent with previous numerical studies [37, 35].

5.2.2 Thermal conductance

In Fig. 5.8, we show the temperature dependence of the thermal conductance for $s = 0.5$ and $\Delta/\omega_c = 0.1$, where the critical system-reservoir coupling is $\alpha_c = 0.1074$. Figs. 5.8 (a) and (b) show the delocalized-phase side ($\alpha \leq \alpha_c$) and the localized-phase side ($\alpha \geq \alpha_c$), respectively. At the critical point, the thermal conductance exhibits distinctive power-law behavior $\kappa \sim T^c$, where c is the critical exponent, determined

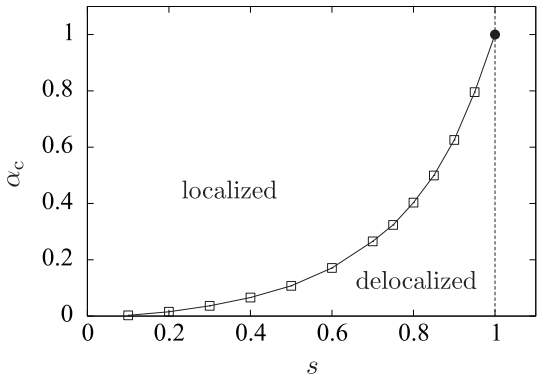

FIGURE 5.7: The phase diagram of the sub-Ohmic case for $\Delta/\omega_c = 0.1$. The solid line indicates the second-order transition line separating the delocalized and localized phases. The empty squares indicate the critical system-reservoir coupling that is numerically determined for the sub-Ohmic case ($0 < s < 1$), whereas the filled circle represents the known transition point $\alpha_c = 1$ for the Ohmic case ($s = 1$).

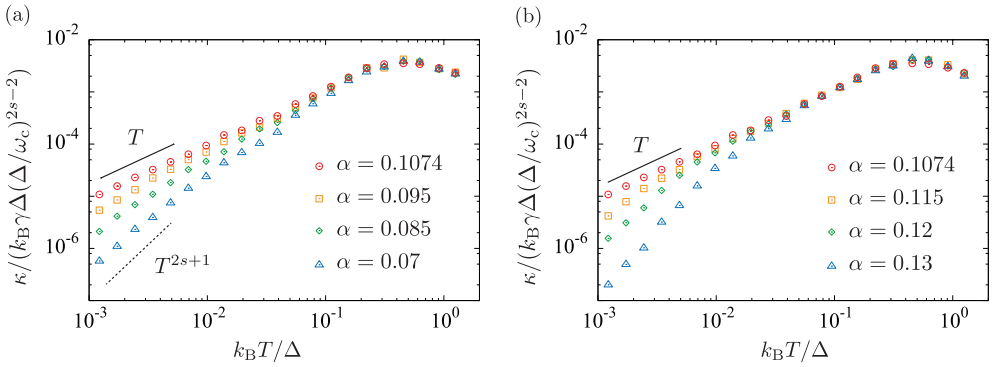

FIGURE 5.8: Temperature dependence of the thermal conductance for (a) $\alpha \leq \alpha_c$ and (b) $\alpha \geq \alpha_c$. The plots represent the CTQMC simulation results for $s = 0.5$ and $\Delta/\omega_c = 0.1$, for which the critical system-reservoir strength is $\alpha_c = 0.1074$.

by the nature of the quantum phase transition in Section 3.6. From Eqs. (3.50) and (3.59), the critical exponent $c = 1$ is obtained for $s = 0.5$. This conclusion is consistent with the critical exponent $c = 1$ obtained by the CTQMC simulation for $s = 0.5$ (see Fig. 5.8).

As the system-reservoir coupling is reduced below the critical value ($\alpha < \alpha_c$), the temperature dependence of the thermal conductance deviates from one at the critical point. For a sufficiently small system-reservoir coupling (e.g., $\alpha = 0.07$ in Fig. 5.8 (a)), the thermal conductance becomes proportional to T^{2s+1} at low temperature, presumably for heat transport due to co-tunneling (3.41). The temperature dependence of the thermal conductance also deviates as the system-reservoir coupling is increased above the critical value ($\alpha > \alpha_c$). Its temperature dependence cannot be explained by a simple formula such as the NIBA up to $\alpha = 0.13$.

Chapter 6

Experimental Realization of Sub-Ohmic Reservoirs

In this chapter, we discuss an experimental realization of sub-Ohmic reservoirs using a superconducting circuit. A previous theoretical study [43] has shown that a spatially-uniform transmission line can realize a sub-Ohmic reservoir with $s = 0.5$. For a controlled experiment of the quantum phase transition, however, it is favorable to realize a sub-Ohmic reservoir with an arbitrary value of s. We propose a superconducting circuit to realize sub-Ohmic reservoirs for arbitrary s by introducing spatial dependence to the circuit elements.

6.1 Superconducting circuit model

In this section, we show that a qubit coupled to two transmission lines reduces to the spin-boson model (see Fig. 6.1 (a)). We consider two kinds of qubits, a flux qubit (Section 6.1.2) and a charge qubit (Section 6.1.3). For simplicity, we first consider uniform LC transmission lines and confirm that the qubits coupled to the transmission lines reduce to the Ohmic spin-boson model. To treat arbitrary transmission lines, we derive general linear-response relations between the spectral density and an impedance of the transmission lines for both types of qubits.

6.1.1 Transmission line

First, we explain that the transmission line, which consists of resistances, inductances, and capacitances (see Fig. 6.1 (b)), is modeled as a set of harmonic oscillators. For simplicity, we consider a uniform transmission line made from constant capacitances C and inductances L without resistances. It is described by the Hamiltonian

$$H = \sum_{j=1}^{N} \frac{Q_j^2}{2C} + \sum_{j=2}^{N} \frac{(\phi_j - \phi_{j-1})^2}{2L}. \tag{6.1}$$

Here we introduced a flux operator $\phi_j(t)$ by $d\phi_j(t)/dt \equiv V_j(t)$, where V_j is a voltage drop at the jth capacitance. The charge operator Q_j is the canonical conjugate variable to the flux operator and these operators satisfy the canonical commutation relation: $[\phi_j, Q_k] = i\delta_{j,k}$. In the continuous limit, $N \to \infty$, the Hamiltonian (6.1) is approximated as follows:

$$H = \int_0^d dx \left[\frac{Q(x)^2}{2c} + \frac{1}{2l} \left(\frac{\partial \phi(x)}{\partial x} \right)^2 \right], \tag{6.2}$$

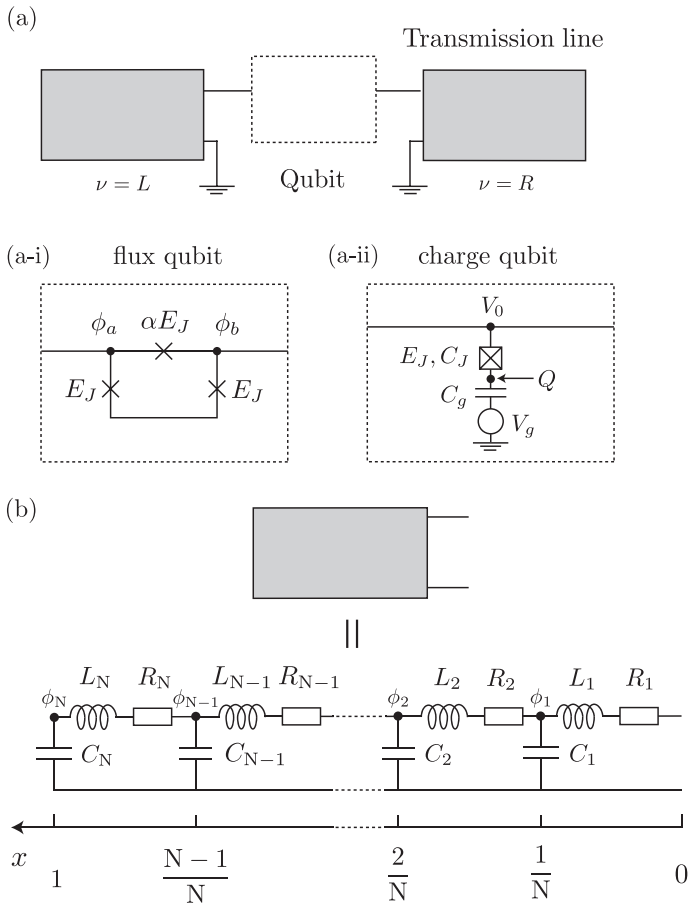

FIGURE 6.1: (a) A superconducting circuit composed of (a-i) flux or (a-ii) charge qubits and two transmission lines. (b) The circuit of the transmission lines proposed to realize the sub-Ohmic spin-boson model, consisting of resistances R_j, inductances L_j, and capacitances C_j.

where d, c, and l are the length of the transmission line, the capacitance and inductance per length, respectively. Expanding $\phi(x)$ in the modes $\{\phi_k\}$

$$\phi(x) = \sum_k \phi_k f_k(x), \tag{6.3}$$

where $f_k(x)$ satisfies

$$\int_0^d dx\, f_k(x) f_{k'}(x) = d\delta_{k,k'}, \quad \int_0^d dx\, \frac{\partial f_k(x)}{\partial x} \frac{\partial f_{k'}(x)}{\partial x} = dk^2 \delta_{k,k'}, \tag{6.4}$$

the Hamiltonian is rewritten follows in terms of ϕ_k and its canonical conjugate variable Q_k as

$$H = \sum_k \left(\frac{1}{2dc} Q_k^2 + \frac{dc\omega_k^2}{2} \phi_k^2 \right), \tag{6.5}$$

where $\omega_k = k/\sqrt{lc}$. Since ϕ_k and Q_k are expressed by $\phi_k = \alpha_k a_k + \alpha_k^* a_k^\dagger$ and $Q_k = \beta_k a_k + \beta_k^* a_k^\dagger$, where a_k ($a_k^\dagger$) is an annihilation (a creation) operator of boson, respectively, the effective Hamiltonian is written as

$$\tilde{H} = \sum_k \left(\frac{|\beta_k|^2}{dc} + \frac{dc\omega_k^2 |\alpha_k|^2}{2} \right) \left(a_k^\dagger a_k + \frac{1}{2} \right) + \sum_k \left[\left(\frac{\beta_k^2}{2dc} + \frac{dc\omega_k^2}{2} \alpha_k^2 \right) a_k^2 + \text{h.c.} \right]. \quad (6.6)$$

Choosing appropriate α_k and β_k under the condition $\alpha_k \beta_k^* - \alpha_k^* \beta_k = i$ from the canonical commutation relation, the effective Hamiltonian (6.6) reduces to a set of the harmonic oscillators with the frequency ω_k.

6.1.2 Flux qubit

We consider a flux qubit coupled to two transmission lines (or two junction arrays), as shown in Fig. 6.1 (a-i). We first consider a uniform transmission line with constant capacitance and inductance ($C_j = C$, $L_j = L$) while neglecting resistance ($R_j = 0$).

The Hamiltonian of the present circuit is given by

$$H = H_{\rm S} + H_{\rm B} + H_{\rm I}, \quad (6.7)$$

$$H_{\rm S} = \sum_{k=1}^{3} \left[\frac{Q_{J,k}^2}{2C_{J,k}} - E_{J,k} \cos(\phi_{J,k}/\phi_0) \right], \quad (6.8)$$

$$H_{\rm B} = \sum_{\nu} \sum_{j=1}^{N} \left[\frac{Q_{\nu,j}^2}{2C} + \frac{(\phi_{\nu,j+1} - \phi_{\nu,j})^2}{2L} \right], \quad (6.9)$$

$$H_{\rm I} = \frac{(\phi_a - \phi_{L,1})^2}{2L_1} + \frac{(\phi_{R,1} - \phi_b)^2}{2L_1}, \quad (6.10)$$

where $H_{\rm S}$, $H_{\rm B}$ ($= \sum_\nu H_{{\rm B},\nu}$), and $H_{\rm I}$ ($= \sum_\nu H_{{\rm I},\nu}$) describe the flux qubit, the transmission lines, and the system-reservoir coupling, respectively, and $\phi_0 = \hbar/2e$ is the flux quantum. The flux qubit comprises three Josephson junctions with Josephson energies $E_{J,k}$ ($k = 1, 2, 3$), and the charge and flux operator of the k-th Josephson junction are denoted by $Q_{J,k}$ and $\phi_{J,k}$, respectively. Similarly, the charge and flux operators of the transmission line (see Fig. 6.1 (b)) are denoted by $Q_{\nu,j}$ and $\phi_{\nu,k}$, respectively. These operators satisfy the exchange relations $[\phi_{J,k}, Q_{J,k'}] = i\delta_{k,k'}$ and $[\phi_{\nu,j}, Q_{\nu',j'}] = i\delta_{j,j'}\delta_{\nu,\nu'}$, respectively. The flux operators at the two sides of the flux qubit are expressed by ϕ_a and ϕ_b (see Fig. 6.1 (a-i)).

To make the flux qubit, the area of one junction is reduced by a factor of α ($E_{J,1} = E_{J,3} = E_J$, $C_{J,1} = C_{J,3} = C_J$, $E_{J,2} = \alpha E_J$, and $C_{J,2} = \alpha^{-1} C_J$). Then, the Hamiltonian of the flux qubit Hamiltonian (6.8) can be rewritten as [17, 32]

$$H_{\rm qb} = \frac{Q_{J,+}^2}{2C_{J,+}} + \frac{Q_{J,-}^2}{2C_{J,-}} + V(\phi_{J,+}, \phi_{J,-}), \quad (6.11)$$

$$V(\phi_{J,+}, \phi_{J,-}) = -E_J \left[2\cos(\phi_{J,+}/2\phi_0) \cos(\phi_{J,-}/2\phi_0) + \alpha \cos\left((\Phi_{\rm ext} - \phi_{J,-})/2\phi_0 \right) \right], \quad (6.12)$$

where $\phi_{J,\pm} = (\phi_{J,1} \pm \phi_{J,3})/2$, its conjugate operator is denoted by $Q_{J,\pm}$, and $V(\phi_{J,+}, \phi_{J,-})$ is the Josephson energy that plays the role of the potential energy. When the magnetic flux through the loop is tuned to be half of the flux quantum ($\Phi_{\rm ext} = \phi_0/2$), the Josephson energy, $V(\phi_{J,+}, \phi_{J,-})$, has two energy minima on the line $\phi_{J,+} = 0$. Due to quantum tunneling effects, there is an energy splitting Δ between the ground

state and the first-excited state. Since these lowest two eigenstates are well separated from the other eigenstates, we can truncate the system into the lowest two eigenstates, thus leading to the two-state system Hamiltonian (6.8). The wavefunctions of the lowest two states are described as $|\sigma_x = \pm 1\rangle = (|\uparrow\rangle \pm |\downarrow\rangle)/\sqrt{2}$, where $|\uparrow\rangle$ and $|\downarrow\rangle$ are the two-dimensional wavefunctions localized at the two potential energy minima, respectively. Introducing the new variables $\phi_\pm = \phi_{R,1} \pm \phi_{L,1}$ and $\Phi_\pm = \phi_b \pm \phi_a$ and using $\phi_{J,+} \propto \Phi_+ \simeq 0$, the system-reservoir coupling (6.10) is rewritten as $H_{\rm I} = -\phi_- \Phi_- / 2L_1$. After truncation into the two-state system, we obtain:

$$H_{\rm I} = -\frac{\phi_-}{2L_1} \phi_0 \langle \varphi_- \rangle \sigma_z, \tag{6.13}$$

where $\langle\uparrow| \Phi_- |\uparrow\rangle \equiv \phi_0 \langle \varphi_- \rangle$, $\langle\downarrow| \Phi_- |\downarrow\rangle \equiv -\phi_0 \langle \varphi_- \rangle$, and $\langle\uparrow| \Phi_- |\downarrow\rangle = \langle\downarrow| \Phi_- |\uparrow\rangle = 0$.

For simplicity, we consider the continuous limit $\Delta x \to 0$ while keeping the length of the transmission line, $d = N\Delta x$, constant, where Δx is the size of each elementary island. Then, the system-reservoir coupling can be rewritten by [17]

$$H_{\rm I} = -\frac{1}{l} \frac{\partial \phi(x)}{\partial x}\bigg|_{x=0} \phi_0 \langle \varphi_- \rangle \sigma_z. \tag{6.14}$$

The transmission line Hamiltonian (6.9) can be The flux, $\phi(x)$, can be expressed by

$$\phi(x) = \sum_k \frac{e^{ikx}}{\sqrt{L_t}} \frac{1}{\sqrt{2c\omega_k}} \left(b_k + b_k^\dagger \right), \tag{6.15}$$

where b_k and $b_k^\dagger$ are bosonic annihilation and creation operators, respectively. Then, the Hamiltonians for the transmission lines and the system-reservoir coupling can be rewritten as follows:

$$H_{\rm B} = \sum_k \omega_k b_k^\dagger b_k, \tag{6.16}$$

$$H_{\rm I} = -\frac{\sigma_z}{2} \sum_k \lambda_k \left(b_k^\dagger + b_k \right), \tag{6.17}$$

$$\lambda_k = \frac{2\phi_0 \langle \varphi_- \rangle}{vl\sqrt{L_t}} \sqrt{\frac{\omega_k}{c}}, \tag{6.18}$$

where $v = 1/\sqrt{lc}$ is the speed of light in the transmission line. This model corresponds to the spin-boson model with an Ohmic reservoir.

Now, we discuss the general linear response relation. The electric current operator at the position x is defined by $\mathcal{I}(x) = l^{-1} \partial\phi(x)/\partial x$ and is calculated at $x = 0$:

$$\mathcal{I}_0 \equiv \mathcal{I}(x = 0) = \sum_k \frac{i\lambda_k}{2\phi_0 \langle \varphi_k \rangle} \left(b_k^\dagger + b_k \right). \tag{6.19}$$

From Eqs. (2.17), (6.17), (6.18), and (6.19), the spectral density is written as

$$I(\omega) = -\frac{4\phi_0^2 \langle \varphi_- \rangle^2}{\pi} \mathrm{Im} \left[G^{\rm R}_{\mathcal{I}_0}(\omega) \right], \tag{6.20}$$

where $G^{\rm R}_{\mathcal{I}_0}(\omega)$ is the Fourier transformation of the current-current correlation function defined by $G^{\rm R}_{\mathcal{I}_0}(t) = -i\theta(t) \langle [\mathcal{I}_0(t), \mathcal{I}_0(0)] \rangle$.

A current $\mathcal{I}_0(\omega)$ is induced by applying an electric field $\boldsymbol{E}(\boldsymbol{r},\omega)$ which can be treated as a perturbation

$$H_{\rm ext}(\omega) = -\frac{i}{\omega}\int d\boldsymbol{r}\, \boldsymbol{i}(\boldsymbol{r})\cdot\boldsymbol{E}(\boldsymbol{r},\omega), \tag{6.21}$$

where $\boldsymbol{i}(\boldsymbol{r},\omega)$ is the current density operator. Using the linear response theory, the current can be expressed as a linear response to the perturbation as follows [64]:

$$\mathcal{I}_0(\omega) = \int d\sigma_r\, \boldsymbol{e}_r\cdot\boldsymbol{i}(\boldsymbol{r},\omega) = \int d\sigma_r d\sigma_{r'} dr'\, \boldsymbol{e}_r\cdot\frac{i}{\omega}G^{\rm R}_{\boldsymbol{i}(\boldsymbol{r})\boldsymbol{i}(\boldsymbol{r}')}(\omega)\boldsymbol{e}_{r'}E(r',\omega), \tag{6.22}$$

where $G^{\rm R}_{\boldsymbol{i}(\boldsymbol{r})\boldsymbol{i}(\boldsymbol{r}')}(t-t') = -i\theta(t-t')\left\langle[\boldsymbol{i}(\boldsymbol{r},t),\boldsymbol{i}(\boldsymbol{r}',t')]\right\rangle$. Note that we have employed a coordinate system (r,σ_r), where r is a coordinate parallel to the electric field, $\boldsymbol{E}(\boldsymbol{r},\omega) = \boldsymbol{e}_r E(r,\omega)$, and σ_r are coordinates on the plane perpendicular to the r-direction. Since the current is not dependent on r due to the current conservation, the linear response can be rewritten by

$$\mathcal{I}_0(\omega) = \int dr'\, \frac{i}{\omega}G^{\rm R}_{\mathcal{I}_0}(\omega)E(r',\omega), \tag{6.23}$$

In addition, the current through a circuit with an impedance $Z(\omega)$ can be also written as

$$\mathcal{I}_0(\omega) = G(\omega)V(\omega) = \int dr\, G(\omega)E(r,\omega). \tag{6.24}$$

Comparing Eq. (6.23) and Eq. (6.24), we obtain the linear response relation between the current-current correlation function and the total impedance of the transmission lines:

$$\frac{1}{Z(\omega)} = \frac{i}{\omega}G^{\rm R}_{\mathcal{I}_0}(\omega). \tag{6.25}$$

Substituting Eq. (6.25) into (6.20), the spectral density can be expressed by the joint impedance of the two transmission lines ($Z_s(\omega) = \sum_\nu Z_\nu(\omega)$) as follows:

$$I(\omega) = \sum_\nu I_\nu(\omega) = \frac{4\phi_0^2\left\langle\varphi_-\right\rangle^2}{\pi}I_0(\omega), \tag{6.26}$$

$$I_0(\omega) = \omega{\rm Re}\left[Z_s(\omega)^{-1}\right]. \tag{6.27}$$

Although we have derived them for a special case, i.e., the case of uniform transmission lines without damping, Eqs. (6.26) and (6.27) hold for arbitrary circuits of the transmission lines because we expect that the coupling form $\mathcal{I}_0\Phi_-$ does not change and the details of the transmission lines are included only in its impedance $Z_\nu(\omega)$.

6.1.3 Charge qubit

We consider a charge qubit coupled to two transmission lines as shown in Fig. 6.1 (a-ii). As in the case of the flux qubit (Section 6.1.2), we first consider a uniform transmission line with constant capacitance and inductance.

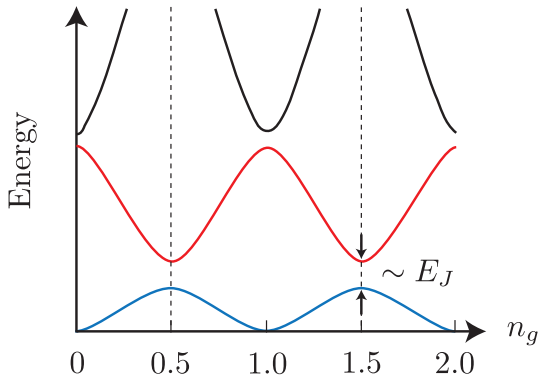

FIGURE 6.2: Eigeneneries of the charge qubit Hamiltonian as a function of the number of the offset charge n_g. At the charge sweet spots (the vertical dashed lines), the two lowest energy states are separated from others and the energy splitting between them is E_J.

The Hamiltonian of the circuit composed of the charge qubit and transmission lines is given by

$$H = H_{\rm S} + H_{\rm B} + H_{\rm I}, \tag{6.28}$$
$$H_{\rm S} = E_C(n - n_g)^2 - E_J\cos(\phi/\phi_0), \tag{6.29}$$
$$H_{\rm I} = \frac{C_J}{C_J + C_g} Q V_0, \tag{6.30}$$

where $H_{\rm S}$ and $H_{\rm I}$ $(= \sum_\nu H_{{\rm I},\nu})$ describe the charge qubit and the system-reservoir coupling, respectively, and $H_{\rm B}$ $(= \sum_\nu H_{{\rm B},\nu})$ is the Hamiltonian of the transmission lines given in Eq. (6.9) (or Eq. (6.16)). The charge qubit comprises a Josephson junction with Josephson energies E_J and the flux drop ϕ, and has the Coulomb energy $E_C = 2e^2/(C_J + C_g)$ and the offset charge $2en_g$. The operator n is the number of Cooper pairs transferred through the Josephson junction ($Q = 2en$). The number operator and flux operator satisfy the exchange relation $[\phi, n] = i\phi_0$. Considering a small Josephson junction with $E_J \ll E_C$ and setting the number of the offset charge as $n_g = 0.5$ (see Fig. 6.2), two lowest charge states $n = 0$ and $n = 1$ are well separated from others, and this system is reduced to the two-state system (2.8) with energy splitting $\Delta \sim E_J$. The wavefunctions of the lowest two states are described as $|\sigma_x = \pm 1\rangle = (|n = 0\rangle \pm |n = 1\rangle)/\sqrt{2}$. After truncation into the two-state system, the system-reservoir coupling Hamiltonian is rewritten as

$$H_{\rm I} = -\frac{\sigma_z}{2}\frac{C_J}{C_J + C_g} 2|e|V_0. \tag{6.31}$$

Considering the continuous limit, the voltage operator V_0 is given by

$$V_0 \equiv \left.\frac{\partial\phi(x = 0, t)}{\partial t}\right|_{t=0}. \tag{6.32}$$

Using the expression of the flux in the transmission line:

$$\begin{aligned}\phi(x=0,t) &= \sum_k \frac{i}{\sqrt{L_t}}\frac{1}{\sqrt{2c\omega_k}}\left(b_k(t)-b_k^\dagger(t)\right)\\ &= \sum_k \frac{i}{\sqrt{L_t}}\frac{1}{\sqrt{2c\omega_k}}\left(b_k e^{-i\omega_k t}-b_k^\dagger e^{i\omega_k t}\right),\end{aligned} \tag{6.33}$$

the voltage operator can be rewritten as

$$V_0 = \sum_k \sqrt{\frac{\omega_k}{2L_t c}}\left(b_k + b_k^\dagger\right). \tag{6.34}$$

Then, the Hamiltonian for the system-reservoir coupling can be rewritten as

$$H_{\rm I} = -\frac{\sigma_z}{2}\sum_k \lambda_k\left(b_k+b_k^\dagger\right), \tag{6.35}$$

$$\lambda_k = \frac{C_J}{C_J+C_g}2|e|\sqrt{\frac{\omega_k}{2L_t c}}. \tag{6.36}$$

This model corresponds to the Ohmic spin-boson model.

Now, we consider the voltage-voltage correlation function defined by $G^{\rm R}_{V_0}(t) = -i\theta(t)\langle[V_0(t),V_0(0)]\rangle$ and obtain the relation between the spectral density and the impedance of the transmission lines in the same way as the flux qubit case. From Eq. (6.34), the Fourier transformation of the voltage-voltage correlation function is related with the spectral density as follows:

$$I(\omega) = -\frac{4|e|^2}{\pi}\left(\frac{C_J}{C_J+C_g}\right)^2 {\rm Im}\left[G^{\rm R}_{V_0}(\omega)\right]. \tag{6.37}$$

Using the linear response relation (6.25) and $G^{\rm R}_{V_0}(\omega) = Z(\omega)^2 G^{\rm R}_{\mathcal{I}_0}(\omega)$, we obtain the spectral density in terms of the impedance

$$I(\omega) = \sum_\nu I_\nu(\omega) = \frac{4|e|^2}{\pi}\left(\frac{C_J}{C_J+C_g}\right)^2 I_0(\omega), \tag{6.38}$$

$$I_0(\omega) = \omega {\rm Re}\left[Z_p(\omega)\right], \tag{6.39}$$

where $Z_p(\omega)^{-1} = \sum_\nu Z_\nu(\omega)^{-1}$.

6.2 The spectral densities

To realize a sub-Ohmic reservoir with an arbitrary exponent, s, we propose a superconducting circuit, as shown in Fig. 6.1 (b). The circuit comprises resistances R_j, inductances L_j, and capacitances C_j ($j = 1, 2, \cdots, N$). For simplicity, we assume that the two transmission lines are constructed by the same circuit. The joint impedance of the two transmission lines is then calculated as $Z_s(\omega) = 2Z_1(\omega)$ for the case of the flux qubit and $Z_p(\omega)^{-1} = 2Z_1(\omega)^{-1}$ for the case of the charge qubit, where $Z_j(\omega)$ ($j = 1, 2, \cdots, N$) includes from jth to Nth islands and is given by a recurrence relation:

$$Z_j(\omega) = R_j + i\omega L_j + \frac{1}{Z_{j+1}(\omega)^{-1}+i\omega C_j}, \tag{6.40}$$

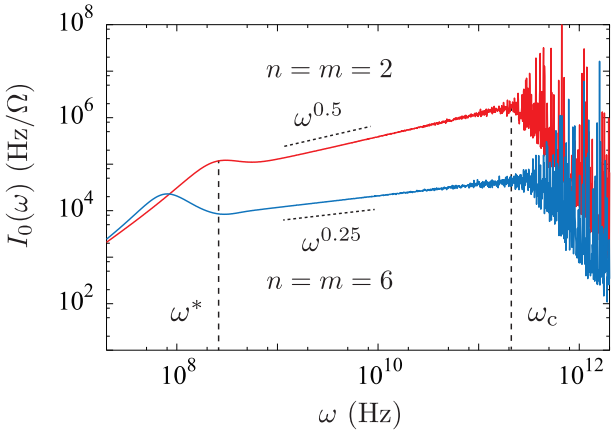

FIGURE 6.3: The spectral density of the superconducting circuit for $s = 0.5$ and 0.25, corresponding to $(n, p, m) = (2, 0, 2)$ and $(6, 0, 6)$. The circuit parameters are set to $N = 10^4$, $R_0 = 1$ kΩ, $L_0 = 13$ nH, and $C_0 = 1$ pF. Each circuit element has 1% relative randomness.

with $Z_{N+1}(\omega)^{-1} = 0$. In the following, we assume that circuit elements have spatial dependence:

$$R_j = R_0 \left(\frac{j}{N}\right)^n, \quad L_j = L_0 \left(\frac{j}{N}\right)^p, \quad C_j = C_0 \left(\frac{j}{N}\right)^m. \tag{6.41}$$

where n, p, and m are non-negative real numbers.

6.2.1 Flux qubit

We assume that the exponents of the circuit elements (see Eq. (6.41)) are set as

$$n \geq 0, \quad p = 0, \quad m \geq 0. \tag{6.42}$$

We show the spectral density, $I_0(\omega) = \omega \mathrm{Re}[Z_s(\omega)^{-1}]$ (see Eq. (6.27)), of the superconducting circuit in Fig. 6.3 for $(n, p, m) = (2, 0, 2)$ and $(6, 0, 6)$. The parameters are set to $R_0 = 1$ kΩ, $L_0 = 13$ nH, $C_0 = 1$ pF, and $N = 10^4$ and referred to experimental studies on Josephson junction arrays [65]. In Fig. 6.3, we added 1% relative randomness for each circuit element to introduce tolerance to circuit parameter fluctuations.

We determined that the spectral density is approximately proportional to ω^s in a certain range of the frequency with the exponent $0 < s < 1$. This indicates that the present circuit can realize a sub-Ohmic reservoir with an arbitrary value of s. Certainly, the analytical calculation concludes:

$$I(\omega) \propto \omega^{2/(m+2)}, \quad (\omega^* \ll \omega \ll \omega_c). \tag{6.43}$$

The detailed calculation is given in Appendix D.1. This result is in good agreement with Fig. 6.3; $m = 2$ and 6 correspond to $s = 0.5$ and 0.25, respectively. The lower frequency limit for the sub-Ohmic spectral density, ω^*, is calculated as follows:

$$\omega^* = \left[\left(\frac{m}{2N}\right)^{2n} \frac{R_0^{m+2}}{C_0^n L_0^{m+n+2}}\right]^{1/(m+2n+2)}. \tag{6.44}$$

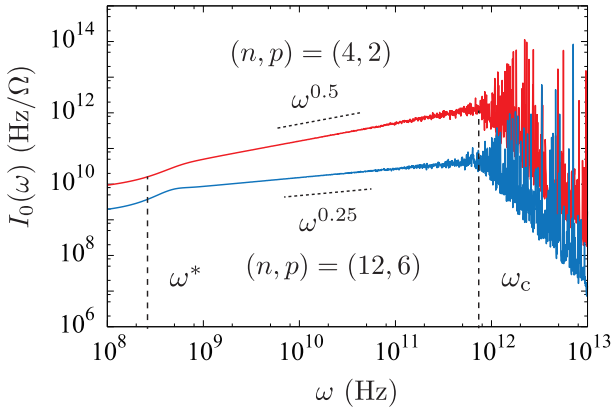

FIGURE 6.4: The spectral density of the superconducting circuit for $s = 0.5$ and $s = 0.25$, corresponding to $(n, p, m) = (4, 2, 0)$ and $(12, 6, 0)$. The circuit parameters are set to $N = 10^4$, $R_0 = 0.1$ kΩ, $L_0 = 13$ nH, and $C_0 = 0.01$ pF. Each circuit element has 1% relative randomness.

Therefore, the exponent n for the resistance (see Eq. (6.41)) controls the lower limit of the sub-Ohmic spectral density. In contrast, the higher frequency limit, ω_c, is a complex function of the circuit parameters.

6.2.2 Charge qubit

We set the exponents of the circuit elements as

$$n \geq p \geq 0, \quad m = 0. \tag{6.45}$$

In Fig. 6.4, we show the spectral density, $I_0(\omega) = \omega \mathrm{Re}[Z_p(\omega)]$ (see Eq. (6.39)), of the superconducting circuit for $(n, p, m) = (4, 2, 0)$ and $(12, 6, 0)$ with $R_0 = 0.1$ kΩ, $L_0 = 13$ nH, $C_0 = 0.01$ pF, and $N = 10^4$, and added 1% relative randomness for each circuit element to introduce tolerance to circuit parameter fluctuations.

From Fig. 6.4, the transmission line realizes a sub-Ohmic reservoir with arbitrary exponent $0 < s < 1$ in a certain range of the frequency. Calculating the transmission line with spatial dependent elements (6.45) analytically (for detail, see Appendix D.2), we obtain the frequency dependence as

$$I(\omega) \propto \omega^{2/(p+2)}, \quad (\omega^* \ll \omega \ll \omega_c). \tag{6.46}$$

This analytical result is consistent with Fig. 6.4; $p = 2$ and 6 correspond to $s = 0.5$ and 0.25, respectively. The lower frequency limit, ω^*, is calculated as follows:

$$\omega^* = \left[\left(\frac{p}{2N} \right)^{2(n-p)} \frac{R_0^{p+2}}{C_0^{n-p} L_0^{n+2}} \right]^{1/(2n-p+2)}. \tag{6.47}$$

The lower frequency limit is controlled by the exponent n for the resistance. As in the case of the flux qubit, the higher frequency limit, ω_c, is a complex function of the circuit parameters.

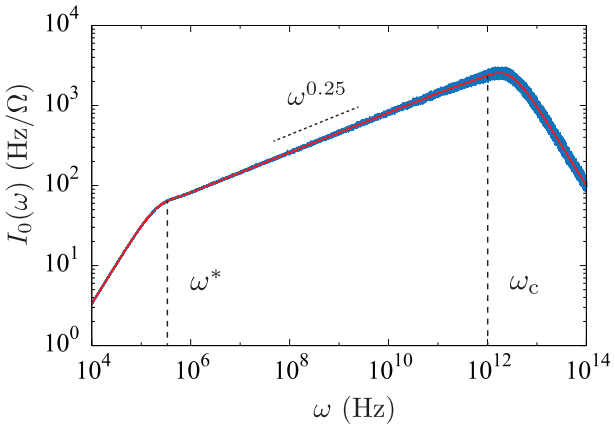

FIGURE 6.5: The spectral density function of the superconducting circuit for $s = 0.25$ corresponding to (n, p, m) = (2, 0, 0). The circuit parameters are set as $N = 10^2$, $R_0 = 0.1$ mΩ, and $C_0 = 0.1$ mF. The red and blue lines represent cases that each circuit element has 0% and 10% relative randomnesses, respectively.

6.2.3 Charge qubit $(0 < s \leq 0.5)$

There is another way to realize a sub-Ohmic reservoir with the restricted exponent $0 < s \leq 0.5$ using the charge qubit. To realize the transmission line, we set the exponent of circuit elements as

$$n \geq 0, \quad p = 0, \quad m = 0. \tag{6.48}$$

In Fig. 6.5, we show the spectral density, $I_0(\omega)$, of the transmission line for (n, p, m) = (2, 0, 0) with 0% and 10% relative randomness for each circuit element. The parameters are set to $N = 10^2$, $R_0 = 0.1$ mΩ, and $C_0 = 0.1$ mF.

As shown in Fig. 6.5, the present circuit realizes the sub-Ohmic reservoir in a certain range of the frequency. Compared with the above two cases (Sections 6.2.1 and 6.2.2), the present circuit (6.48) can realize a sub-Ohmic reservoir with a smaller number of islands, N, and has a higher tolerance for randomness. By the analytical calculation in Appendix D.3, we obtain the frequency dependence of the spectral density:

$$I(\omega) \propto \omega^{1/(n+2)}, \quad (\omega^* \ll \omega \ll \omega_c). \tag{6.49}$$

This result is in good agreement with Fig. 6.5; $n = 2$ corresponds to 0.25. However, from analytical calculation (6.49), the exponent of the spectral density is restricted to $0 < s \leq 0.5$. In this case, the lower frequency limit, ω^*, and the higher frequency limit, ω_c, can be calculated as follows:

$$\omega^* = \frac{1}{R_0 C_0}\left(\frac{n}{2N}\right)^2\left(1+\frac{2\sqrt{2}}{n}\right)^{n+2}, \tag{6.50}$$

$$\omega_c = \frac{1}{R_0 C_0}\left(\frac{2N}{n}\right)^n. \tag{6.51}$$

Chapter 7

Summary

We systematically studied heat transport via a local two-state system for all types of reservoirs, i.e., for the Ohmic case ($s = 1$), sub-Ohmic case ($s < 1$), and super-Ohmic case ($s > 1$) near equilibrium. We used the exact expression for the thermal conductance obtained from the Keldysh formalism and studied it using both analytical and numerical methods within the linear response.

We showed that heat transport via a two-state system can be described by three types of transport processes: sequential tunneling, co-tunneling, and incoherent tunneling. Sequential tunneling is a transport process occurred by a combination of photon (or phonon) absorption and emission, and the temperature dependence of the thermal conductance is the exponential decrease as the temperature is lowered. Co-tunneling is a transport process via a virtual excitation in the local two-state system, and the thermal conductance behaves as $\kappa \propto T^{2s+1}$ at low temperatures. Incoherent tunneling is a transport process induced by a stochastic transition between two localized wavefunctions. In this thesis, we gave the condition for the sequential tunneling using the quantum master equation and showed that the sub-Ohmic case does not satisfy this condition. We also pointed out that the Markov approximation yielded incorrect results for the thermal conductance in the incoherent tunneling regime since the non-Markovian properties are important. However, for the incoherent tunneling regime, the NIBA yielded correct results.

We used a continuous-time Monte Carlo algorithm and systematically compared the numerical results with those of the analytical approximation formulas. We found that all numerical results were well reproduced by one of three formulas, i.e., the sequential tunneling formula, co-tunneling formula, or NIBA. We summarize the relevant transport mechanisms for each regime in Table 7.1. We also showed that for $0 < s \leq 1$, the quantum phase transition between the delocalized and localized phases strongly affected the temperature dependence of the thermal conductance. For the delocalized phase ($\alpha < \alpha_c$), the thermal conductance is well described by the co-tunneling formula at low temperatures and by NIBA at moderate-to-high temperatures. On the contrary, for the localized phase ($\alpha \gg \alpha_c$), the NIBA holds arbitrary temperatures.

Furthermore, we studied quantum critical phenomena (QCP) in the sub-Ohmic case from the viewpoint of heat transport. By the continuous-time quantum Monte Carlo simulations, we showed that the thermal conductance at the critical point ($\alpha = \alpha_c$) has a characteristic power-law temperature dependence determined by the nature of the quantum phase transition. We also clarified the means by which the critical exponent of the thermal conductance is related to other critical exponents discussed in previous theoretical studies.

Finally, we proposed a superconducting circuit with the flux or charge qubits that realize the sub-Ohmic spin-boson model. Giving the spatial dependence to circuit elements in transmission lines (or Josephson junction arrays), the sub-Ohmic spectral

TABLE 7.1: Summary of the relevant transport process. The last column shows the temperature dependences of the thermal conductance. The temperature dependence of the NIBA is complex in general, and the symbol $(^*)$ indicates the high-temperature limit. Near the quantum critical point for the sub-Ohmic case, the thermal conductance shows a quantum critical phenomena (QCP). The critical exponent c is a function of s (see Eq. (3.59)).

Exponent	Condition	Transport Process	Dependence
$0 < s < 1$	$\alpha < \alpha_c$, $k_B T \ll \Delta_{\rm eff}$	Co-tunneling	T^{2s+1}
(sub-Ohmic)	$\alpha < \alpha_c$, $k_B T \gtrsim \Delta_{\rm eff}$	Incoherent tun.	
	$\alpha > \alpha_c$, arbitrary temp.	Incoherent tun.	
	$\alpha = \alpha_c$, $k_B T \ll \Delta_{\rm eff}$	QCP	T^c
$s = 1$	$\alpha < 1$, $k_B T \ll \Delta_{\rm eff}$	Co-tunneling	T^3
(Ohmic)	$\alpha < 1$, $k_B T \gtrsim \Delta_{\rm eff}$	Incoherent tun.	$T^{2\alpha-1}$ $(^*)$
	$\alpha > 1$, arbitrary temp.	Incoherent tun.	$T^{2\alpha-1}$ $(^*)$
$1 < s < 2$	$k_B T \ll \Delta_{\rm eff}$	Co-tunneling	T^{2s+1}
(super-Ohmic)	$\Delta_{\rm eff} \lesssim k_B T \lesssim k_B T^*$	Sequential tun.	$e^{-\Delta_{\rm eff}/k_B T}/T^2$
	$k_B T > k_B T^*$	Incoherent tun.	
$2 \leq s$	$k_B T \ll \Delta_{\rm eff}$	Co-tunneling	T^{2s+1}
(super-Ohmic)	$k_B T \gtrsim \Delta_{\rm eff}$	Sequential tun.	$e^{-\Delta_{\rm eff}/k_B T}/T^2$

density with an arbitrary value of the exponent s is realized in a certain frequency range.

The present study provides a theoretical basis for describing heat transport via nano-scale objects. The present study also provides a new platform for experiments attempting to access quantum phase transitions directly upon measuring heat transport in mesoscopic devices.

Appendix A

Instanton Method

In this appendix, we derive the tunneling amplitude for the double-well potential systems, Eq. (2.7), using an instanton method. In the imaginary-time path-integral formalism, the transition amplitude from $q(-\tau_0/2) = q_i$ to $q(\tau_0/2) = q_f$ is written as

$$\langle q_f | \, e^{-H_S \tau_0} \, | q_i \rangle = N \int \mathcal{D}q(\tau) \, e^{-S^{(\mathrm{E})}[q(\tau)]}, \tag{A.1}$$

where $S^{(E)}[q(\tau)]$ is the Euclidean action:

$$S^{(\mathrm{E})}[q(\tau)] = \int_{-\tau_0/2}^{+\tau_0/2} d\tau \, \left\{ \frac{M}{2} \left[\frac{q(\tau)}{d\tau} \right]^2 + V[q(\tau)] \right\}, \tag{A.2}$$

where N is a normalization factor, and $\int \mathcal{D}q(\tau)$ denotes integration over all path $q(\tau)$. Now suppose the semi-classical approximation, in which the action takes large values than the Plank constant (note that $\hbar$ is set as unity in this thesis). In this situation, the integral (A.1) is dominantly determined by the stationary solution and fluctuation of the paths around it. The stationary solution $X(\tau)$ is obtained from the stationary condition $\delta S^{(E)}[X(\tau)] = 0$ as

$$-M \frac{d^2 X(\tau)}{d\tau^2} + \frac{dV[X(\tau)]}{dX(\tau)} = 0. \tag{A.3}$$

This equation corresponds to the classical equation of motion of particle under the upside-down potential, $-V(q)$. If there is one stationary point, we can estimate the exponential factor of the transition amplitude as follows:

$$\langle q_f | \, e^{-H_S \tau_0} \, | q_i \rangle = N \int \mathcal{D}q(\tau) \, e^{-S^{(\mathrm{E})}[q(\tau)]} \sim e^{-S_0^{(\mathrm{E})}}, \tag{A.4}$$

where $S_0^{(\mathrm{E})} = S^{(\mathrm{E})}[X(\tau)]$ is the action of the stationary solution.

Next, we consider the pre-exponential factor of the transition amplitude. The path $q(\tau)$ of the integral in Eq. (A.1) is expanded around the stationary solution as

$$q(\tau) = X(\tau) + \sum_n c_n x_n(\tau), \tag{A.5}$$

where $x_n(\tau)$ is a complete set of orthonormal functions that vanish at the boundary:

$$\int_{-\tau_0/2}^{+\tau_0/2} d\tau \, x_n(\tau) x_m(\tau) = \delta_{m,n}, \; x_n(\pm\tau_0/2) = 0. \tag{A.6}$$

Thus, the integral measure can be written in the form

$$\int \mathcal{D}q(\tau) = \prod_n \int \frac{dc_n}{\sqrt{2\pi}}. \tag{A.7}$$

Expanding the Euclidean action up to the second order around the stationary point

$$\begin{aligned} & S^{(\mathrm{E})}\left[X(\tau) + \sum_n c_n x_n(\tau)\right] - S_0^{(\mathrm{E})}[X(\tau)] \\ &= \int_{-\tau_0/2}^{+\tau_0/2} d\tau \left(\sum_n c_n x_n(\tau)\right)\left[-\frac{M}{2}\frac{d^2}{d\tau^2} + \frac{1}{2}\frac{d^2V[X(\tau)]}{dX(\tau)^2}\right]\left(\sum_n c_n x_n(\tau)\right). \end{aligned} \tag{A.8}$$

We note that the first-order terms with respect to $x_n(\tau)$ vanish as $X(\tau)$ is the stationary solution. Here, we assume that $\{x_n(\tau)\}$ are eigenfunctions of the differential operator $-Md^2/d\tau^2 + V''[X(\tau)]$:

$$\left[-M\frac{d^2}{d\tau^2} + \frac{d^2V[X(\tau)]}{dX(\tau)^2}\right] x_n(\tau) = \epsilon_n x_n(\tau), \tag{A.9}$$

where $\{\epsilon_n\}$ is the corresponding eigenvalues. Then, the Euclidean action is transformed into the diagonal form

$$S^{(\mathrm{E})}\left[X(\tau) + \sum_n c_n x_n(\tau)\right] = S_0^{(\mathrm{E})} + \frac{1}{2}\sum_n \epsilon_n c_n^2. \tag{A.10}$$

Performing Gaussian integration, we obtain the transition amplitude

$$\langle q_f | \, e^{-H_S \tau_0} \, | q_i \rangle = e^{-S_0^{(\mathrm{E})}} N \prod_n \epsilon_n^{-1/2} \tag{A.11}$$

$$= e^{-S_0^{(\mathrm{E})}} N \left\{ \det\left[-M\frac{d^2}{d\tau^2} + \frac{d^2V[X(\tau)]}{dX(\tau)^2}\right]\right\}^{-1/2}. \tag{A.12}$$

In the following, we calculate the exponential and pre-exponential factors concretely in the double-well potential (2.5).

A.1 Exponential factor

Let us first consider the stationary solution for the double-well potential system. The classical equation of motion (A.3) has not only trivial solutions

$$X(\tau) = \pm\frac{q_0}{2}, \tag{A.13}$$

but also nontrivial solutions which connect the points $\pm q_0/2$. These nontrivial solutions are crucial to calculate the quantum tunneling amplitude. In the limit $\tau_0 \to \infty$, these nontrivial solutions of Eq. (A.3) are

$$X_\pm(\tau) = \pm\frac{q_0}{2}\tanh\left[\frac{\omega_0(\tau - \tau_c)}{2}\right], \tag{A.14}$$

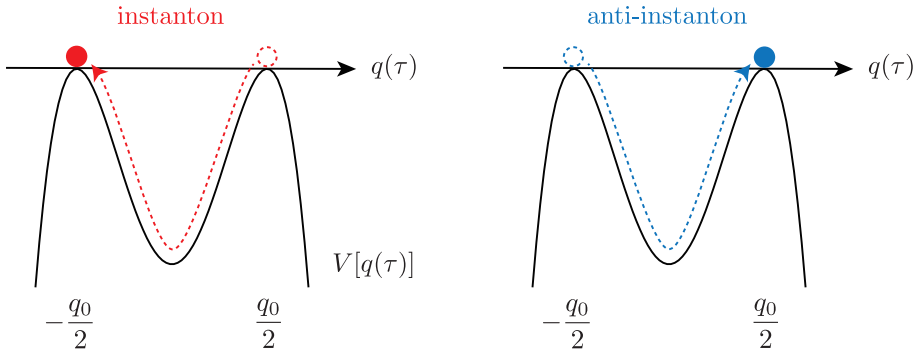

FIGURE A.1: Schematic of the instanton and anti-instanton. The instanton is the imaginary time path from the point $-q_0/2$ to $+q_0/2$ in the upside-down potential $V[q(\tau)] = -V[q(t)]$. The anti-instanton is the imaginary time path opposite to the instanton.

where τ_c is the arbitrary parameter. These solutions, $X_+(\tau)$ and $X_-(\tau)$, are called 'instanton' and 'anti-instanton', respectively (see Fig. A.1). Using the instanton or anti-instanton solutions, we obtain the action $S_0^{(E)}$

$$S_0^{(E)} = S^{(E)}[X_\pm(\tau)] = \frac{16V_b}{3\omega_0}. \tag{A.15}$$

This exponential factor is consistent with one derived from the WKB approximation [66]. Note that τ_c may take an arbitrary time, and the action of the instanton, $S_0^{(E)}$, does not depend on the τ_c, reflecting the invariance with respect to time translation. Each concrete solution (A.14) has a definite position with respect to the origin, and thus there exits an infinite family of solutions distributed along the imaginary-time axis.

A.2 Pre-exponential factor

First, we consider the single-instanton contribution to the transition amplitude, Eq. (A.1), and calculate the pre-exponential factor of it. The transition amplitude (A.12) is rewritten as

$$\begin{aligned}\langle \pm q_0/2 | \, e^{-H_S \tau_0} \, | \mp q_0/2 \rangle_{\text{single}} &= N e^{-S_0^{(E)}} \left[\det\left(-M\frac{d^2}{d\tau^2} + \omega_0^2 \right) \right]^{-1/2} \\ &\quad \times \left\{ \frac{\det\left[-Md^2/d\tau^2 + V''[X(\tau)] \right]}{\det\left(-Md^2/d\tau^2 + \omega_0^2 \right)} \right\}^{-1/2}\end{aligned} \tag{A.16}$$

We multiplied and divided by the determinant for harmonic oscillator, which is calculate easily as [66]

$$N \left[\det\left(-M\frac{d^2}{d\tau^2} + \omega_0^2 \right) \right]^{-1/2} = \sqrt{\frac{M\omega_0}{2\pi \sinh(\omega_0 \tau_0)}} \tag{A.17}$$

$$\sim \sqrt{\frac{M\omega_0}{\pi}} e^{-\omega_0 \tau_0/2}, \ \tau_0 \to \infty. \tag{A.18}$$

Substituting the explicit expression $X_+(\tau)$ (A.14) into $V''[X(\tau)]$, we obtain the eigenvalue equation for determinant in the numerator:

$$\left\{-\frac{d^2}{d\tau^2}+\omega_0^2\left[1-\frac{3}{2}\frac{1}{\cosh^2(\omega_0(\tau-\tau_c)/2)}\right]\right\}x_n(\tau)=\epsilon x_n(\tau) \tag{A.19}$$

It can be regarded as a certain Schorödinger equation. Under the boundary condition $x_n(\pm\tau_0/2)=0$, $\tau_0\to\infty$, Eq. (A.19) has discrete spectrum for $\epsilon<\omega_0$ and continuous spectrum for $\epsilon>\omega_0$ [67]. There are two discrete levels; one has the eigenvalue $\epsilon_1=(3/4)\omega_0^2$, and the other $\epsilon_0=0$. The eigenfunction of the latter is [67]

$$x_0(\tau)=\sqrt{\frac{3\omega_0}{8}}\frac{1}{\cosh^2(\omega_0(\tau-\tau_c)/2)}. \tag{A.20}$$

The naive integration with respect to the coefficient c_0 (A.7) (the zero mode) gives divergence since the action is independent of c_0. However, we can overcome this divergence by changing the integration over c_0 into τ_c. Note that the eigenfunction $x_0(\tau)$ is proportional to $dX(\tau)/d\tau$. This means that the change of c_0 can be absorbed into the translational shift of the instanton solution along the imaginary-time axis. When c_0 is changed into $c_0+\Delta c_0$, the change of the path, $\Delta q(\tau)$, is given as $\Delta q(\tau)=x_0(\tau)\Delta c_0$ (see Eq. (A.5)). On the other hand, the change $\Delta q(\tau)$ under a shift $\Delta\tau_c$ is

$$\Delta q(\tau)=\Delta X(\tau)=\frac{dq}{d\tau_c}\Delta\tau_c=-\sqrt{S_0^{(E)}}x_0(\tau)\Delta\tau_c. \tag{A.21}$$

Comparing the two increments, we obtain

$$dc_0=\sqrt{S_0^{(E)}}d\tau_c. \tag{A.22}$$

Then, considering separately the zero mode in the ratio of the determinant,

$$\begin{aligned}&\left\{\frac{\det\left[-Md^2/d\tau^2+V''[X(\tau)]\right]}{\det\left(-Md^2/d\tau^2+\omega_0^2\right)}\right\}^{-1/2}\\&=\sqrt{\frac{S_0^{(E)}}{2\pi}}\omega_0 d\tau_c\left\{\frac{\det'\left[-Md^2/d\tau^2+V''[X(\tau)]\right]}{\det'\left(-Md^2/d\tau^2+\omega_0^2\right)}\right\}^{-1/2}\\&=\sqrt{\frac{S_0^{(E)}}{2\pi}}\omega_0 d\tau_c\left\{\frac{\det'\left[-Md^2/d\tau^2+V''[X(\tau)]\right]}{\omega_0^{-2}\det\left(-Md^2/d\tau^2+\omega_0^2\right)}\right\}^{-1/2},\end{aligned} \tag{A.23}$$

where $\det'[\cdots]$ denoted the reduced determinant with the zero mode removed.

We now consider the non-zero modes. It is easiest to deal with the second discrete level, whose eigenvalue is $(3/4)\omega_0^2$. If we denote by Φ the ratio

$$\Phi=\frac{\det'\left[-Md^2/d\tau^2+V''[X(\tau)]\right]}{\omega_0^{-2}\det\left(-Md^2/d\tau^2+\omega_0^2\right)}, \tag{A.24}$$

the contribution of this level to Φ as $\tau_0\to\infty$ is $3/4$. We turn to other modes, with $\epsilon>\omega_0^2$. In this region, Eq (A.19) has a continuous spectrum without the boundary condition. Therefore, let us forget the boundary condition for a moment. The

solution in the continuous spectrum has the following properties: First, the solutions are labeled by a continuous index p, which is related to the eigenvalue ϵ by $p = \sqrt{\epsilon_p - \omega_0^2}$ and ranges over the entire interval $(0, \infty)$. Second, the continuum wavefunctions determined by the Schrödinger equation, Eq. (A.19), include no reflection. Namely, choosing one of the linearly independent solutions in such a way that

$$x_p(\tau) = e^{ip\tau}, \quad \tau \to +\infty, \tag{A.25}$$

we have in the other asymptotic region the same exponential:

$$x_p(\tau) = e^{ip\tau + i\delta_p}, \quad \tau \to -\infty. \tag{A.26}$$

The entire dynamical effect is reduced to the phase [67]

$$e^{i\delta_p} = \frac{1 + ip/\omega_0}{1 - ip/\omega_0} \frac{1 + 2ip/\omega_0}{1 - 2ip/\omega_0}. \tag{A.27}$$

Since the second linearly independent solution can be chosen in the form $x_p(-\tau)$, the general solution is $Ax_p(\tau) + Bx_p(-\tau)$, where A and B are arbitrary constants. Considering the boundary condition $x(\pm\tau_0/2) = 0$, the arbitrary constants satisfy

$$Ax_p(\pm\tau_0/2) + Bx_p(\mp\tau_0/2) = 0. \tag{A.28}$$

In order to have nontrivial solutions for Eq. (A.28), it is necessary to satisfy

$$\frac{x_p(\tau_0/2)}{x_p(-\tau_0/2)} = \pm 1, \tag{A.29}$$

which gives the equation for p:

$$p\tau_0 - \delta_p = \pi n, \quad n = 0,\ 1, \ldots. \tag{A.30}$$

If we denote the solutions of Eq. (A.30) by $\tilde{p}_n = p_n + \delta_p/\tau_0$ where $p_n = \pi n/\tau_0$, the ratio Φ of the determinant in $\epsilon > \omega_0$ is written as

$$\Phi_{\text{con.}} \simeq \prod_{n=0}^{\infty} \frac{\omega_0^2 + \tilde{p}_n^2}{\omega_0^2 + p_n^2}. \tag{A.31}$$

Since the difference $\tilde{p}_n - p_n$ is small in the limit $\tau_0 \to \infty$, $\Phi_{\text{con.}}$ can be written as

$$\Phi_{\text{con.}} = \exp\left[\sum_{n=0}^{\infty} \ln \frac{\omega_0^2 + p_n^2}{\omega_0^2 + p_n^2}\right] \approx \exp\left[\sum_{n=0}^{\infty} \frac{2p_n(\tilde{p}_n - p_n)}{\omega_0^2 + p_n^2}\right]. \tag{A.32}$$

Changing from the summation over n into integration over p_n and using Eq. (A.30), we obtain

$$\begin{aligned} \Phi_{\text{con.}} &= \exp\left[\frac{1}{\pi}\int_0^{\infty} dp\, \frac{2\delta_p p}{p^2 + \omega_0^2}\right] = \exp\left[-\frac{1}{\pi}\int_0^{\infty} \frac{d\delta_p}{dp} \ln\left(1 + \frac{p^2}{\omega_0^2}\right) dp\right] \\ &= \exp\left[-\frac{2}{\pi}\int_0^{\infty} dy\, \left(\frac{1}{1+y^2} + \frac{2}{1+4y^2}\right) \ln\left(1+y^2\right)\right] = \frac{1}{9}. \end{aligned} \tag{A.33}$$

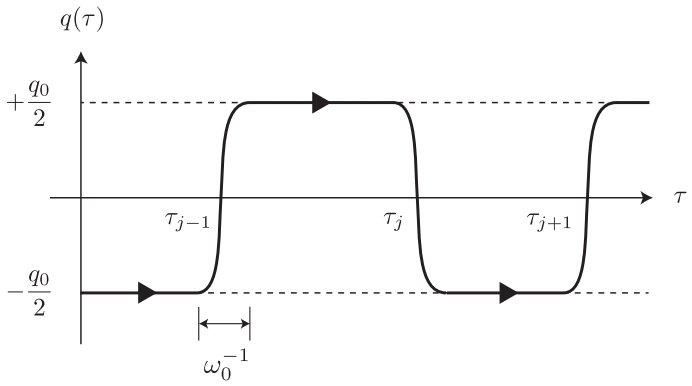

FIGURE A.2: Dilute instanton gas configuration.

Here, we introduced the dimensionless variable $y = p/\omega_0$. Finally, combining the contribution of the second discrete level and the continuous spectrum, we obtain

$$\Phi = \frac{3}{4} \times \frac{1}{9} = \frac{1}{12}, \tag{A.34}$$

and from Eqs. (A.18) and (A.23), the single-instanton contribution to the transition amplitude (A.16):

$$\begin{aligned} &\langle \pm q_0/2 |\, e^{-H_S \tau_0} \,| \mp q_0/2 \rangle_{\text{single}} \\ &= e^{-S_0^{(E)}} \sqrt{\frac{M\omega_0}{2\pi \sinh(\omega_0 \tau_0)}} \sqrt{\frac{S_0^{(E)}}{2\pi}} \omega_0 d\tau_c \left(\frac{1}{12}\right)^{-1/2} \\ &= \left(\sqrt{\frac{M\omega_0}{\pi}} e^{-\omega_0 \tau_0/2}\right) \left(\sqrt{\frac{6}{\pi}} \sqrt{S_0^{(E)}} e^{-S_0^{(E)}}\right) \omega_0 d\tau_c. \end{aligned} \tag{A.35}$$

Note that the factor in the first bracket corresponds to a simple harmonic operator, the exponential factor e^{-S_0} is classical contribution accounting for the action of the instanton, and the remaining represents for the fluctuation around the bouncing segments of the path. This result can be trusted as long as

$$\sqrt{S_0^{(E)}} e^{-S_0^{(E)}} \omega_0 \tau_0 \ll 1. \tag{A.36}$$

The energy of the lowest state is determined by the transition to the limit $\tau_0 \to \infty$. At large τ_0, paths constructed of many instantons and anti-instantons are important. Considering n instantons or anti-instantons with the arbitrary parameters $\tau_1, \tau_2, \ldots, \tau_n$ (see Fig. A.2). If the characteristic intervals satisfy $|\tau_i - \tau_j| \gg \omega_0^{-1}$, then individual instantons and anti-instantons do not interact each other. Therefore, the

transition amplitudes $\langle -q_0/2|\, e^{-H_S\tau_0}\, |+q_0/2\rangle$ is obtained by summation over n:

$$\begin{aligned}
&\langle -q_0/2|\, e^{-H_S\tau_0}\, |+q_0/2\rangle \\
&= \sum_{n\in\text{odd}} \left(\sqrt{\frac{M\omega_0}{\pi}} e^{-\omega_0\tau_0/2}\right) d^n \int_{-\tau_0/2}^{+\tau_0/2} \omega_0 d\tau_n \int_{-\tau_0/2}^{\tau_n} \omega_0 d\tau_{n-1} \cdots \int_{-\tau_0/2}^{\tau_2} \omega_0 d\tau_1 \\
&= \sum_{n\in\text{odd}} \left(\sqrt{\frac{M\omega_0}{\pi}} e^{-\omega_0\tau_0/2}\right) d^n \frac{(\omega_0\tau_0)^n}{n!} \\
&= \sqrt{\frac{M\omega_0}{\pi}} e^{-\omega_0\tau_0/2} \sinh\left(\omega_0\tau_0 d\right), \qquad \text{(A.37)}
\end{aligned}$$

where d is the instanton density

$$d = \sqrt{\frac{6}{\pi}} \sqrt{S_0^{(\mathrm{E})}} e^{-S_0^{(\mathrm{E})}}. \qquad \text{(A.38)}$$

Similarly, $\langle +q_0/2|\, e^{-H_S\tau_0}\, |+q_0/2\rangle$ is obtained as

$$\langle +q_0/2|\, e^{-H_S\tau_0}\, |+q_0/2\rangle = \sqrt{\frac{M\omega_0}{\pi}} e^{-\omega_0\tau_0/2} \cosh\left(\omega_0\tau_0 d\right). \qquad \text{(A.39)}$$

Finally, we consider how the transition amplitude (A.37), (A.39) can be understood in physical terms. Considering the two-state system (2.8), the transition amplitude can be expressed as

$$\begin{aligned}
&\langle \pm q_0/2|\, e^{-H_S\tau_0}\, |+q_0/2\rangle \\
&= \langle \pm q_0/2|\, e^{(\Delta_0/2)\sigma_x\tau_0}\, |+q_0/2\rangle \\
&= \langle \pm q_0/2|\, \left[|E_g\rangle\, e^{(\Delta_0/2)\tau_0}\, \langle E_g| + |E_e\rangle\, e^{-(\Delta_0/2)\tau_0}\, \langle E_e|\right] |+q_0/2\rangle. \qquad \text{(A.40)}
\end{aligned}$$

Using $\langle +q_0/2|E_g\rangle = \langle -q_0/2|E_g\rangle = \langle +q_0/2|E_e\rangle = -\langle -q_0/2|E_e\rangle$,

$$\begin{aligned}
\langle +q_0/2|\, e^{-H_S\tau_0}\, |+q_0/2\rangle &\propto \cosh(\Delta_0\tau_0/2), \qquad \text{(A.41)} \\
\langle -q_0/2|\, e^{-H_S\tau_0}\, |+q_0/2\rangle &\propto \sinh(\Delta_0\tau_0/2). \qquad \text{(A.42)}
\end{aligned}$$

Comparing this expression with Eq. (A.37), the tunneling amplitude Δ_0 is expressed as

$$\Delta_0 = 2\omega_0 d = 2\omega_0 \sqrt{\frac{6S_0^{(\mathrm{E})}}{\pi}} e^{-S_0^{(\mathrm{E})}}. \qquad \text{(A.43)}$$

Rewriting it in terms of the potential barrier height V_b, we obtain Eq. (2.7).

Appendix B

The Influence function of the Spin-boson Model

In this appendix, following Ref. [15], we derive the influence function of the spin-boson model (4.2). Let us start with the Caldeira-Leggett model (2.1). For simplicity, we consider the local system coupled with one reservoir. Using a standard imaginary-time path integral, the density matrix at $\beta = 1/k_{\rm B}T$ can be written as

$$W_\beta(q'', \boldsymbol{x}''; q', \boldsymbol{x}') = Z_t^{-1} \int_{q(0)=q'}^{q(\beta)=q''} \mathcal{D}q(\tau) \int_{\boldsymbol{x}(0)=\boldsymbol{x}'}^{\boldsymbol{x}(\beta)=\boldsymbol{x}''} \mathcal{D}\boldsymbol{x}(\tau)\, e^{-S^{(\rm E)}[q(\tau), \boldsymbol{x}(\tau)]}, \tag{B.1}$$

where Z_t is the partition function of the global system. As explicitly indicated, the functional integrations run over all the paths taken by the coordinates of the local system $q(\tau)$ and reservoir $\boldsymbol{x}(\tau)$ with endpoints $q(0) = q'$, $\boldsymbol{x}(0) = \boldsymbol{x}'$, $q(\beta) = q''$, and $\boldsymbol{x}(\beta) = \boldsymbol{x}''$. The Euclidean action $S^{(E)}$ is given by the sum of the contributions from the system, the reservoir, and the interaction as follows:

$$S^{(\rm E)} = S_{\rm S}^{(\rm E)} + S_{\rm B}^{(\rm E)} + S_{\rm I}^{(\rm E)} = \int_0^\beta d\tau \, \left[\mathcal{L}_{\rm S}^{(\rm E)}(\tau) + \mathcal{L}_{\rm B}^{(\rm E)}(\tau) + \mathcal{L}_{\rm I}^{(\rm E)}(\tau) \right], \tag{B.2}$$

where the Euclidean Lagrangians of the Caldeira-Leggett model (2.1) are given by

$$\mathcal{L}_{\rm S}^{(\rm E)}(\tau) = \frac{M}{2}\dot{q}(\tau)^2 + V[q(\tau)], \tag{B.3}$$

$$\mathcal{L}_{\rm B}^{(\rm E)}(\tau) = \sum_{\alpha=1}^{N} \frac{m_\alpha}{2} \left[\dot{x}_\alpha(\tau)^2 + \omega_\alpha^2 x_\alpha(\tau)^2 \right], \tag{B.4}$$

$$\mathcal{L}_{\rm I}^{(\rm E)}(\tau) = \sum_{\alpha=1}^{N} \left[-C_\alpha x_\alpha(\tau) q(\tau) + \frac{1}{2} \frac{C_\alpha^2 q(\tau)^2}{m_\alpha \omega_\alpha^2} \right]. \tag{B.5}$$

Now, we focus on a reduced description in which the reservoir coordinates, $\boldsymbol{x}(\tau)$, are eliminated. To this end, we introduce the reduced density matrix

$$\rho_\beta(q'', q') = {\rm Tr}_{\rm B} \left[W_\beta(q'', \boldsymbol{x}''; q', \boldsymbol{x}') \right] = \int_{-\infty}^{\infty} d\boldsymbol{x}' \, W_\beta(q'', \boldsymbol{x}'; q', \boldsymbol{x}'), \tag{B.6}$$

and the reduced partition function

$$Z(\beta) = \frac{Z_t(\beta)}{Z_{\rm B}(\beta)}, \tag{B.7}$$

where Z_B is the partition function of the isolated reservoir described by the collection of N harmonic oscillators

$$Z_B = \prod_{\alpha=1}^{N} Z_B^{(\alpha)} = \prod_{\alpha=1}^{N} \frac{1}{2\sinh(\beta\omega_\alpha/2)} \tag{B.8}$$

Thus, the reduced density matrix can be written in the form

$$\rho_\beta(q'', q') = Z^{-1} \int_{q(0)=q'}^{q(\beta)=q''} \mathcal{D}q(\tau)\, e^{-S_S^{(E)}[q(\tau)]} \mathcal{F}^{(E)}[q(\tau)], \tag{B.9}$$

where $\mathcal{F}^{(E)}$ is the influence functional

$$\begin{aligned} \mathcal{F}^{(E)}[q(\tau)] &\equiv e^{-S_{infl}^{(E)}[q(\tau)]} \\ &= \frac{1}{Z_B} \oint \mathcal{D}\boldsymbol{x}(\tau)\, e^{-S_B^{(E)}[q(\tau),\boldsymbol{x}(\tau)] - S_I^{(E)}[q(\tau),\boldsymbol{x}(\tau)]}. \end{aligned} \tag{B.10}$$

The integration $\oint \mathcal{D}\boldsymbol{x}(\tau)$ indicates the sum over all periodic paths with period β taken by the coordinates of the reservoir $\boldsymbol{x}$. In the following, we calculate the Euclidean influence action $S_{infl}^{(E)}[q(\tau)]$.

We choose periodic continuation of the paths $q(\tau)$ and $\boldsymbol{x}(\tau)$. Therefore, we can expand the coordinates as Fourier series

$$x_\alpha(\tau) = \frac{1}{\beta} \sum_{n=-\infty}^{\infty} e^{i\nu_n\tau} \tilde{x}_{\alpha,n}, \tag{B.11}$$

$$q(\tau) = \frac{1}{\beta} \sum_{n=-\infty}^{\infty} e^{i\nu_n\tau} \tilde{q}_n, \tag{B.12}$$

where $\tilde{x}_{\alpha,n} = \tilde{x}^*_{\alpha,-n}$, $\tilde{q}_n = \tilde{q}^*_{-n}$, and $\nu_n = 2\pi n/\beta$, $(n = 0, \pm1, \pm2, \dots)$ is a Matsubara frequency. Substituting the Fourier expansion (B.11) and (B.12) into Eq. (B.2), we obtain

$$\begin{aligned} S_{B,I}^{(E)}[q(\tau), \boldsymbol{x}(\tau)] &\equiv S_B^{(E)}[q(\tau), \boldsymbol{x}(\tau)] + S_I^{(E)}[q(\tau), \boldsymbol{x}(\tau)] \\ &= \sum_{\alpha=1}^{N} \frac{1}{\beta} \sum_{n=-\infty}^{\infty} \frac{m_\alpha}{2} \left(\nu_n^2 |\tilde{x}_{\alpha,n}|^2 + \omega_\alpha^2 \left| \tilde{x}_{\alpha,n} - \frac{C_\alpha \tilde{q}_n}{m_\alpha \omega_\alpha^2} \right|^2 \right). \end{aligned} \tag{B.13}$$

Next, we split $\tilde{x}_{\alpha,n}$ into the classical part $\bar{x}_{\alpha,n}$ and the quantum part $y_{\alpha,n}$ as

$$\tilde{x}_{\alpha,n} = \bar{x}_{\alpha,n} + y_{\alpha,n} = \frac{C_\alpha \tilde{q}_n}{m_\alpha(\nu_n^2 + \omega_\alpha^2)} + y_{\alpha,n}, \tag{B.14}$$

where $\bar{x}_{\alpha,n}$ is the stationary solution determined from the equation of motion

$$m_\alpha \frac{d^2 \bar{x}_\alpha(\tau)}{d\tau^2} - m_\alpha \omega_\alpha^2 \bar{x}_\alpha(\tau) + C_\alpha q(\tau) = 0. \tag{B.15}$$

Substituting Eq. (B.14) into (B.13), we obtain

$$S^{(\mathrm{E})}_{\mathrm{B,I}}[q(\tau),\boldsymbol{x}(\tau)] = S^{(\mathrm{E})}_{\mathrm{B}}[\boldsymbol{y}(\tau)] + S^{(\mathrm{E})}_{\mathrm{infl}}[q(\tau)] \tag{B.16}$$

$$\begin{aligned} S^{(\mathrm{E})}_{\mathrm{B}}[\boldsymbol{y}(\tau)] &= \sum_{\alpha=1}^{N} \frac{1}{\beta} \sum_{n=-\infty}^{\infty} \frac{m_\alpha}{2} \left(\nu_n^2 + \omega_\alpha^2\right) |y_{\alpha,n}|^2 \\ &= \sum_{\alpha=1}^{N} \int_0^\beta d\tau \, \frac{m_\alpha}{2} \left[\dot{y}_\alpha(\tau)^2 + \omega_\alpha^2 y_\alpha(\tau)^2\right] \end{aligned} \tag{B.17}$$

$$S^{(\mathrm{E})}_{\mathrm{infl}}[q(\tau)] = \sum_{\alpha=1}^{N} \frac{C_\alpha^2}{2m_\alpha} \frac{1}{\beta} \sum_{n=-\infty}^{\infty} \left(\frac{1}{\omega_\alpha^2} - \frac{1}{\nu_n^2 + \omega_\alpha^2}\right) |q_n|^2. \tag{B.18}$$

The path sum of all β-periodic quantum fluctuations $\boldsymbol{y}(\tau)$ directly yields the partition function of the reservoir,

$$Z_{\mathrm{B}} = \oint \mathcal{D}\boldsymbol{y}(\tau) \, e^{-S^{(\mathrm{E})}_{\mathrm{B}}[\boldsymbol{y}(\tau)]}. \tag{B.19}$$

Hence this term cancels the factor Z_{B}^{-1} in Eq. (B.10). The influence action (B.18) may be concisely written as

$$S^{(\mathrm{E})}_{\mathrm{infl}}[q(\tau)] = \frac{M}{2} \frac{1}{\beta} \sum_{n=\infty}^{\infty} \xi_n |q_n|^2, \tag{B.20}$$

$$\xi_n = \frac{1}{M} \sum_{\alpha=1}^{N} \frac{C_\alpha^2}{m_\alpha \omega_\alpha^2} \frac{\nu_n^2}{(\nu_n^2 + \omega_\alpha^2)} = \frac{2}{M q_0^2} \int_0^\infty d\omega \, \frac{I(\omega)}{\omega} \frac{\nu_n^2}{(\nu_n^2 + \omega^2)}, \tag{B.21}$$

where $I(\omega)$ is the spectral density defined in Eq. (2.17). Performing the inverse Fourier transformation, the influence action (B.20) becomes

$$S^{(\mathrm{E})}_{\mathrm{infl}}[q(\tau)] = \int_0^\beta d\tau \int_0^\tau d\tau' \, k(\tau - \tau') q(\tau) q(\tau'), \tag{B.22}$$

$$k(\tau) = \frac{M}{\beta} \sum_{n=-\infty}^{\infty} e^{i\nu_n \tau} \xi_n. \tag{B.23}$$

Note that the kernel $k(\tau)$ satisfies $k(\tau) = k(\beta - \tau) = k(\tau + \beta)$ and $\int_0^\beta d\tau \, k(\tau) = 0$. Using these properties, the influence function (B.22) is rewritten as

$$S^{(\mathrm{E})}_{\mathrm{infl}}[q(\tau)] = -\frac{1}{2} \int_0^\beta d\tau \int_0^\tau d\tau' \, k(\tau - \tau') \left[q(\tau) - q(\tau')\right]^2. \tag{B.24}$$

Evidently, the influence action $S^{(\mathrm{E})}_{\mathrm{infl}}[q(\tau)]$ is fully nonlocal. Alternatively, the influence action is expressed in terms of the kernel

$$\tilde{k}(\tau) = \mu : \delta(\tau) : -k(\tau), \tag{B.25}$$

where $: \delta(\tau) :$ is the periodically continued δ-function,

$$S^{(\mathrm{E})}_{\mathrm{infl}}[q(\tau)] = \frac{1}{2} \int_0^\beta d\tau \int_0^\tau d\tau' \, \tilde{k}(\tau - \tau') \left[q(\tau) - q(\tau')\right]^2. \tag{B.26}$$

With choice

$$\mu = \sum_{\alpha=1}^{N} \frac{C_\alpha \alpha^2}{m_\alpha \omega_\alpha^2} = \frac{2}{q_0^2} \int_0^\infty d\omega \, \frac{I(\omega)}{\omega}, \tag{B.27}$$

the kernel can be expressed as

$$\tilde{k}(\tau) = \frac{2}{q_0^2 \beta} \sum_{n=-\infty}^{\infty} \int_0^\infty d\omega \, I(\omega) \frac{\omega}{\nu_n^2 + \omega^2} e^{i\nu_n \tau} \tag{B.28}$$

$$= \frac{1}{q_0^2} \int_0^\infty d\omega \, I(\omega) \frac{\cosh[\omega(\beta/2 - \tau)]}{\sinh(\omega\beta/2)}. \tag{B.29}$$

Considering the spin-boson model, the path $q(\tau)$ is piecewise constant and it occasionally jumps between the positions $+q_0/2$ and $-q_0/2$, which are positions give minimal potential energy of the local system. It is convenient to put

$$q(\tau) = \frac{q_0}{2} \sigma_z(\tau), \tag{B.30}$$

where $\sigma_z(\tau)$ is a spin path. Thus, the spin path, $\sigma_z(\tau)$, jumps forth and back between the variables $+1$ and -1, and is expressed by

$$\sigma_z(\tau) = 1 + 2 \sum_{j=1}^{2m} (-1)^j \theta(\tau - s_j), \tag{B.31}$$

which implies a path of $2m$ alternating flips with centers $\{s_j\}$. Introducing the kernel $K(\tau) \equiv q_0^2 \tilde{k}(\tau)$, the influence function (B.10) takes form

$$\mathcal{F}^{(\mathrm{E})}[\sigma_z(\tau)] = \exp\left[-\frac{1}{8} \int_0^\beta d\tau \int_0^\tau d\tau' \, K(\tau - \tau') \left[\sigma_z(\tau) - \sigma_z(\tau') \right]^2 \right] \tag{B.32}$$

$$K(\tau) = \int_0^\infty d\omega \, I(\omega) \frac{\cosh[\omega(\beta/2 - \tau)]}{\sinh(\omega\beta/2)}. \tag{B.33}$$

From these results, it is straightforward to derive the partition function (4.1) with the kernel (4.3).

Appendix C

The Noninteracting-blip Approximation (NIBA)

In this appendix, based on Ref. [15], we derive the symmetrized correlation function (3.48) in the NIBA and discuss the conditions for the NIBA. The density matrix of the global system (2.8), $\hat{W}(t)$, is written in the real-time path integral form as

$$\begin{aligned}\langle q_f, \boldsymbol{x}_f|\, \hat{W}(t)\, |q_f', \boldsymbol{x}_f'\rangle &= \int dq_i dq_i' d\boldsymbol{x}_i d\boldsymbol{x}_i'\, K(q_f, \boldsymbol{x}_f, t; q_i, \boldsymbol{x}_i, 0)\, \langle q_f, \boldsymbol{x}_f|\, \hat{W}(0)\, |q_f', \boldsymbol{x}_f'\rangle \\ &\quad \times K^*(q_f', \boldsymbol{x}_f', t; q_i', \boldsymbol{x}_i', 0), \end{aligned} \tag{C.1}$$

where $q_{i/f}$ and $\boldsymbol{x}_{i/f}$ are the coordinates of the local system and reservoir, respectively, and K is the coordinate representation of the time evolution operator

$$K(q_f, \boldsymbol{x}_f, t; q_i, \boldsymbol{x}_i, 0) = \langle q_f, \boldsymbol{x}_f|\, e^{-iHt}\, |q_i, \boldsymbol{x}_i\rangle \tag{C.2}$$

$$= \int \mathcal{D}q(t)\mathcal{D}\boldsymbol{x}(t)\; e^{iS[q(t), \boldsymbol{x}(t)]}. \tag{C.3}$$

Here, the functional integration, $\int \mathcal{D}q(t)\mathcal{D}\boldsymbol{x}(t)$, extends over all paths with endpoints

$$q(0) = q_i, \quad q(t) = q_f, \quad \boldsymbol{x}(0) = \boldsymbol{x}_i, \quad \boldsymbol{x}(t) = \boldsymbol{x}_f, \tag{C.4}$$

and $S[q(t), \boldsymbol{x}(t)]$ is the action of the global system. The density matrix of the global system describes the dynamics of the system-plus-environment complex as a whole. However, in most cases of interest, the only information one wishes to have is the system's dynamics under the reservoir's influence. Then, the quantity one is really interested in is the reduced density matrix defined as

$$\rho(q_f, q_f'; t) = \int d\boldsymbol{x}_f\; \langle q_f, \boldsymbol{x}_f|\, \hat{W}(t)\, |q_f', \boldsymbol{x}_f\rangle\,. \tag{C.5}$$

Assuming that the density matrix of the global system at $t = 0$ is in a product initial state

$$\hat{W}(0) = \rho_{\rm S}(0) \otimes \frac{1}{Z_{\rm B}} e^{-\beta H_{\rm B}}, \tag{C.6}$$

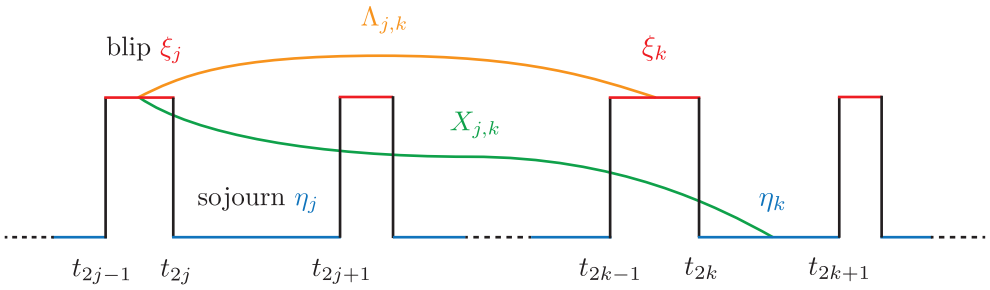

FIGURE C.1: Graphical representation of sojourns and blips. $\Lambda_{j,k}$ is the interaction between blip j and blip k, and $X_{j,k}$ is the interaction between blip j and sojourn k.

where ρ_S is the density matrix of the local system, e.g., $\rho_S(0) = |\uparrow\rangle\langle\uparrow|$, the reduced density matrix is expressed by

$$\rho(q_f, q_f'; t) = \int dq_i dq_i' \, J_{FV}(q_f, q_f', t : q_i, q_i', 0)\rho(q_i, q_i'; 0), \tag{C.7}$$

$$J_{FV}(q_f, q_f', t : q_i, q_i', 0) = \int \mathcal{D}q\mathcal{D}q' \, e^{i(S_S[q]-S_S[q'])}\mathcal{F}_{FV}[q, q'], \tag{C.8}$$

where $\mathcal{F}_{FV}[q, q']$ is the Feynman-Vernon influence functional. In the two-state system, it can be expressed in terms of the spin path [68]:

$$\begin{aligned}\mathcal{F}_{FV}[\sigma_z, \sigma_z'] = \exp\Bigg\{ &-\frac{1}{4}\int_0^t dt' \int_0^{t'} dt'' \, \left[\sigma_z(t') - \sigma_z'(t')\right] \\ &\times \left[\ddot{Q}(t'-t'')\sigma_z(t'') - \ddot{Q}^*(t'-t'')\sigma_z'(t'')\right]\Bigg\},\end{aligned} \tag{C.9}$$

where $\sigma_z(\tau) = q(\tau)/(q_0/2)$, $\sigma_z'(\tau) = q'(\tau)/(q_0/2)$, and $Q(t)$ is the kernel given as

$$Q(t) = \int_0^\infty d\omega \, \frac{I(\omega)}{\omega}\left\{\coth\left(\frac{\beta\omega}{2}\right)[1-\cos(\omega t)] + i\sin(\omega t)\right\}. \tag{C.10}$$

We note that $Q(t)$ is related with $W(\tau)$ in Eq. (4.6) via the analytical continuation as $Q(t) = W(\tau = it)$. Introducing antisymmetric and symmetric spin paths

$$\xi(t) = \frac{\sigma_z(t) - \sigma_z'(t)}{2}, \tag{C.11}$$

$$\eta(t) = \frac{\sigma_z(t) + \sigma_z'(t)}{2}, \tag{C.12}$$

respectively, the influence functional (C.9) is rewritten as

$$\mathcal{F}_{FV}[\sigma_z, \sigma_z'] = \exp\left\{\int_0^t dt' \, \dot{\xi}(t') \int_0^{t'} dt'' \, \left[Q'(t'-t'')\dot{\xi}(t'') + iQ''(t'-t'')\dot{\eta}(t'')\right]\right\}, \tag{C.13}$$

where $Q'(t) \equiv \mathrm{Re}[Q(t)]$ and $Q''(t) \equiv \mathrm{Im}[Q(t)]$.

In the two-state system, the reduced density matrix is 2×2 matrix. Intervals of the spin path dwelling in the diagonal and off-diagonal states have been termed 'sojourn' and 'blip', respectively [6]. During a sojourn, the function $\xi(t)$ is zero, whereas during a blip interval the function $\eta(t)$ is zero. There are two sojourn states

($\eta_i = \pm 1$) and two blip states ($\xi_i = \pm 1$). A general sojourn-to-sojourn path making $2n$ transitions at intermediate times t_j, $(j = 1, 2, \ldots, 2n)$ is parametrized by

$$\eta^{(n)}(t) = \sum_{j=0}^{n} \eta_j \left[\theta(t - t_{2j}) - \theta(t - t_{2j+1})\right], \tag{C.14}$$

$$\xi^{(n)}(t) = \sum_{j=0}^{n} \xi_j \left[\theta(t - t_{2j-1}) - \theta(t - t_{2j})\right]. \tag{C.15}$$

Denoting the intervals spent in blip and sojourn states by τ_j and s_j, respectively, we have (see Fig. C.1)

$$\tau_j = t_{2j} - t_{2j-1}, \quad s_j = t_{2j+1} - t_{2j}. \tag{C.16}$$

Thus, the influence functional (C.13) can be written as

$$\mathcal{F}^{(n)} = G_n H_n, \tag{C.17}$$

$$G_n = \exp\left[-\sum_{j=1}^{n} Q'_{2j,2j-1}\right] \exp\left[-\sum_{j=2}^{n}\sum_{k=1}^{j-1} \xi_j \xi_k \Lambda_{j,k}\right], \tag{C.18}$$

$$H_n = \exp\left[i \sum_{j=1}^{n}\sum_{k=0}^{j-1} \xi_j \eta_k X_{j,k}\right] = \exp\left[i \sum_{k=0}^{n-1}\sum_{j=k+1}^{n} \xi_j \eta_k X_{j,k}\right]. \tag{C.19}$$

Here, $\Lambda_{j,k}$ is an interaction between blip j and blip k, and $X_{j,k}$ is an interaction between blip j and sojourn k (see Fig. C.1):

$$\Lambda_{j,k} = Q'_{2j,2k-1} + Q'_{2j-1,2k} - Q'_{2j,2k} - Q'_{2j-1,2k-1}, \tag{C.20}$$

$$X_{j,k} = Q''_{2j,2k+1} + Q''_{2j-1,2k} - Q''_{2j,2k} - Q''_{2j-1,2k+1}, \tag{C.21}$$

where $Q_{j,k} = Q(t_j - t_k)$. The blip interactions are bundled up in the real-valued function G_n. The first exponential factor in Eq. (C.18) contains the intrablip interactions, and the second exponential factor represents the interblip correlations. The interactions between the sojourns and the blips are in the phase factor H_n. However, the sojourns do not interact with each other. The function G_n is a filtering function which suppresses long blips. Hence, it is favored that the system dwells in sojourn states. Physically, this is because continuous measurement of σ_z due to the environment suppresses quantum interference between the eigenstates of σ_z, and results in the decrease of occupation lengths of blip states.

Using the influence functional (C.17), we obtain the dynamics of the population $\langle \sigma_z \rangle_t$ as follows:

$$\langle \sigma_z \rangle_t = 1 + \sum_{m=1}^{\infty} (-1)^m \int_0^t \mathcal{D}_{2m,0}\{t_j\} \frac{1}{2^m} \sum_{\{\xi = \pm 1\}} F_m, \tag{C.22}$$

where

$$\int_0^t \mathcal{D}_{2m,0}\{t_j\} = \int_0^t dt_{2m} \cdots \int_0^{t_2} dt_1 \, \Delta^{2m}, \tag{C.23}$$

and the effect of the reservoir is included in the influence function

$$F_m = G_m \prod_{k=0}^{m-1} \cos\left(\sum_{j=k+1}^{m} \xi_j X_{j,k}\right). \tag{C.24}$$

In addition, one can derive the generalized master equation for the population:

$$\frac{d\langle\sigma_z\rangle_t}{dt} = -\int_0^t dt'\, K_z(t,t')\langle\sigma_z\rangle_t, \tag{C.25}$$

Compared Eq. (C.22) with (C.25), the kernel $K_z(t,t')$ is expressed as

$$K_z(t,t') = \Delta^2 F_1(t,t') + \sum_{n=2}^{\infty}(-1)^{n-1}\frac{\Delta^{2n}}{2^n}\int_{t'}^{t} dt_{2n-1}\cdots\int_{t'}^{t_3} dt_2 \sum_{\{\xi_j=\pm\}} \tilde{F}_n, \tag{C.26}$$

where $\tilde{F}_n$ is irreducible influence function defined by subtraction of the reducible parts in F_n. Here, 'irreducible' means that it cannot be separated into two or more uncorrelated parts at sojourns.

Now, we turn to the discussion of the dynamics within the noninteracting-blip approximation (NIBA). The simple assumption underlying the NIBA is that the average time $\langle s\rangle$ spent by the system in sojourn states is very large compared to the average time $\langle\tau\rangle$ spent in blip states. In detail, the NIBA assumption leads to two simple prescriptions regarding the sojourn-blip correlation $X_{j,k}$ and interblip interactions $\Lambda_{j,k}$.

1. Set the sojourn-blip correlation

$$X_{j,k} = \begin{cases} 0, & (j \neq k+1), \\ Q''(\tau_{k+1}), & (j = k+1). \end{cases} \tag{C.27}$$

2. Set all interblip interactions $\Lambda_{j,k}$ equal to zero.

With these specifications, the influence functional (C.17) reduces to a factorized form of intrablip correlations in which the sign of the individual blip phase depends on the label of respective preceding sojourn,

$$\mathcal{F}^{(n)}_{\mathrm{NIBA}} = \prod_{j=1}^{n} \exp\left[-Q'(\tau_j) + i\xi_j\eta_{j-1}Q''(\tau_j)\right]. \tag{C.28}$$

Generally, the NIBA can be justified in three cases discussed in Section 3.5 of the main text.

In the NIBA, since the irreducible influence functions $\tilde{F}_n$ become zero for $n > 1$, the kernel $K_z(t,t')$ is approximated as

$$K_{z,\mathrm{NIBA}}(t,t') = \Delta^2 F_1(t,t') = \Delta^2 e^{-Q'(t-t')}\cos\left[Q''(t-t')\right]. \tag{C.29}$$

Since this kernel depends only on the relative time $t-t'$, one can perform the Laplace transformation for it:

$$K_{z,\mathrm{NIBA}}(\lambda) = \Delta^2\int_0^\infty d\tau\, e^{-\lambda\tau}e^{-Q'(t-t')}\cos\left[Q''(t-t')\right]. \tag{C.30}$$

From Eq. (C.25), the Laplace transformation of the kernel is related to the population under the condition $\langle\sigma_z\rangle_{t=0} = +1$ as follows:

$$\langle\sigma_z(\lambda)\rangle = \frac{1}{\lambda + K_z(\lambda)}. \tag{C.31}$$

The symmetrized correlation function $S(t)$ defined in Eq. (2.44) is related to the population as follows [56]:

$$S(t) = \langle\sigma_z\rangle_{|t|}\,, \tag{C.32}$$

under the condition $\langle\sigma_z\rangle_{t=0} = +1$. Performing the Fourier transformation for Eq. (C.32) and using Laplace transformation of the population (C.31),

$$S(\omega) = 2\mathrm{Re}\int_0^\infty dt\, e^{i\omega t}\,\langle\sigma_z\rangle_t \tag{C.33}$$

$$= 2\mathrm{Re}\left[\langle\sigma_z(-i\omega)\rangle\right] = 2\mathrm{Re}\left[\frac{1}{-i\omega + K_z(-i\omega)}\right]. \tag{C.34}$$

Rewriting the kernel $K_z(\lambda)$ with the self-energy $\Sigma(\lambda)$ (3.49), we finally derive Eq. (3.48).

Appendix D

Impedances of the Transmission Line

We analyze the frequency dependence of the spectral density for the circuit model discussed in Chapter 6. Assuming $|\omega C_j Z_{j+1}(\omega)| \ll 1$, the recurrence relation (6.40) is given approximately:

$$Z_j(\omega) \simeq R_j + i\omega L_j + Z_{j+1}(\omega) - i\omega C_j Z_{j+1}(\omega)^2. \tag{D.1}$$

In the continuous limit $N \to \infty$, where N is the number of islands in the transmission line, this recurrence relation reduces to the differential equation:

$$\frac{\partial Z(\omega, x)}{\partial x} \simeq -r(x) - i\omega l(x) + i\omega c(x) Z(\omega, x)^2, \tag{D.2}$$

where $r(x)$, $l(x)$, and $c(x)$ ($0 \leq x = j/N \leq 1$) are the resistance, inductance, and capacitance per unit length, respectively. From Eq. (6.41), they are given as

$$r(x) = r_0 x^n, \tag{D.3}$$
$$l(x) = l_0 x^p, \tag{D.4}$$
$$c(x) = c_0 x^m, \tag{D.5}$$

where $r_0 = R_0 N$, $l_0 = L_0 N$, and $c_0 = C_0 N$. We note that $Z(\omega) = Z(\omega, x \to 0)/2$.

D.1 The flux qubit

For the choice of the parameters given in Eq. (6.42), the differential equation for the impedance is written as

$$\frac{\partial Z(\omega, x)}{\partial x} \simeq -r_0 x^n - i\omega l_0 + i\omega c_0 x^m Z(\omega, x)^2. \tag{D.6}$$

Under the condition

$$x^* \equiv \left(\frac{n}{2\omega\sqrt{l_0 c_0}}\right)^{2/(m+2)} \ll x \ll \left(\frac{\omega l_0}{r_0}\right)^{1/n}, \tag{D.7}$$

$\dot{Z}(\omega, x) = \partial Z(\omega, x)/\partial x$ and $r_0 x^n$ are sufficiently small compared with other terms in the right-hand side of Eq. (D.6). Then, we obtain

$$Z_A(\omega, x) = \sqrt{\frac{l_0}{c_0}} x^{-m/2}, \tag{D.8}$$

In contrast, for $x \simeq 0$, we can neglect $r(x)$ and $c(x)$, and obtain the following:

$$Z_B(\omega, x) = -i\omega l_0 x + A(\omega). \tag{D.9}$$

The constant of integration, $A(\omega)$, can be determined by the equation $Z_A(\omega, x^*) = Z_B(\omega, x^*)$. Thus, we arrive at the approximate expression of $Z(\omega)$ as follows:

$$\begin{aligned} Z(\omega) &\sim \frac{Z_B(\omega, x \to 0)}{2} \\ &= \frac{1}{2}\left(i\omega l_0 x^* + \sqrt{\frac{l_0}{c_0}} (x^*)^{-m/2} \right). \end{aligned} \tag{D.10}$$

From Eq. (6.27), we obtain the following the spectral density:

$$I(\omega) \propto I_0(\omega) = \omega \mathrm{Re}\left[Z(\omega)^{-1} \right] \propto \omega^{2/(m+2)} \tag{D.11}$$

Note that since m is a non-negative real number, this circuit realizes sub-Ohmic reservoirs with arbitrary sub-Ohmic exponent s ($s < 1$). This frequency dependence appears for $\omega^* \ll \omega \ll \omega_c$, where the lower bound, ω^*, is obtained by considering the condition (D.7):

$$\omega^* = \left[\left(\frac{m}{2}\right)^{2n} \frac{r_0^{m+2}}{c_0^n l_0^{m+n+2}} \right]^{1/(m+2n+2)}. \tag{D.12}$$

D.2 The charge qubit

For the choice of the parameters given in Eq. (6.45), the differential equation for the impedance is written as

$$\dot{Z}(\omega, x) \simeq -r_0 x^n - i\omega l_0 x^p + i\omega c_0 Z(\omega, x)^2. \tag{D.13}$$

The spatial dependence of the elements is different from the case of the flux qubit. However, we can analyze the behavior of the impedance in the same way. In this case, neglecting $\dot{Z}(\omega, x)$ and $r_0 x^n$ give the impedance as

$$Z_A(\omega, x) = \sqrt{\frac{l_0}{c_0}} x^{p/2}, \tag{D.14}$$

for

$$x^* \equiv \left(\frac{p}{2\omega\sqrt{l_0 c_0}} \right)^{2/(p+2)} \ll x \ll \left(\frac{\omega l_0}{r_0} \right)^{1/(n-p)}. \tag{D.15}$$

In contrast, for $x \simeq 0$, we can neglect terms that elements have the spatial dependence and obtain

$$Z_B(\omega, x) = -\frac{1}{i\omega c_0 x + A(\omega)}. \tag{D.16}$$

From the condition $Z_A(\omega, x^*) = Z_B(\omega, x^*)$ and Eq. (6.39), the frequency dependence of the spectral density is obtained as

$$I(\omega) \propto I_0(\omega) = \omega \mathrm{Re}[Z(\omega)] \propto \omega^{2/(p+2)}. \tag{D.17}$$

Note that since p is a non-negative real number, this circuit realizes sub-Ohmic reservoirs with arbitrary sub-Ohmic exponent s ($s < 1$). This frequency dependence for $I(\omega)$ appears for $\omega^* \ll \omega \ll \omega_c$. The lower bound, ω^*, is obtained from the condition (D.15):

$$\omega^* = \left[\left(\frac{p}{2}\right)^{2(n-p)} \frac{r_0^{p+2}}{c_0^{n-p} l_0^{n+2}} \right]^{1/(2n-p+2)}. \tag{D.18}$$

D.3 The charge qubit $(0 < s \leq 0.5)$

We can analytically investigate the power of the impedance in the same way as the above two cases. For the choice of the parameters given in Eq. (6.48), the differential equation for the impedance is written as

$$\dot{Z}(\omega, x) \simeq -r_0 x^n + i\omega c_0 Z(\omega, x)^2. \tag{D.19}$$

For

$$x^* \equiv \left(\frac{n^2}{4\omega r_0 c_0}\right)^{1/(n+2)} \ll x, \tag{D.20}$$

we can neglect $\dot{Z}(\omega, x)$ and obtain:

$$Z_A(\omega, x) = e^{-i\pi/4} \sqrt{\frac{r_0}{\omega c_0}} x^{n/2}. \tag{D.21}$$

On the other hand, for $x \simeq 0$, we can neglect the first terms of the right hand side in Eq. (D.19). It gives the impedance for $x \simeq 0$ as

$$Z_B(\omega, x) = -\frac{1}{i\omega c_0 x + A(\omega)}, \tag{D.22}$$

where $A(\omega)$ is the constant of integration and determined by the equation $Z_A(\omega, x^*) = Z_B(\omega, x^*)$. Therefore, from Eq. (6.39), we obtain the spectral density as follows

$$I(\omega) \propto I_0(\omega) = \omega \mathrm{Re}\left[Z(\omega)\right] \propto \omega^{1/(n+2)}. \tag{D.23}$$

Note that since n is a non-negative real number, this circuit realizes sub-Ohmic reservoirs with $0 < s \leq 0.5$. This frequency dependence appears for $\omega^* \ll \omega \ll \omega_c$, where the lower bound, ω^*, and cutoff frequency, ω_c, are given as

$$\omega^* = \frac{1}{r_0 c_0} \left(\frac{n}{2}\right)^2 \left(1 + \frac{2\sqrt{2}}{n}\right)^{n+2}, \tag{D.24}$$

$$\omega_c = \frac{N^2}{r_0 c_0} \left(\frac{2N}{n}\right)^n, \tag{D.25}$$

respectively.

Bibliography

[1] R. Landauer, IBM J. Res. Dev. **1**, 223 (1957).

[2] S. Datta, *Electronic Transport in Mesoscopic Systems* (Cambridge University Press, Cambridge, 1995).

[3] K. Saito, Europhys. Lett. **83**, 50006 (2008).

[4] K. Schwab, E. A. Henriksen, J. M. Worlock, and M. L. Roukes, Nature **404**, 974 (2000).

[5] A. C. Hewson, *The Kondo Problem to Heavy Fermions* (Cambridge University Press, Cambridge, 1997).

[6] A. J. Leggett *et al.*, Rev. Mod. Phys. **59**, 1 (1987).

[7] D. Segal and A. Nitzan, Phys. Rev. Lett. **94**, 034301 (2005).

[8] T. Ojanen and A. P. Jauho, Phys. Rev. Lett. **100**, 155902 (2008).

[9] R. M. Potok, I. G. Rau, H. Shtrikman, Y. Oreg, and D. Goldhaber-Gordon, Nature **446**, 167 (2007).

[10] Z. Iftikhar *et al.*, Nature **526**, 233 (2015).

[11] Z. Iftikhar *et al.*, Science **360**, 1315 (2018).

[12] D. L. Cox and A. Zawadowski, Adv. Phys. **47**, 599 (1998).

[13] R. Bulla, T. A. Costi, and T. Pruschke, Rev. Mod. Phys. **80**, 395 (2008).

[14] A. Ronzani *et al.*, Nat. Phys. **14**, 991 (2018).

[15] U. Weiss, *Quantum Dissipative Systems*, 4th ed. (World Scientific, Singapore, 1999).

[16] Y. Makhlin, G. Schön, and A. Shnirman, Rev. Mod. Phys. **73**, 357 (2001).

[17] B. Peropadre, D. Zueco, D. Porras, and J. J. García-Ripoll, Phys. Rev. Lett. **111**, 243602 (2013).

[18] J. Leppäkangas *et al.*, Phys. Rev. A **97**, 052321 (2018).

[19] J. Bourassa *et al.*, Phys. Rev. A **80**, 032109 (2009).

[20] A. Nitzan, *Chemical Dynamics in Condensed Phases: Relaxation, Transfer, and Reactions in Condensed Molecular Systems* (Oxford University Press, Oxford, 2006).

[21] J. Ren, P. Hanggi, and B. Li, Phys. Rev. Lett. **104**, 170601 (2010).

[22] D. Segal, A. J. Millis, and D. R. Reichman, Phys. Rev. B **82**, 205323 (2010).

[23] T. Ruokola and T. Ojanen, Phys. Rev. B **83**, 045417 (2011).

[24] T. Chen, X. B. Wang, and J. Ren, Phys. Rev. B **87**, 144303 (2013).

[25] Y. Yang and C. Q. Wu, Europhys. Lett. **107**, 30003 (2014).

[26] C. Wang, J. Ren, and J. Cao, Sci. Rep. **5**, 11787 (2015).

[27] J. Liu, H. Xu, B. Li, and C. Wu, Phys. Rev. E **96**, 012135 (2017).

[28] F. Guinea, V. Hakim, and A. Muramatsu, Phys. Rev. B **32**, 4410 (1985).

[29] K. Saito and T. Kato, Phys. Rev. Lett. **111**, 214301 (2013).

[30] L. Magazzù *et al.*, Nat. Commun. **9**, 1403 (2018).

[31] P. Forn-Díaz *et al.*, Nat. Phys. **13**, 39 (2017).

[32] J. E. Mooij *et al.*, Science **285**, 1036 (1999).

[33] P. W. Anderson and G. Yuval, J. Phys. C: Solid State Phys. **4**, 607 (1971).

[34] J. M. Kosterlitz, Phys. Rev. Lett. **37**, 1577 (1976).

[35] R. Bulla, N. H. Tong, and M. Vojta, Phys. Rev. Lett. **91**, 170601 (2003).

[36] M. Vojta, N. H. Tong, and R. Bulla, Phys. Rev. Lett. **94**, 070604 (2005).

[37] A. Winter, H. Rieger, M. Vojta, and R. Bulla, Phys. Rev. Lett. **102**, 030601 (2009).

[38] M. Vojta, N.-H. Tong, and R. Bulla, Phys. Rev. Lett. **102**, 249904 (2009).

[39] A. W. Chin, J. Prior, S. F. Huelga, and M. B. Plenio, Phys. Rev. Lett. **107**, 160601 (2011).

[40] M. Vojta, Phys. Rev. B **85**, 115113 (2012).

[41] E. Luijten, *Interaction range, universality and the upper critical dimension*, PhD thesis, Delft University of Technology, 1997.

[42] E. Luijten and H. W. Blöte, Phys. Rev. B **56**, 8945 (1997).

[43] N. H. Tong and M. Vojta, Phys. Rev. Lett. **97**, 016802 (2006).

[44] L. B. Yu, N. H. Tong, Z. Y. Xue, Z. D. Wang, and S. L. Zhu, Sci. China Phys. **55**, 1557 (2012).

[45] M. Kato, Master Thesis (Graduate School of Science, The Universe of Tokyo, 2017).

[46] A. O. Caldeira and A. J. Leggett, Physica A **121**, 587 (1983).

[47] A. I. Vaĭnshteĭn, V. I. Zakharov, V. A. Novikov, and M. A. Shifman, Sov. Phys. Usp. **25**, 195 (1982).

[48] J. Maciejko, *An Introduction to Nonequilibrium Many-Body Theory* .

[49] A. J. Bray and M. A. Moore, Phys. Rev. Lett. **49**, 1545 (1982).

[50] S. Chakravarty, Phys. Rev. Lett. **49**, 681 (1982).

[51] S. K. Kehrein, A. Mielke, and P. Neu, Z. Phys. B **99**, 269 (1996).

[52] S. K. Kehrein and A. Mielke, Phys. Lett. A **219**, 313 (1996).

[53] H.-P. Breuer and F. Petruccione, *The Theory of Open Quantum Systems* (Oxford University Press, Oxford, 2002).

[54] M. Kato, Theory of heat transport via a local two-state system, Master's thesis, The University of Tokyo, 2016.

[55] H. Shiba, Prog. Theor. Phys. **54**, 967 (1975).

[56] M. Sassetti and U. Weiss, Phys. Rev. Lett. **65**, 2262 (1990).

[57] B. K. Agarwalla and D. Segal, New J. Phys. **19**, 043030 (2017).

[58] U. Weiss and H. Grabert, Phys. Lett. A **108**, 63 (1985).

[59] H. Rieger and N. Kawashima, Eur. Phys. J. B **9**, 233 (1999).

[60] H. Spohn and R. Dümcke, J. Stat. Phys. **41**, 389 (1985).

[61] R. H. Swendsen and J.-S. Wang, Phys. Rev. Lett. **58**, 86 (1987).

[62] G. A. Baker Jr., *Essentials of Padé Approximants* (Academic Press, New York, 1975).

[63] K. Völker, Phys. Rev. B **58**, 1862 (1998).

[64] H. Bruus and K. Flensberg, *Many-Body Quantum Theory in Condensed Matter Physics* (Oxford University Press, Oxford, 2004).

[65] H. Miyazaki, Y. Takahide, A. Kanda, and Y. Ootuka, Phys. Rev. Lett. **89**, 197001 (2002).

[66] A. Altland and B. Simons, *Condensed Matter Field Theory*, 2nd ed. (Cambridge University Press, Cambridge, 2010).

[67] L. D. Landau and E. M. Lifshitz, *Quantum Mechanics: Non-Relativistic Theory*, 3rd ed. (Butterworth-Heinemann, Oxford, 1981).

[68] R. P. Feynman and F. L. Vernon, Ann. Phys. (N. Y). **24**, 118 (1963).